VERIFICATION OF HANDHELD ULTRASONIC TOMOGRAPHY FOR INTEGRATION INTO A BRIDGE MAINTENANCE DEVICE

A Thesis

by

JACQUELINE BYNDAS

Submitted to the Office of Graduate and Professional Studies of
Texas A&M University
in partial fulfillment of the requirements for the degree of

MASTER OF SCIENCE

Chair of Committee, Stefan Hurlebaus
Committee Members, Robert Lytton
Alex (Gwo-Ping) Fang
Head of Department, Robin Autenrieth

December 2016

Major Subject: Civil Engineering

ABSTRACT

This thesis investigates the competences, limitations, and modifications of a handheld ultrasonic tomography device for integration into a zero-intrusive automatic bridge maintenance device. The handheld device relies on low-frequency pulse-echo methodology to identify and localize a variety of defects as well as determine specimen thickness. Current available non-destructive equipment is not suitable for the evaluation of in-service concrete structures since it is time consuming and expensive. Therefore, there is a need to develop a high speed non-destructive testing device in order to evaluate current structures for retrofitting or new construction. This thesis validates this handheld device for integration, discusses preliminary design options, and identifies key features necessary for high speed application.

Eleven preconstructed concrete slab specimens, containing a variety of artificial defects including delaminations, air-voids and water-voids, were tested using the handheld system. This research concludes that the system effectively determines the initial depth of the defects and rebar within 10 percent of the actual location, with the exception of one artificial delamination located an inch from the surface. This is the shallowest defect and indicates that there may be near-sighted issues. This device determined the thickness to be within 2.6 percent of the actual thickness for all specimens, ranging from 305 mm (12.0 in.) to 610 mm (24.0 in.) deep. It was also determined that transducer orientation plays a significant role in characterizing flaws; the vertical orientation is able to identify horizontal defects more clearly, while the horizontal orientation detects vertical defects more effectively. All flaws identified within the specimens are parallel to the surface, and cracks located at the surface or propagating vertically were not recognized by the system. It was also found that overlapping measurements

significantly improve image clarity, but scans without overlapping measurements are still able to successfully characterize and localize an artificial defect as well as two layers of rebar. Slabs containing simulated delaminations demonstrate a shadowing effect, where whole or partial reflections of the plastic can be seen throughout the slab since the ultrasonic waves are unable to penetrate through the defect.

The most functional design consists of a cylinder of transducers equally spaced along the outer surface area to eliminate signal timing issues and reduce damage from impact forces. The final product will be larger and able to operate at a variety of speeds since the signal will be generated automatically as the transducers come into contact with the specimen surface. Digital mapping is key for database application and should be integrated into the device to generate a visual map database of defects beneath the surface of concrete structures.

DEDICATION

To my Lily, who has shown me pure and unconditional love

ACKNOWLEDGMENTS

I would like to express my gratitude to my committee chair, Dr. Stefan Hurlebaus, for his support, guidance, and knowledge throughout the pursuit of my graduate studies. I would also like thank my committee members, Dr. Robert Lytton and Dr. Alex (Gwo-Ping) Fang for sharing your passions, providing your continuous support and insightful comments during this process.

I thank my project partner, Justin Buskmiller, for all his contributions, hard work, countless meetings, and support throughout this research. My sincerest thanks to TxDOT for providing funding to make this research possible.

A special thank you to my friends, especially Jessica Phillips and Freddy Allen, for becoming my family in Texas. To my boyfriend, Vyacheslav Prakhov, thank you for the continuous support and encouragement throughout this adventure. Last, but certainly not least, thank you to my family, especially my parents and siblings, John, Helga, Katy, and Jake for always believing in me.

TABLE OF CONTENTS

Page

LIST OF FIGURES

Page

LIST OF TABLES

Page

1. INTRODUCTION

1.1 Problem Statement

Millions of vehicles travel across roadways and bridges each day, making them critical to modern society. In the United States, the average age of existing functional bridges is around 42 years. The state of Texas has the highest number of bridges at about 53,000, followed by Ohio which has a total of approximately 28,000 bridges. In Texas, 14% of bridges are considered to be functionally obsolete and 2% are structurally deficient (Texas Department of Transportation, 2014). Although efforts are being made to improve the bridge infrastructure, it is difficult to assess bridges in high-traffic urban areas since closure for inspection and repair could have negative repercussions (ASCE, 2013). Chase and Laman (2000) note that the major problem with the National Highway System (NHS) bridges are the bridge decks, which are either in poor condition, or are too narrow for present day traffic demands. Over 88% (2.8 billion ft^2) of all the bridge deck area in the United States is concrete, and about half it has a wearing surface. It is estimated that only $12.6 billion is spent on bridges annually, while $20.5 billion is needed to bring the nation's bridges up to par by 2028 (ASCE, 2013). Owing to the current state of bridge infrastructure, there is a need to develop network-level bridge deck evaluation methods that can repeatedly provide an accurate assessment of the bridge deck's condition. There is also a need for project-level deck evaluation to avoid cost overruns in deck replacement projects.

To combat deteriorating bridge decks and bring them up to satisfactory conditions, it would require various state Departments of Transportation (DOT) to invest large sums of

money and resources. Even after the restoration of bridges, it requires lifelong maintenance and observation to ensure the safety of millions of people.

Due to the importance of safe and reliable infrastructure, there is a need for rapid non-destructive testing (NDT) technologies that can identify and characterize concrete deterioration in bridge decks. Current NDT technology is not practical for preventative measures, and therefore it is usually not used until defects are visible, meaning the structure has already sustained substantial damage. The investigation of these defects are then carried out at a slow rate, which can take hours for a small section or days for an entire bridge deck. Rapid collection will allow engineers to provide quality control during construction and assess structure conditions before extensive damage is visible. For these reasons, it is essential that the technology be fast, accurate, and easy to use. This research aims to determine if ultrasonic tomography can be integrated into a zero-intrusive bridge maintenance device, which would increase safety standards and minimize maintenance costs.

1.2 Research Objectives

The first objective is to perform a literature review to understand the concrete degradation process, investigate possible non-destructive testing techniques, and evaluate current bridge deck inspection devices. This will provide a solid foundation for this research.

The second objective is to validate the use of a specific handheld ultrasonic tomography device as a capable non-destructive testing instrument. It is critical to determine the current capabilities and limitations of the handheld device before possible integration into an automated system. These capabilities are determined by testing the handheld device on eleven preconstructed concrete slabs, representative of a concrete bridge deck, with known locations of rebar and artificial defects. The slabs will be tested without knowledge regarding defect

locations and the results will be compared to a previously generated defect key by Wimsatt et al. (2008). In addition, this objective will determine the influence of transducer orientation and step size on the device's ability to determine depth, detect rebar, and identify defects. These tasks are critical to determine if ultrasonic tomography is a viable solution for fast-paced scanning of concrete bridge decks.

The third objective of this research is to configure several possible preliminary designs. A prototype design is critical for development of a successful innovative device. This thesis will discuss five potential designs, the brainstorming process for each, as well as the strengths and weaknesses of each design. These preliminary designs focus on the exterior of the prototype, primarily the transducer placement. The first design option will be a stepping device, where two separate transducer arrays are used to compile ultrasonic scans. The first transducer array takes a measurement, which is followed by the second array being placed directly next to the first array to take the second measurement and so forth until the entire desired area is scanned. The second option consists of a continuous track of transducers, similar to a tank, which seamlessly moves across the desired surface. The third option encompasses commercially available transducer arrays that are mounted along a wheel, with the transducers facing outwards for continuous measurements. The fourth design option is similar to the third, but adds additional transducers in between the existing rectangular arrays. The fifth option contains equally spaced transducers to reduce damage while improving reliability. Ultimately, one configuration will be determined to be the most suitable for a prototype design and eventually full size application.

The fourth objective is to determine features necessary for an ultrasonic tomography device to operate at high speeds. This will address physical features necessary for the final

design as well as potential logistics issues. High resolution, real-time images are critical for the final design, but this requires efficient transmission of data from the moving device to a stationary laptop for processing. This objective will review data acquisition and processing needs for the final design as well as the integration of digital mapping. The device's ability to operate at various speeds will be addressed in addition to the most critical forces on the device. This identifies aspects for improvement prior to device creation.

1.3 Thesis Organization

This thesis follows the objectives stated in the research proposal and previous section. Upon completion of the introductory chapter, the second chapter discusses processes that contribute to the degradation of reinforced concrete structures, existing non-destructive technology, and currently available non-destructive devices for the detection of defects below the surface.

Chapter 3 discusses the process for testing the eleven concrete specimens. A few of the concrete slabs are control specimens whereas others contain stimulated air- and water- filled voids, delaminations, natural cracks, and varying surface textures. It is critical that the handheld ultrasonic tomography device be validated prior to integration into a high speed piece of equipment. Validation serves several purposes; it develops proper collection techniques, familiarizes the researcher with settings for successful measurements, allows for the development of interpretive skills when analyzing results, and determines the reliability, capabilities, and potential issues for the compact handheld ultrasonic tomography system.

Chapter 4 identifies five different preliminary design options. The design options will be discussed in detail and will be evaluated for functionality. Each design has its strengths and weaknesses while capitalizing on different aspects of efficiency and design strategy.

Chapter 5 depicts necessary design considerations for integration into a high speed ultrasonic tomography device. This chapter outlines potential complications of the design and provides potential solutions for several challenges featuring the mechanical and electrical systems. Investigation prior to the creation of the final prototype design allows for easier integration and fewer obstacles later in the development process.

The final chapter discusses the overall findings of the research, which includes determining the overall competence of the handheld ultrasonic tomography device. This section readdresses potential issues of the ultrasonic tomography system prior to high speed integration. Mechanical design challenges for the final product are also be discussed with viable solutions. Ultimately, this research provides the foundation for development of a final design and physical prototype.

1.4 Summary of Findings

The compact handheld ultrasonic tomography system successfully identified the simulated air- and water-voids in addition to artificial delaminations created by thin pieces of plastic. All layers of rebar were successfully discovered and the device was able to determine the overall thickness of each specimen successfully, with a maximum error of 2.3 percent. Manufacturers stated the device can measure thicknesses up to 600 mm (23.6 in.), but it effectively determined thicknesses up to 610 mm (24.0 in.).

The device depicted the initial depth of the simulated defects, with the accuracy over depth being within 2.4 percent in all but one instance. One plastic defect was not identified, which indicates that there may be near-sighted issues with the system since other plastic defects were observed at deeper depths in other slabs. The evaluated location compared to the actual

location of the first layer of rebar was within 0.66 to 2.3 percent of the total depth of the slab. Though the second layer of rebar was identified, the accuracy diminished.

Transducer orientation influences whether vertical or horizontal rebar is more detectable. In all specimens, when the transducer array was in the vertical orientation, the horizontal rebar was seen more clearly, whereas when the transducer array was in the horizontal orientation, the vertical rebar was more evident. It was clear that overlap affected the clarity of the images. The scans without overlapping measurements still identified defects and two layers of reinforcing steel, but without the clarity of the images provided by overlapping measurements. This indicates that a trained individual should review scans without overlap to minimize inaccurate interpretations. Overall, the system was successful at identifying a variety of defects, at various depths, with and without overlapping measurements.

Of the preliminary designs, option five is optimal since it can easily be attached to a utility truck, consists of verified transducer arrays, and is capable of operating at a variety of speeds without affecting the signal capabilities. This design also minimizes stresses on the transducers during data collection while maintaining consistent contact with the ground at all times during transmission. An important feature of the final design will feature the transducers automatically emitting signals when the rows come into contact with the ground under self-weight. Signal processing will need to be expedited in order to produce real-time images for immediate inspections. Finally, a lightweight, maneuverable, bolted design is ideal to allow for ease of use and adjustments throughout the design process.

2. LITERATURE REVIEW

2.1 Bridge Deterioration Background

Concrete bridge decks can deteriorate at an alarming rate from consistent use, which in turn could contribute to a catastrophic failure and result in injury or cost human lives. Heavy traffic, constant cyclic loading, poor quality of construction, overloading, freeze-thaw cycles, and deicing salts may lead to rebar corrosion, delamination, cracking, and concrete degradation. In concrete, multiple deterioration mechanisms may integrate, making the deterioration process of concrete structures complex. It is well known that concrete is weak in tension. To improve the performance of concrete structures under tension, reinforcing steel bars are typically embedded in concrete. ACI 318 (2014) specifies minimum concrete cover thickness for various reinforced concrete structures to ensure that the reinforcing steel is protected from the elements. The use of deicing salts, which contain chloride, can corrode the reinforcing steel, which ultimately affects the bridge deck capacity. Gucunski (2013) notes that the two most common corrosion processes are chlorine-induced pitting and carbonation. The two types of corrosion can usually be visually determined. Chlorine-pitted corrosion leaves black marks along the steel, whereas carbonation will leave a gold-brown or red colored rust. Corrosion is a time dependent deterioration mechanism which usually depends on the type of steel used, temperature, moisture content, and exposure levels. Freeze-thaw cycles also greatly contribute to the process of rebar corrosion. Reinforcement corrosion may lead to delamination in the concrete deck. When reinforcing steel corrodes, it expands, which induces stresses on the concrete surrounding the bar. The concrete eventually cracks and propagates, leading to the deterioration of the structure. In addition to stresses caused by the corrosion of steel, other

factors may accelerate concrete cracking, including the curing process of concrete, air temperature, traffic loads, and the geometry of the bridge. Deterioration of concrete can lead to a reduction in the load carrying capacity of the structure, which is a major cause for concern.

Other situations that may cause concrete deterioration include; micro-cracking, Alkali-Silica Reaction (ASR), Delayed Ettringite Formation (DEF), and plastic shrinkage. ASR is fueled by the reactive silica in aggregates and the alkalis in cement, which in turn produces a gel that increases in volume in the presence of water. Similar to delamination, this volume increase causes stress, which produces internal cracking at the surface of the structure (Farny and Kerkhoff, 2007). Unlike corrosion, which happens at the rebar location, ASR can cause cracking anywhere in concrete. Quillin (2001) explains DEF as the formation of ettringite and associated expansion when concrete is subjected to high temperatures during its curing period. At elevated curing temperatures (>70°C) the formation of calcium silicate hydrate (C-S-H) gel is accelerated. The accelerated formation rate of C-S-H gel physically traps some of the sulphates and aluminates in its layered structure before they can react to form ettringite. At high curing temperatures, the trapping continues until the C-S-H gel becomes fully saturated with sulphates. After the concrete has gone through the entire heat curing cycle, and when stored in a moist environment at ambient temperatures, the sulphates diffuse out of the C-S-H gel into the pore solution. This provides an internal source of sulphates and triggers the reformation of ettringite in hardened concrete. The reformation of ettringite causes expansion and eventually cracking of concrete, which is widely known as DEF. However, the DEF mechanism can be prevented by limiting the curing temperature of concrete to below 70°C. It has also been established that Type III cement is more likely to contribute to this phenomena. A possible defect mechanism, especially in aged concrete bridges, is the de-bonding of asphalt

concrete from the underlying Portland cement concrete (Farny and Kerkhoff, 2007). This exposes the Portland cement concrete deck to a variety of foreign materials, such as water and chlorides, which contribute to the defects discussed previously.

It is critical to detect various defects caused by concrete deterioration mechanisms. Proper and timely identification of defects can help various transportation agencies take corrective actions to prevent failure of transportation systems and structures. By doing this, they also avoid expensive repairs and replacements. Various non-destructive testing (NDT) techniques may be used for detecting defects in concrete structures without compromising the integrity of the structure. The following section briefly discusses the various NDT techniques that have been used in the past for the evaluation of bridge decks.

2.2 Non-destructive Testing Methods

2.2.1 Brief History of Non-destructive Testing

While visual inspection can be considered as one of the earliest evaluation techniques, this technique is only useful when concrete cracks are visible on the surface. It does not give any indication of the interior condition of the concrete. In past years, several non-destructive techniques have been used in the transportation industry for the evaluation of concrete bridge decks. All non-destructive testing techniques involve a sent signal (wave) and a received response. One early non-destructive testing technique included researchers exciting a specimen with sound, like dropping a coin or tapping an object, and listening for the reflected sound waves to detect abnormalities (White, 2012). In 1895, Wilhelm Conrad Rontgen, conducted an experiment where he produced an electromagnetic wave that would leave a fluorescent trace on paper coated with barium platinocyanide. These fluorescent images, which could vary

depending on obstructing objects, are commonly known as X-rays (Nitske, W. R., 1971). His discovery and proceeding research initiated the field of radiology. A few decades later, Sergei Sokolov, who is known as the father of ultrasonic testing, indicated in the 1920s that he could detect flaws in metal through a transmission technique. He proposed the idea of the first ultrasonic camera, which used sound waves operating at a frequency of 3000 MHz and received the reflected waves with a large piezoelectric transducer. After the signal was received, the face of the transducer was scanned with a metal contact beam to produce an "image". Even though this technology was advanced for the time period, it did not produce an image of enough quality and therefore, it could not practically be used (Johnson, 2013). During the same time period, extensive research on flaw detection in metals was taking place in Germany.

In 1933, Muhlhauser received a patent for a system that transmitted ultrasonic energy and detected the response with secondary transducers. A few years later, in 1936, Pohlman developed the "Pohlamn Cell", which was an image converting device. By 1942, Sproule essentially used echo-sounding techniques to detect various defects in steel. Nondestructive testing procedure development progressed over the next few decades, with various researchers from around the world taking multiple approaches to refine non-destructive testing (Woo, 2015). From these origins, modern non-destructive testing techniques include, but are not limited to, impact-echo, chain dragging and hammer sounding, impulse response, electrical resistivity, ground penetrating radar, infrared thermography, and ultrasonic pulse echo. Each one of these methods is briefly discussed in the following sections.

2.2.2 Impact-Echo

Impact-echo is useful for detecting delamination in concrete. With this technique stress waves are generated by striking the bridge deck surface. The response waves are recorded with contact or air-coupled sensors near the site of impact. From this test, the frequency and the depth of reflection can be determined. This depth could be the possible location of a change in material, which can be the source of delamination in a bridge deck. Delamination causes the steel and concrete to separate, causing air-voids. Once the location of the delamination is determined, there are various ways to determine the severity of the delamination and how it will affect the overall health of the structure. One way to analyze the condition of the delamination is by observing the frequency pattern. A delaminated point will shift the frequency to higher amplitudes because the reflections occur at more shallow depths (Cheng and Sansalone, 1995). Figure 2.1 shows a simple schematic of the impact-echo procedure.

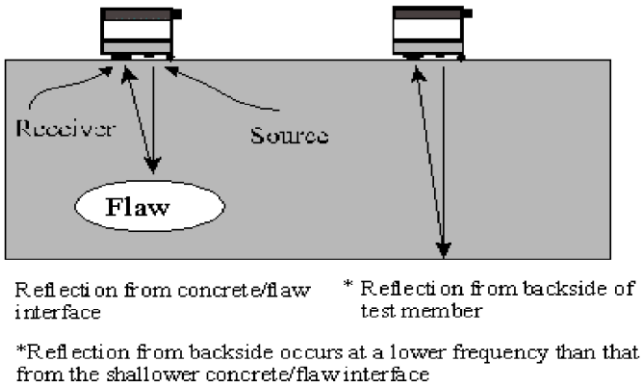

Figure 2.1: Schematic of Impact-Echo Method (Tinkey et al., 2003)

Gucunski et al. (2013) explains that the initial delamination between the layers of concrete and steel can be detected by relating the reflected waves and frequencies from the delamination site and the bottom of the bridge deck. Initial delamination is the most difficult to detect in comparison to progressed delamination, which can be clearly seen with a single

peak frequency, corresponding directly to the depth of the delamination. For shallow delamination, low frequency waves are reflected due to flexural-mode oscillations from the top portion of delamination.

Impact-echo is useful because it only requires one side access to a structure, and can detect the defects at various depths. Although it fits basic criteria for testing, an experienced operator is needed, because the same specimen can give varied results depending on the engineer. Additionally, impact-echo is only applicable to specimens with certain depths. Furthermore, the measurements have to be performed in a dense test grid, which makes impact-echo a slow process.

2.2.3 Chain Dragging and Hammer Sounding

This is a common inspection method that is utilized to inspect concrete bridge decks. This technique relies on changes in sound between quality concrete and concrete with voids when chains are dragged across the bridge deck, or when the deck is lightly tapped using a hammer. Chain dragging is limited to horizontal surfaces, but the hammer sounding technique can be used for a wide range of structures (Wimsatt et al., 2008).

This method can detect late stage delamination. However, the detection in sound differences is subjective and therefore can be misleading. This technique is also ineffective on bridge decks with overlay due to the influence of material changes.

2.2.4 Impulse Response

In the impulse response technique, stress waves are generated using a hammer and the dynamic response is measured using a geophone or an accelerometer (Wimsatt et al., 2008). This method detects honeycombing, voids under joints, and delaminations. It is also effective

at detecting cracks in concrete elements and the debonding of asphalt and concrete overlays on concrete decks. However, smaller defects may go undetected and the interpretation is dependent on the selection of the test points.

2.2.5 Electrical Resistivity

Electrical resistivity is a commonly used technique to detect anomalies in concrete, since it easily detects moisture, which can be directly related to the presence of defects. The presence of water insinuates the presence of chlorides, which can be linked directly to corrosion and delamination of steel from concrete. The damages and cracked areas of concrete are the paths of least resistance, the preferred path of electric current. The most common set up of electrical resistivity is the Wenner set-up (Gowers and Millard, 1999). It calculates resistivity due to the difference in potential between electrodes. It is highly valuable in detecting potentially corrosive areas that could in the long term affect bridge health.

Although the data collection is simple, interpretation can be difficult since the resistance can depend on moisture and salt content, and therefore poor evaluation can lead to false conclusions. In addition, the device needs the surface to be wetted prior to gathering data which makes the collection process time consuming and more difficult. Resistivity measurements can also be used to determine permeability, but in general they need to be coupled with other NDT test methods in order to verify results. Carbonation may also seriously impacts resistance, so it is generally recommended to avoid using the electrical resistivity method for defect detection in concrete (Wimsatt et al., 2008).

2.2.6 Air-Coupled Ground Penetrating Radar

Ground penetrating radar (GPR) has already been used on roadways at speeds up to 70 miles per hour for pavement profiling, object detection, and construction quality. For the evaluation of bridge decks, GPR is commonly used to determine the thickness of concrete layers, reinforcement configuration, location of air-voids, and estimate concrete electrical properties.

Figure 2.2 shows a picture of an air-coupled GPR system. The setup consists of a radar antenna attached with a fiberglass arm to the front of a moving vehicle. The antenna, which is directed to the ground, emits a high frequency electromagnetic wave and then captures the reflection in real-time. It is critical that the antenna be composed of fiberglass so it does not interfere with the emitted signal.

Figure 2.2: Air-Coupled GPR System (Wimsatt et al., 2008)

The variation in electrical properties of the constituent materials results in a change in response of the reflected energy. Using the relation of dielectric permittivity values, engineers

can determine a change in material since a portion of the wave will be reflected back to the antenna. In relation to the condition of a bridge deck, an engineer will evaluate the attenuation of the reflected waves at the top of the steel reinforcement. Advantages of the GPR system include the fast-paced nature, the use of electromagnetic waves that can penetrate concrete and other non-ferrous materials, ability to detect embedded materials, and 10% accuracy for location and depth of reinforcement when compared to true location (Wimsatt et al., 2008).

However, there are certain limitations for air-coupled GPR. For instance, if the concrete contains excessive amounts of water and/or many free chloride ions from deicing chemicals, the signal and recorded attenuation can be greatly affected. This results in inaccuracy, making it difficult for engineers to draw any conclusions. Temperature can also cause skewed results. In addition, it is not possible to directly image the delamination in the bridge deck, determine the mechanical properties of concrete, or conclusively detect corrosion. An additional obstacle for the implementation of GPR is that the Federal Communications Commission regulates transmitting power output and pulse rates, which makes it difficult to design and build new and improved systems (Barnes and Trottier, 2000). Moreover, the test equipment, if available, is expensive and an engineer needs extensive training to accurately interpret results (Wimsatt et al., 2008).

2.2.7 Infrared Thermography

Infrared thermography has been used for a few decades to detect flaws in bridge structures. This technology looks at electromagnetic radiation in relation to temperature and infrared wavelength to determine the location of cracks and delamination. The infrared camera looks at the rates of heating and cooling, comparing their infrared radiation. This energy is converted to an electrical signal and processed to create a temperature map for the user to see,

making misinterpretation minimal. The infrared camera functions on the principal that different materials emit different amounts of thermal radiation: the infrared camera detects differences in material, allowing the user to identify air-voids that result from cracking and delamination (Wimsatt et al., 2008).

For infrared thermography (IR) to work, the structure must be heated either by solar radiation or a heater. The infrared camera then displays how the structure emits heat since heat flows from a hot region to a cold region. Cracks or delaminated areas are usually filled with air or water, and these areas usually change temperature faster than surrounding materials.

Though the infrared camera can detect where a delamination or void is present in reference to the surface, it cannot detect the depth location of the flaw (Gucunski et al., 2013). This technique is also affected by surface anomalies and boundary conditions. Figure 2.3 shows a typical mobile infrared thermography setup as well as a thermal map.

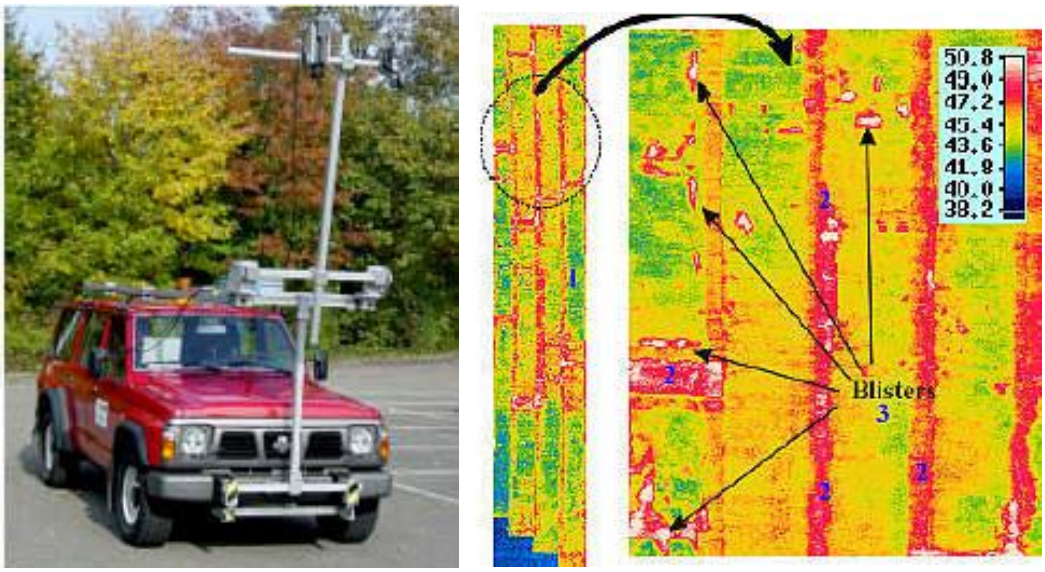

Figure 2.3: Mobile IR Measuring Equipment (Left) and Typical Thermal Map (Right) (Stimolo, 2003)

2.2.8 Ultrasonic Pulse Echo

Ultrasonic pulse echo is similar to impact-echo, but uses an acoustic stress instead of producing stresses by impact. These acoustic waves are produced by exciting a piezoelectric material (Wimsatt et al., 2008).

Ultrasonic testing was not used regularly in analyzing reinforced concrete structures until recently due to high scatter and attenuation, both of which made it difficult to determine any defects. In addition, probes had to be coupled to the ground with grease or wax, making the process slow and messy (Wimsatt et al., 2008). Low-frequency, dry coupled tip transducers have been developed to combat these issues in analysis of reinforced concrete.

2.2.9 Ultrasonic Tomography

Ultrasonic tomography is an extension of the ultrasonic pulse echo method, in which the transducers are usually set up in arrays. Some transducers fire the ultrasonic signal while the others act as receivers of the reflected signal. The basic principal behind ultrasonic non-destructive testing is that the waves travel through the medium and when they interface with an anomaly, a portion of the wave energy is reflected and captured by the receiving transducers. The velocity of the reflected wave helps identify acoustical impedance, which is then analyzed to determine defects. A clear decrease in velocity of the reflected waves is usually indicative of substantial deterioration (Wimsatt et al., 2008).

After the reflected waves are received, a Synthetic Aperture Focusing Technique (SAFT) algorithm is used to construct an almost real time image to identify cracking, debonding, delamination, or other defects. This method is extremely useful for structures that only have one-sided access, such as reinforced concrete bridge decks. In order for the device

to accurately reflect the condition of the structure, a closely spaced test grid is essential. It also takes time for the SAFT algorithm to create the display of the concrete. In addition, the resolution of the scan depends on how well the transducers are in contact with the structure, meaning that rough surfaces may impact the ability to accurately detect flaws (Bishko et al., 2008).

In concrete, ultrasonic tomography it can be difficult to detect voids within 0.5 in. and delamination within 0.75 in of the transducer array. Since there are a few drawbacks, the nature of ultrasonic testing makes it a prime candidate for the evaluation of concrete bridge decks. The most recognizable and popular device utilizing this technology is the 1040A MIRA device.

Previous work has been conducted by using the ultrasonic tomography system, shown in Figure 2.4(b), to verify the technique's ability to detect a wide variety of common defects at critical locations in structures. Ultrasonic tomography is a relatively new technology in the field of non-destructive testing and incorporates advanced pulse-echo ultrasonics with tomographic representation of a test field.

Typical systems employ an array of low-frequency shear wave transducers with a center frequency of 50 kHz. The A1040 MIRA ultrasonic tomography system incorporates a 4 by 12 grid of mechanically isolated and dampened dry-point-contact (DPC) transducers that do not require the use of a coupling agent. The device can fit the profile of a rough concrete testing surface with a variance of up to 0.4 inches due to the spring loaded technology (Acoustic Control Systems, 2015). The system is then manually applied at every desired testing point for data collection process, shown in Figure 2.4(a).

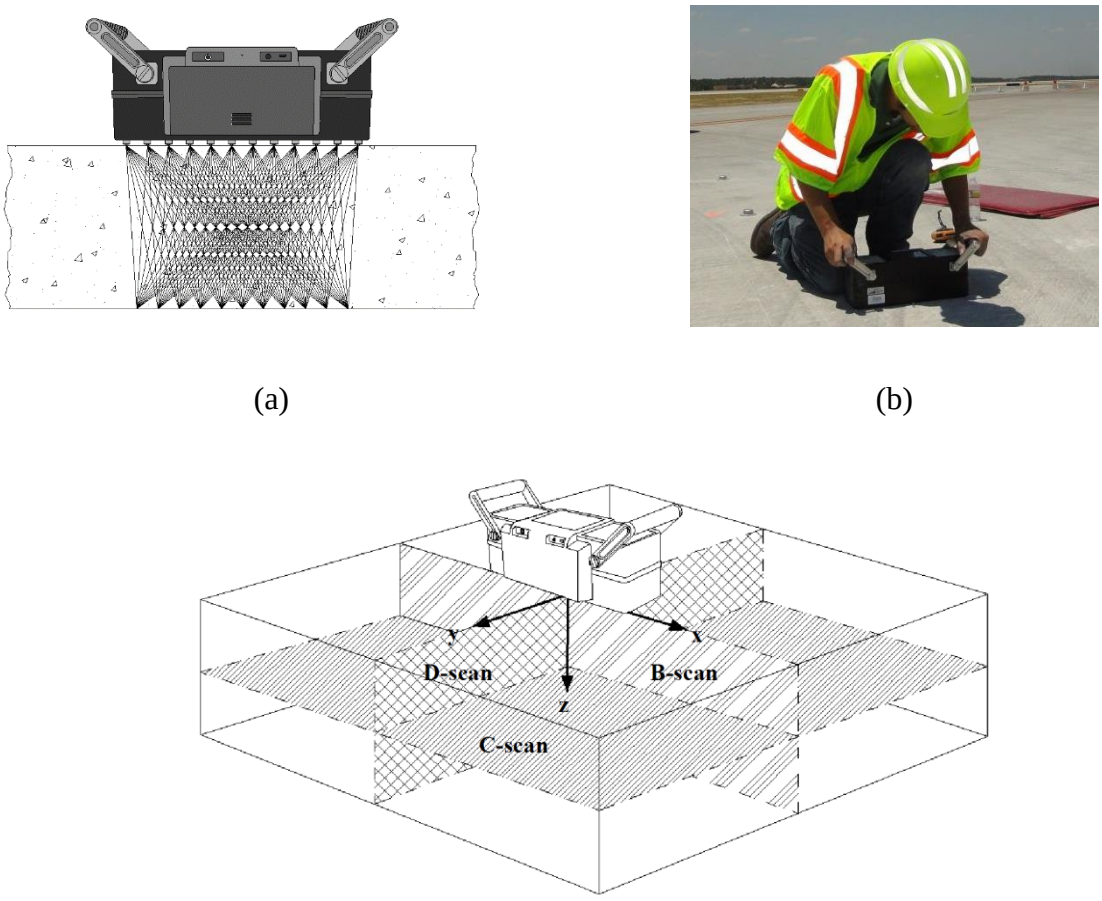

Figure 2.4: (a) Operational Sketch, (b) Physical Data Collection, (c) B-, C-, and D-Scans Relative to Tomograph

Using this linear array of elements, there is a wide coverage of shear wave pulses that reflect at internal interfaces where the material impedance changes. With the help of a digitally focused algorithm, an alteration of the SAFT algorithm, a 3-D volume is presented. This 3-D image can be dissected into each of the three planes, shown in Figure 2.4(c) representing its volume; the B-scan, C-scan, and D-scan.

For each scan, the various intensities reported by the returned waves are color coded from dark blue to deep red, representing low reflectivity, which is indicative of typically sound

concrete, and high reflectivity, which implies a defect of some sort, respectively. With this intensity scaling, it is easy to see any discontinuities with different wave speeds, such as voids, delaminations, cracks, and other abnormalities.

Various engineers have used the ultrasonic tomography technique extensively for applications ranging from bridge decks, highway pavements, airport runways, and tunnel linings. It has been successful at accurately and precisely locating delaminations, air- and water-filled voids, slab thickness, reinforcement mesh layout and depth, and various materials such as clay lumps (Im et al., 2010; Shokouhi et al., 2011; White et al., 2014; Wimsatt et al., 2013). The ultrasonic tomography testing method, by itself, is classified as a very low-speed non-destructive evaluation system that can collect data at approximately 1-2.5 min/ft^2 (Wimsatt et al., 2013).

2.2.10 NDT Summary

Previous research shows that various NDT techniques can be used for the detection of flaws in reinforced concrete decks. This is essential for the maintenance and repair of current transportation infrastructure. Specifically, technology is needed to characterize bridge deck deterioration in real time in order to determine early concrete deterioration which can potentially cause a catastrophic event. Fast, easy, and accurate detection would increase employee safety, save money and time while quickly identifying bridge deck damage for repair.

From the review of various NDT techniques above, the ultrasonic tomography technique shows the most promise in detecting anomalies in concrete. However, its sluggish pace majorly hinders widespread application with concrete bridge decks. For developing a

zero-intrusive, high-speed, and high resolution system, a rolling dry coupled spring loaded ultrasonic transducer system may be the most viable solution, and needs a detailed investigation.

2.3 SAFT Algorithm

2.3.1 Ultrasonic Tomography: History and Basics

The Synthetic Aperture Focusing Technique (SAFT) algorithm is a post processing algorithm that converts reflected ultrasonic data into a high resolution image. The first one-dimensional implementation of the SAFT algorithm was in the late 1970s, following the wide use of radar technology. When paralleled with other imaging techniques, the SAFT algorithm performs more accurately with smaller transducers at lower frequencies (Dengzhi, 2014). In 1982, Pacific Northwest Laboratory conducted studies to incorporate the SAFT algorithm in usable field equipment, following extensive development research conducted by Hall et al. (1986). It is important to note that the basic theory for the SAFT algorithm is only applicable to homogeneous materials, but it can be modified in order to accurately work for non-homogenous materials, like reinforced concrete.

The SAFT algorithm creates high-resolution images by superimposing several pulse echo signals that have been measured at various positions (Kotoky and Shekhar, 2013). The linear SAFT algorithm aides in the clarity of the images by numerically superimposing the data transmitted and received by the array of dry contact transducers. SAFT creates images based on results from either B- or C-scans while filtering out scattering. This leads to a clearer and more precise image that can accurately depict the defects below the surface (Burr at el., 1998).

To minimize scattering, transducers with low frequencies between 20 and 100 kHz are used (Kotoky and Shekhar, 2013). Minimizing the structural noise is critical because it can disguise some defects and inaccurately display others.

2.3.2 Geometry of the SAFT Algorithm

Due to the need for measurements at various positions, it is necessary to have the device send pulse-echoes in an array. From this post processing algorithm, engineers can translate ultrasonic data into images that can accurately identify the vast majority of defects.

It is critical that the path travelled from the emitting transducer to the defect and back to the receiving transducer be known for SAFT to work correctly, so an A-scan is necessary to provide geometrical guidance and restore the image. Once the transducers have received all emitted signals, the algorithm superimposes this computed data, which results in a high resolution image. A time-frequency template of the signals is used over a Fourier transform in order to preserve the time information of the signal. The time frequency analysis is then based on Wigner-Ville distribution.

Kotoky and Shekhar (2013) explain that the basics of the SAFT algorithm rely on geometry. For this, the focus of the ultrasonic transducers is assumed to be in constant phase, meaning the amplitude is consistent, before diverging at various angles in a cone shape. The angle of deflection is determined by transducer properties, primarily focal length and diameter. Due to this, it is necessary for the system to use a single type of transducer, because waves propagating at various angles would make the algorithm extremely difficult, if not impossible. These properties of the transducer are simply calculated by knowing the path length and travel time for a signal moving along that path. The aperture of the transducer is critical because it

assists in the layering of the A and B scan. The aperture width of the transducer corresponds to the width of the cone and at what range it can be applied. The path length that the signal must travel corresponds to the phase shift seen in the signal. From these geometric properties, an engineer can construct images that simplify the detection of defects below the concrete surface (Kotoky and Shekar, 2013). This geometric interpretation can be seen in Figure 2.5.

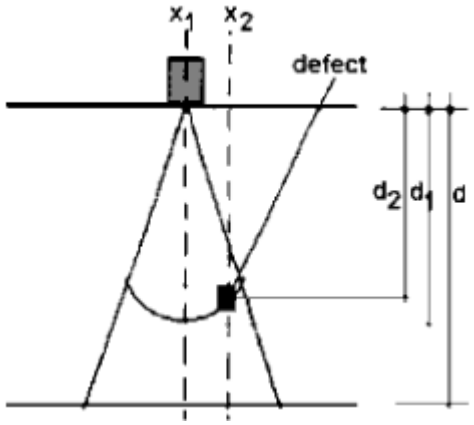

(a) Display of the waves passing through the Defect Zone

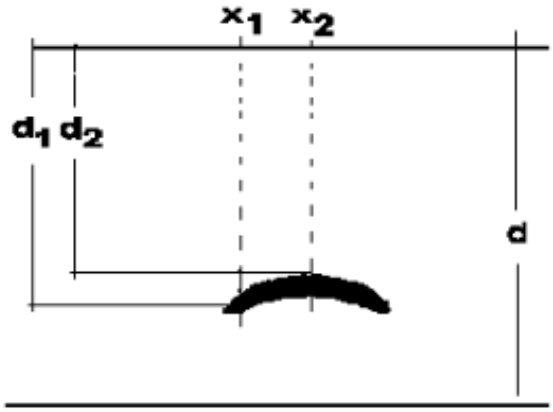

(b) B- Scan of the Iron Defect

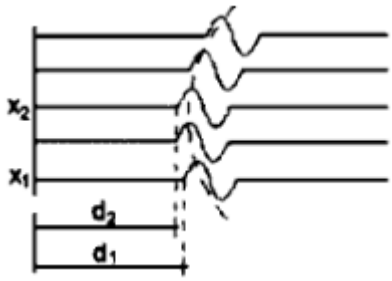

(c) Resulting Image Produced from the Waves Passing Through the Defect in 2.5(a).

Figure 2.5: Geometry Process for the SAFT Algorithm (Kotoky and Shekar, 2013)

As Kotoky and Shekhar explain in Figure 2.5(a), the wave is sent from the transducer at a distance x_1 in a conical shape, interacting with the defects at x_2. When the wave interacts with the defect, it is at a depth, d_2, while the same waves are at a depth, d_1 from the surface directly below the transducer. From this, Figure 2.5(b) is produced, showing the shape of the waves and the various distances. In this image, it shows the detection of a single round hole in an iron block. The final broad image is then produced using the transducer aperture width. With this technique, the A-scan is focused below the transducer as shown in Figure 2.5(a), which corresponds to the B-scan in Figure 2.5(b). These images are ultimately used to produce the final image in Figure 2.5(c).

With SAFT, the intention is to determine a parabola at each data point where a significant amount of energy is dispersed. If the summation of energy values over this parabola at a point is high, it is marked as a scattering point. For the scattering of a signal in non-homogeneous materials, it is important to know properties of this parabola, or conical shape, to reduce noise. In order to successfully reduce scattering, the parabola must be short in comparison with the whole array of transducers because of the larger size. In addition, by producing a smaller parabola, the algorithm is more efficient. In addition to relative shortness, it is important that the parabola be thick in order to average out noise due to small changes in the material. By using a thicker line, the amplitude indicating flaws is not as large, and it evens out noise for the non-homogeneous material. Only a flaw with the same length or larger than the parabola thickness can be detected, removing all the noise present in a non-homogeneous material (Burr et al., 1998).

2.3.3 Nonlinear SAFT

In the mid-1990s, using the original SAFT algorithm, it was difficult to interpret the results and usually required an engineer that was trained in special techniques to decipher recorded data (Burr et al., 1998). To improve this feature, the algorithm can be modified. This modification of the SAFT algorithm, usually discussed as a non-linear SAFT algorithm, is necessary for concrete structures, which are non-homogeneous. Nonlinear modification requires that the A-or B-scan of the surface be known from the linear system.

2.3.4 Noise Reduction

The spectrum of displacement can be calculated from the spectrum of the signal, at a specific location and frequency, multiplied by the signal's impulse response from passage through the structure. From deconvolution, the incident wave scattering is easy to deal with in a homogeneous material, but not with a non-homogeneous material like reinforced concrete. With these, the process fails; the calculated scatter does not match the actual scattering of the signal. The SAFT algorithm can be further modified to take into account that the length of the flaw is much larger than the length of the non-homogeneous particles. The correlation between two reflected signals at two different points in the transducer array may be used to differentiate which signals are from defects and which are related to structural noise (Burr et al., 1998).

2.3.5 Basic Mathematics of the SAFT Algorithm

With the SAFT algorithm, each transducer is treated as a point source for the waves, and the area of interest is the area below the point source, which is essentially a series of targets. According to Bamler (1992), Stepinski (2007), and Hoegh (2013), the basic synthetic aperture equation for continuous time and space is given by,

$$s(x_e, x_r, t) = \int_x^{\cdot} \int_z^{\cdot} f(x,z)\delta\big(t'(t, x_e, x_r, x, z)\big)\mathrm{d}z\mathrm{d}x \tag{2.1}$$

where $s(x_e, x_r, t)$ is the received A-scan, *f (x,z)* is the reflectivity function, $\delta\big(t'(t, x_e, x_r, x, z)\big)$ is the emitted pulse from the transducers, *t* is time, *z* is the vertical position of the defect, *x* is the horizontal position of the defect , x_e and x_k are the horizontal position of the emitting and receiving transducers, respectively. In basic mathematic equation, t' is defined as,

$$t' = t - \frac{1}{c}(\sqrt{z^2 + (x - x_e)^2} + \sqrt{z^2 + (x - x_r)^2}) \tag{2.2}$$

where *c* is the velocity of sound, which is constant, and *t* is the real time.

These equations were derived and explained by Bamler (1992), Stepinski (2007), and Hoegh (2013) for the SAFT algorithm in the time domain. Two assumptions when deriving these equations are: the material is isotropic, meaning uniformity in wave propagation throughout the material and the material is homogeneous. Due to the material reflectivity and the received signal, the SAFT algorithm can reconstruct a B-Scan using the inverse of relative reflectivity in the area of interest (Hoegh 2013).

2.3.6 Time vs Frequency Domain

Two applicable domains exist for the SAFT algorithm, time and frequency. The two domains have different capabilities. The time domain is easy to associate with a physical understanding and has a fairly simple algorithm, as denoted in the previous section. Conversely, the SAFT algorithm in the frequency domain is complicated and hard to relate to the physical world. Though the frequency domain algorithm is more difficult to develop, it can process data significantly faster while using much less computational memory. It is also important to note that the frequency domain can interpret the signal of various wave velocities,

whereas the time domain is very limited in this area (Hoegh 2013). The capabilities and limitations of each SAFT domain are summarized in Table 2.1.

Table 2.1. Comparison of SAFT Algorithm Domains

	Time Domain	Frequency Domain
Coding the Algorithm	Easier	Difficult
Ease of Relating to Physical Concepts	Simple	Complex
Memory Space Needed For Data and Computations	Immense	Minimal
Computation Speed	Slow	Fast
Capabilities with Different Wave Velocities	Limited	Larger Range

2.4 Current Concrete Bridge Deck Evaluation Technology

2.4.1 A1040 MIRA

A1040 MIRA (MIRA) is an ultrasonic tomographic device developed by Acoustic Control Systems used to image the internal configuration of a concrete structure with access to only one side. This device can detect defects such as honeycombing, cracks, holes, and delamination. This is possible because MIRA produces high quality, informative images for engineers to assess quality of construction and detect critical flaws in structures. It uses dry contact, 50 kHz transducers, which eliminate the need for contact gels to maintain a clean surface. MIRA consists of a linear array of 48 transducers in a configuration of 4 by 12. MIRA emits shear waves and receives the reflected signal by various transducer pairs which allows for various incident angles. These varying incident angles are critical to analysis of non-homogeneous materials (Hoegh 2013). The transducers are equipped with wear resistant tips that minimize damage and allow MIRA to be used on rough surfaces (Acoustic Control Systems, 2015). MIRA can be seen in Figure 2.6.

Figure 2.6: A1040 MIRA Ultrasonic Tomographic Device (Acoustic Control Systems, 2015)

2.4.1.1 Monostatic vs Bi-static Transducers

A monostatic transducer both emits and receives signals while in a bi-static system a transducers used for only one purpose, either emitting or receiving. In a bi-static system, a single or number of other transducers are near the one emitting the signal to receive the signal. MIRA A1040 is a bi-static system since the signal is received at a different location than it is emitted. The transducer can emit and receive a signal, but not simultaneously. Each row of transducers in the matrix will send a signal while the others receive the reflected waves, meaning MIRA emits 48 signals simultaneously at its rate of 50 kHz. Each image is processed and layered to produce the final image, which displays the defects within the concrete. The emitting process is shown in Figure 2.7.

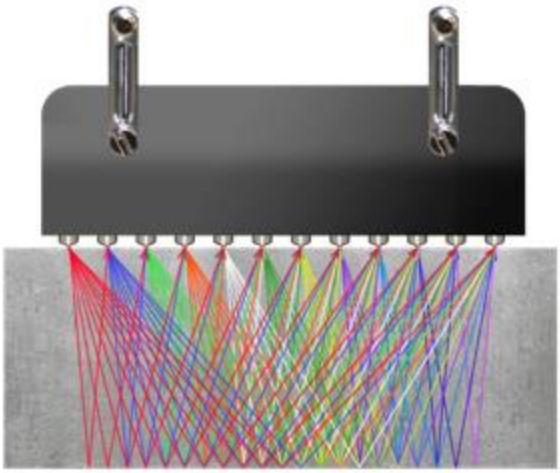

Figure 2.7: MIRA Emitting and Receiving Signals for One Scan (Acoustic Control Systems, 2015)

2.4.1.2 Data Files from MIRA

When extracting the data from MIRA, the user will observe that there are four different files for each scan. There will be an image file, which contain the final post processed images of the concrete. Also present is a .bin file that contains the saved tomogram, which is all the data associated with the image file. The size of the .bin files is related directly to the number of pixels. The .lvb file contains the raw data received by the transducers prior to any post processing. The last file is a .cfg file which encompasses a description of the configuration of the saved post-processed image. IdealViewer is the available commercial product to transform raw data files to a three dimensional model of the area scanned. This allows an engineer to quickly and easily assess the location and magnitude of defects.

2.4.2 Impact-Echo Device

A university developed a multi-sensor, air-coupled, impact-echo device that can be manually moved over a bridge deck surface of about 1000 square feet in approximately 90 minutes (Gucunski et al., 2013). The device consists of a linear microphone array which is manually moved over the surface while automatically producing impacts. This technology allows an engineer to identify and characterize defects close to the surface (Zhu and Popavics, 2007). The package includes automated data and image processing, so an engineer can receive real time visual representation of the scan (Gucunski et al., 2013).

Strengths of this device include the automated data collection and processing systems in addition to ease of use. The weaknesses include collection time, which is a significant improvement in comparison to commercial products, but would still require construction to be halted or a completed structure to be closed. Figure 2.8 shows the configuration of the device.

Figure 2.8: Impact-Echo Device University of Illinois Urbana-Champaign (Gucunski et al., 2013)

2.4.3 Non-Contact Wave Testing

A second university developed a device similar to the impact-echo device. However, instead of impact-echo, it sends leaky surface waves through an automated impact source while an array of microphones receive the signal. The data is then processed to compile a dynamic elastic modulus and yield map of pavement (Ryden et al., 2008).

This very applicable for pavement testing and integrity, but may not be the best application for concrete bridge decks, since it doesn't directly acquire data for the desired characteristics. Another significant drawback is that the machine needs to be manually pushed at a slow rate in order to receive data properly, which is not feasible for high speed demands. Figure 2.9 from Ryden et al. (2008), depicts how the microphones receive the surface waves.

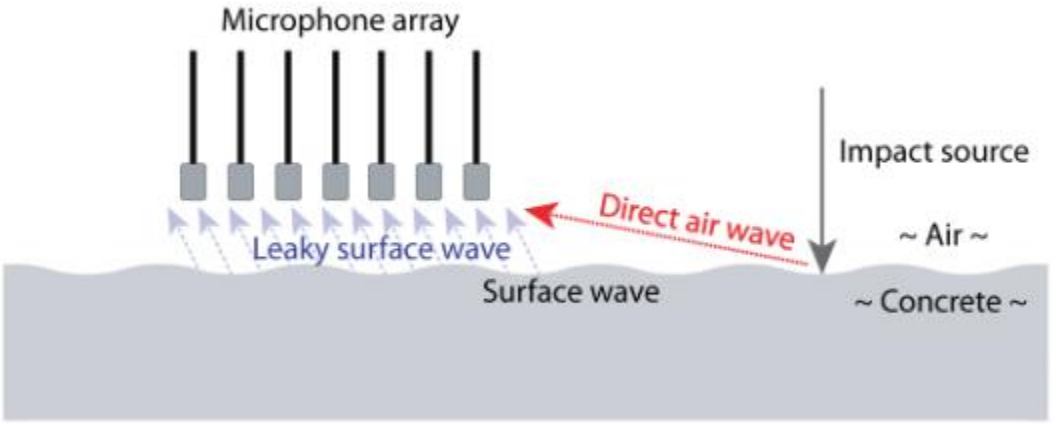

Figure 2.9: Description of Non- Contact Wave Testing (Ryden et al., 2008)

2.4.4 FLEXUS

Another ultrasonic measurement and imaging system, FLEXUS, consists of a three-axis scanner with low frequency transducers in an area of approximately of nine square feet. It uses a total of 48 transducers, arranged in three axial groups of 16, with a traditional or combination SAFT algorithm to produce images. An interesting feature allows the user to

choose between SAFT to either produce high quality images or reduce scanning time to approximately 1 minute per a square foot (Schickert, 2015). Though this increases speed, it still takes a substantial amount of time to scan an entire concrete bridge deck. Additionally, FLEXUS is primarily used for walls and other vertical structures; a horizontal scanning system is desired for this project. Figure 2.10 displays the FLEXUS configuration.

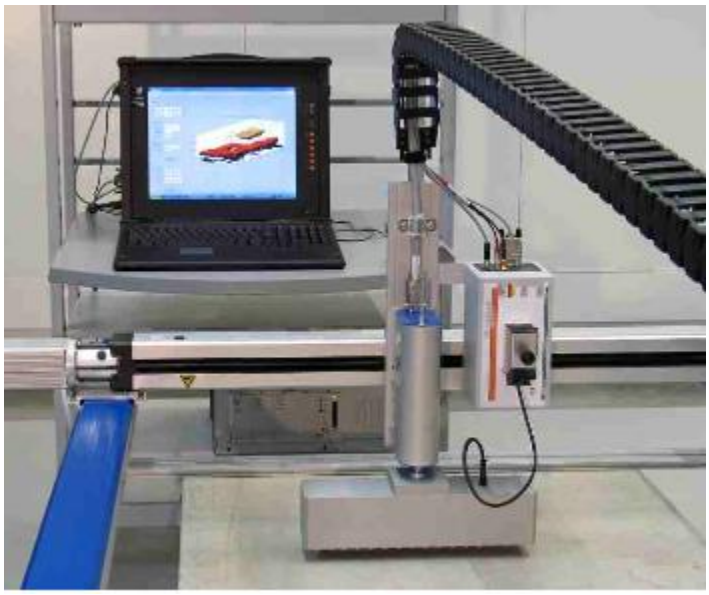

Figure 2.10: FLEXUS Multipoint Scanner (Hillger et al., 2014)

2.4.5 RABIT

Rutgers University designed an autonomous robot, named Robotic Assisted Bridge Inspection Tool (RABIT), to detect rebar corrosion, concrete degradation, delamination, and other common defects. It contains a variety of non-destructive testing equipment including; GPR, ultrasonic surface wave sensors, impact-echo, and electrical resistivity, in addition to high resolution digital camera for a clear depiction of the surface and GPS for exact location of the device. The data must be extracted to use an online data analysis tools, which produces multiple maps to represent the concrete's condition (Center for Advanced Infrastructure and

Transportation, 2014). It is a fully automated device, but with a large variety of NDT technology it requires a complex understanding to determine the best approach for various structures. Figure 2.11 depicts the RABIT configuration and shows all non-destructive technologies.

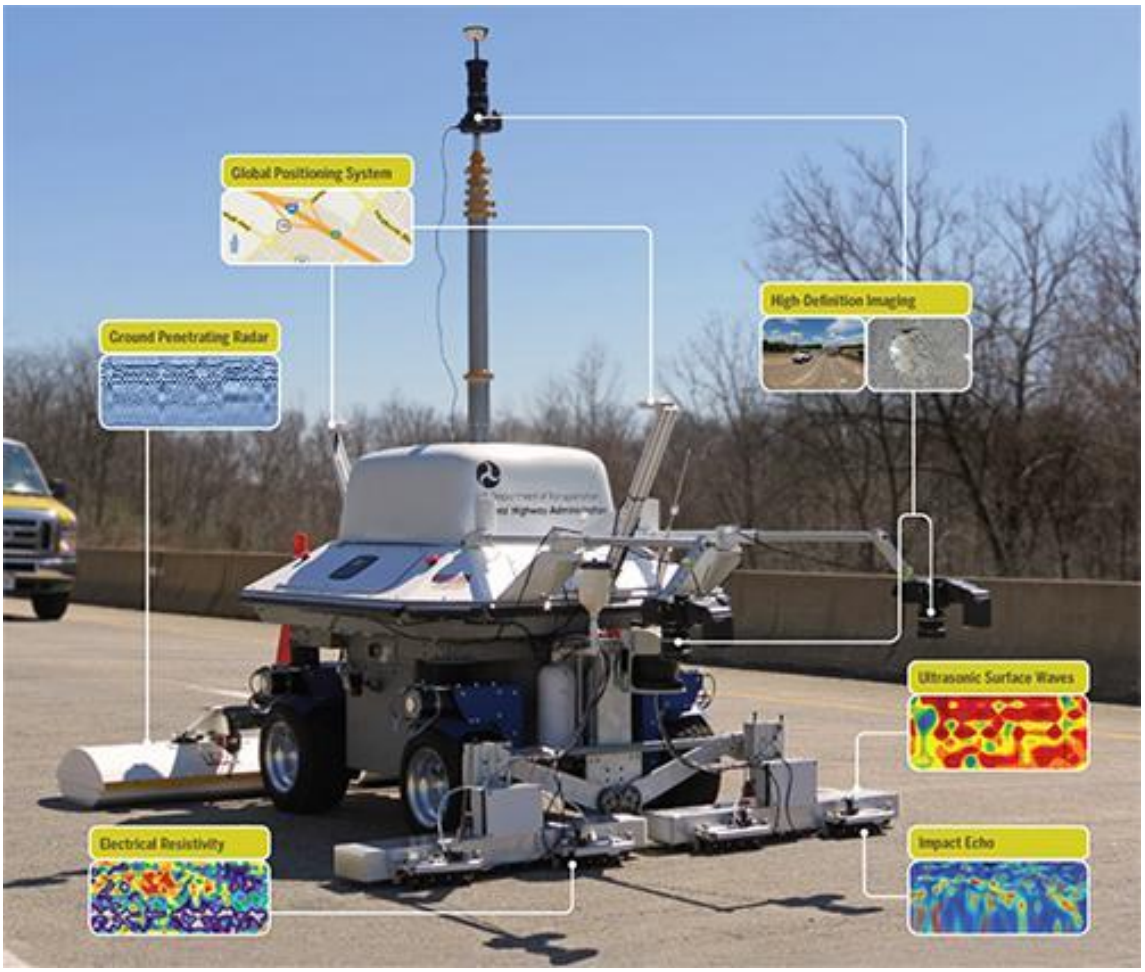

Figure 2.11: Image of RABIT (Center for Advanced Infrastructure and Transportation, 2014)

2.4.6 BetoScan

Another measurement system, the BetoScan, is a self-navigating robot consisting of both contact and non-contact sensors and uses a combination of mapping, radar, and ultrasonic techniques. It includes optical analysis, microwaves, ultrasonics, eddy current methods, and

radar. It is specifically designed to investigate the impact of deicing salts on concrete integrity since chloride is directly related to high corrosion (Kurz et al., 2009).

BetoScan uses multiple characteristics to assess the condition of concrete decks, including bridges and parking structures. These include electrochemical potential, chloride profiles, carbonation depth, cover adequacy, delamination, cracks, and corrosion. According to Reichling et al. (2009), the BetoScan can simultaneously measure the desired characteristics and cover "thousands of square meters per a day" on horizontal surfaces, due to its multisensory set up. The BetoScan also uses the ultrasonic system, A1220 Monolith, also known as EYECON, to determine structure thickness and map defects. Figures 2.12 and 2.13 depict the physical BetoScan and show the capabilities of the device and their specific use for determining characteristics, respectively.

This indicates that the A1220 Monolith is a flexible device that can be utilized in a larger, automated mobile NDT device. BetoScan, like RABIT, offers a wide variety of techniques to determine characteristics of a bridge deck, but limited mobility and a complex mechanical design make it difficult to use.

Figure 2.12: BetoScan Automated Robot (Reichling et al., 2009)

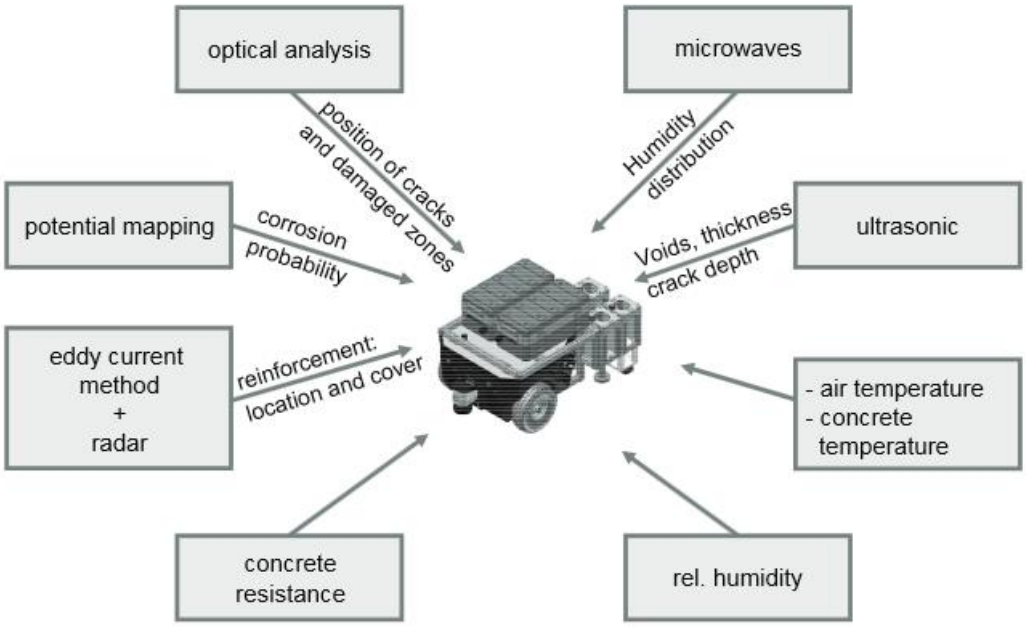

Figure 2.13: BetoScan Capabilities (Reichling et al., 2009)

2.4.7 EYECON A1120 Monolith

EYECON, also known as the A1120 Monolith, is a handheld ultrasonic tomography device. Like MIRA, EYECON is a portable device that can successfully determine concrete thickness, delamination, voids, honeycombing, and bond quality using the ultrasonic pitch-catch method in the time domain. Figure 2.14 shows the EYECON device and its included transducer array.

Figure 2.14: Transducer Array (Foreground) with EYECON Handheld Computer (Background)

Also, similar to MIRA, it uses dry point contact transducers which eliminates the need for messy contact gels. The device usually displays results as individual A-scans, which shows the reflected amplitude versus depth or C-scans, which display the bird's eye cross sectional view of the concrete being scanned. The pitch-catch method is an ultrasonic pulse-echo method where transmitting and receiving transducers are separate. The packaged transducers are bi-static and arranged in a 4 by 6 array. In Figure 2.14, the 12 transducers on the left transmit the

shear wave at 50 kHz, while the remaining 12, on the right, receive the reflected waves. A more detailed image depicting the signal emission and receiving process can be seen in Figure 2.15.

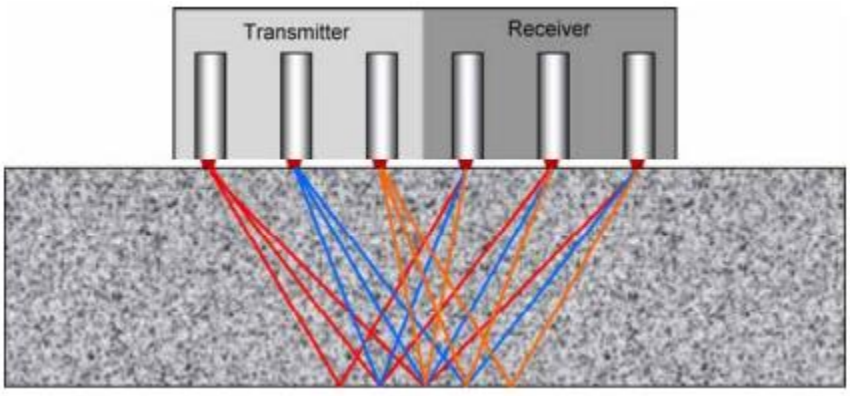

Figure 2.15: Transmitting and Receiving Configuration of EYECON (Germann Instruments, 2015)

Each transducer is spring loaded to account for surface irregularities and noise is reduced by using multiple transmitting and receiving transducers. The transducer array presented in Figure 2.14 clearly depicts the dry contact tips. This piezoceramic tip is sturdy and long-wearing.

EYECON is of particular importance, since the ultimate goal is to integrate multiple transducer arrays, shown in Figure 2.14, into a rolling, zero-intrusive ultrasonic tomography device that can easily and efficiently characterize defects below bridge deck surfaces.

2.4.8 Existing Device Conclusions

From the literature review, it is evident that current non-destructive testing devices do not meet the criteria for high speed application. They may be suited to determine defects below the concrete surface, but are unable determine defects fast and efficiently. In addition, several machines are bulky. A lightweight, portable machine is desired to quickly and effectively

produce high resolution images depicting the interior condition of a concrete structure. EYECON, a portable handheld ultrasonic device, has several desirable qualities: spring loaded transducers for proper contact, dry-coupled wear-resistant piezoceramic tips for quick measurements, and swift data collection. For these reasons, the transducer array is desirable and will be evaluated to be integrated into a fast-paced device.

3. EXPERIMENTAL PROGRAM

3.1 Introduction

Wimsatt et al. (2008) identified the need for the implementation of NDT methods into the transportation industry in order safely and efficiently identify potential hazards. It was suggested that researchers conduct demonstrations with techniques that exist, but are not widely used, such as ultrasonic tomography. In the years that followed, researchers were able to successfully apply ultrasonic tomography for the classification of defects within tunnel linings that include identifying debonding, delaminations, and moisture undetectable to the human eye (Wimsatt et al., 2013). This chapter aims to determine the applicability of ultrasonic tomography to the transportation industry in order to maintain and improve the infrastructure.

EYECON is a portable hand-held device that uses ultrasonic waves to detect flaws in concrete. It uses an array of 4 by 6 dry point contact transducers to emit and receive shear waves. This handheld ultrasonic tomography device is capable of determining the concrete thickness and detecting flaws in concrete such as; delaminations, voids, honeycombing, and other defects using ultrasonic pitch-catch methods in the time domain. The device can determine concrete thickness up to 600 mm (26.3 in.) for normal strength concrete and the accuracy of flaw depth is within 10% of the total depth of the concrete. However, it is essential that the capabilities of this device be validated using control test specimens with known conditions, before they can be used in real applications. This chapter verifies the ability of this device to detect a variety of flaws that are preconstructed into eleven concrete slabs.

3.2 Experimental Setup

A total of eleven concrete slabs with varying depth, reinforcement details, and known defects were available for conducting the experimental program. During construction of the slabs, a defect key was created that documented the exact location of the simulated defects within each slab. All slabs are nominally 1.83 m by 1.83 m (6 ft by 6 ft) in length and width, but vary in depth. Table 3.1 summarizes the slab depth, reinforcement details, defects, and the location of the defects located within each slab. Test results were compared to this documented defect key for validation. All slabs containing rebar have two mats of No. 5 rebar at depth, *d*, from the top and bottom of the slab, and at 203 mm (8.0 in.) o.c. All depths of the defects are from the top of the slab. Figure 3.1 summarizes the slabs used for testing.

Table 3.1: Summary of Concrete Slabs with Simulated Defects (Wimsatt et al., 2013)

Slab Number	Slab Depth (mm)	Reinforcement Depth, *d* (mm)	Defect	True Depth of Defect (mm)
I	305	None	None	N/A
II	457	127	Natural Crack	N/A
III	305	127	None	N/A
IV	610	None	None	N/A
V	610	127	None	N/A
VI	381	127	None	N/A
VII	381	127	0.05 mm Thin Plastic	51
VIII	381	127	0.05 mm Thin Plastic	76
IX	381	127	0.05 mm Thin Plastic	25
X	381	127	Air-Filled Void (13 mm Foam)	203
XI	381	127	Water-Filled Void (Ziploc Bag)	203

Figure 3.1: Concrete and Shotcrete Specimens at Texas A&M University RELLIS Campus, Bryan, TX

To initiate the scans, consistent settings must be established. Table 3.2 depicts the settings used during testing procedures.

Table 3.2: Instrument Settings in Map Mode

Setting Description	Setting Value
Horizontal Step (mm)	50
Horizontal Size (points)	Off
Vertical Step (mm)	50
Vertical Size (points)	Off
Depth (mm)	Varied by Slab
Frequency kHz	50
Probe Type	Double
Gain dB	75
Period Number	0.5
Accumulation	Off
TGV	On
Readings Discreteness	0.1
Input Signals Filter	On
Pulse Voltage (V)	200
Repetition Rate (Hz)	45
Base (mm)	Off
Scale	mm
Cursor	On
Transducer Orientation	Vertical or Horizontal

Figure 3.2 displays the experimental setup of the handheld ultrasonic device. The influence of the orientation of the device on the detection of flaws is also investigated for reliability purposes. Each slab was scanned with the transducer array in the vertical and horizontal orientations. The scans in the two orientations were recorded starting from the same origin, without any changes in the device settings. Figure 3.3 depicts where the origin of the grid is located, as well as the orientation of all slab images.

Figure 3.2: Experimental Setup

Figure 3.3: Origin of the Grid

Contrast allows the user to determine if a defect is located within a specimen. The same contrast level is used for both orientations for a given slab, but the level differs between slabs. Table 3.3 presents a summary of the contrast levels used for the analysis of each slab.

Table 3.3: Contrast Levels for Analysis

Slab	I	II	III	IV	V	VI	VII	VIII	IX	X	XI
Contrast Level (dB)	-10	-11	-10	-12	-14	-13	-10	-10	-10	-11	-10

The slabs were tested along a marked grid of squares. The grid is comprised of 32 rows and 32 columns. The square grids were 50 mm by 50 mm (2.0 in. by 2.0 in.), of which 32 by 31 measurements were taken, for a total of 992 individual measurements. The origin of the slab starts 127 mm (5.0 in.) from the two edges, but varied slightly from slab to slab. This grid size was chosen so that there would be overlapping scanned sections in order to obtain images with high resolution after the application of the SAFT algorithm. The transducer array is approximately 120 mm (4.7 in.) long and 80 mm (3.2 in.) wide, so a 50 mm (2.0 in.) step size, both horizontally and vertically, allows for 30 mm (1.2 in.) of overlap in one direction and 70 mm (2.8 in.) of overlap in the other. The chosen step size clearly provides a substantial amount of overlap for high resolution images.

In order to complete the settings for the scanning process, the velocity of sound through the slab material must be determined and entered into the settings. The A1040 MIRA was used to determine the average surface velocity through each slab by take five measurements at arbitrary locations. MIRA contains a fixed array that calculates the surface velocity by measuring the time it takes the wave to travel a distance of 30 mm (1.2 in.). However, this is the surface wave velocity, which has a different velocity than the shear or longitudinal waves that propagate in the medium. A more accurate way to determine the velocity through the specimen would be direct transmission, but this could not be achieved due to lack of access to both sides of the specimen. Therefore, the wave velocity obtained from MIRA is used in this

investigation, and this may induce minor errors in the localization of flaws. Table 3.4 provides the average velocity for each slab.

Table 3.4: Average Sound Velocity

Slab	I	II	III	IV	V	VI	VII	VIII	IX	X	XI
Average Velocity (m/s)	3008	2673	2893	2970	2950	2840	2635	2557	2488	2866	2498
Average Velocity (ft/s)	9869	8770	9491	9744	9678	9318	8645	8389	8163	9403	8196

3.3 Experimental Procedure

After creating a map with the settings listed in Table 3.2, the procedure for inspecting the slab specimens is described in what follows.

1. Configure a grid on top of the slab specimen using soapstone. For this section, a grid of 32 by 32 squares is used, where each square is 50 mm (2.0 in.) by 50 mm (2.0 in.). As shown in Figure 3.3, the origin of the grid is placed approximately 127 mm (5.0 in.) from the corners.

2. With the transducer in the vertical orientation, take the first scan at the origin with the edges of the transducer aligned with the X and Y-axis of the grid. While on the map screen, the A-Scan will appear on the right hand side. Press the transducer down in order to ensure proper contact with the concrete and press “Enter” to take the scan.

3. Continue to hold the transducer until the measurement is recorded on the Map screen. The device will beep when the measurement has been recorded.

4. Move the transducer 50 mm (2.0 in.) along the positive X-axis as shown in Figure 3.3, aligning the edges of the transducer with the X-axis and the first line parallel to the Y- axis. Press “Enter” to take the measurement.

5. Continue to take measurements across the first row using the same procedure listed in Step 4.

6. After the first row is complete, move the transducer to the origin and then 50 mm (2.0 in.) along the positive Y-axis to the second row. Move the cursor on the Map screen to match this point. Take measurement by pressing “Enter”.

7. Continue taking measurements, one at a time, in the horizontal direction until the second row is complete, then repeat the process for Rows 3 through 32, until the entire slab has been scanned.

8. Upload data into a storage device.

A visualization software was used to obtain refined C-scans of the specimens. Negative contrasts are used in order to have the defects appear bright red during the analysis. The contrast must be adjusted in order to determine if a defect is present within the concrete. Initially, without contrast, the entire slab appears red, which is the default setting. The user must adjust contrast in order to accurately locate defects. For these concrete specimens, most contrast levels are between -10 and -15 dB. After the appropriate contrast settings are applied, unaffected concrete appears as various tones of blue due to the non-homogeneous nature of concrete. The procedure is described next.

1. Open the *map.cfg* file from the folder containing the files from the scan.
2. Wait for the file to load and configure.
3. Click the settings button to ensure required settings are applied, they can be changed at this point if necessary.
4. Press the +/- buttons in the top right corner to adjust the contrast level to clearly see defects within the slab. Most slabs were analyzed with a contrast level between -10 and -15 dB.
5. Use arrows in the left side to move through the slab is the X, Y, and Z directions to see the D, B, and C scans, respectively.

The above procedures were followed for the scans using both the vertical and horizontal transducer orientations, and the results were compiled for each slab. The scans are analyzed in depth and compared to the slab key to determine if the defects were accurately located.

3.4 Experimental Results

3.4.1 Plain Slabs

Slabs that contained no rebar or stimulated defects are discussed in this section. These include Slab I and IV that are 305 mm (12.0 in.) and 610 mm (24.0 in.) deep, respectively. From the results of the scan measurements, the depth of the two slabs were estimated to be 300 mm (11.8 in.) and 610 mm (24.0 in.), which compares well with the actual thicknesses of the slab. Figure 3.4(a) and Figure 3.4(b) show representative C-scan images from Slab I and IV. The analysis of C-scans from the two slabs predominantly revealed blue contrast, with slight variations in tone. The various tones of blue found in Figure 3.4 and additional images

in Appendix A are due to the non-homogeneous nature of the concrete. The lack of any major contrast in the C-scans suggests that there no defects or reinforcement within these slabs. These findings correspond well with the defect key. However, the C-scans of Slab IV, revealed the presence of a small defect at a depth of 330 mm (13.0 in.), which is not documented in the defect key. This is likely due to the hollow formwork that was used to construct the slab that may have accumulated water or debris.

Scans from the vertical orientation and horizontal orientation of the device were also compared to each other. Irrespective of the orientation of the device, similar results were obtained in terms of the overall depth, and the absence of defects and reinforcement in the slab. The location of the lighter blue tones are similar, although not completely identical. There are no notable variations in contrast of the C-scans to indicate the possibility of defects within the slabs. From both transducer orientations, it is evident that the slab is clear of significant imperfections and both scans produce similar information. Additional C-scans at various depths of Slab I and IV can be found in Appendix A.

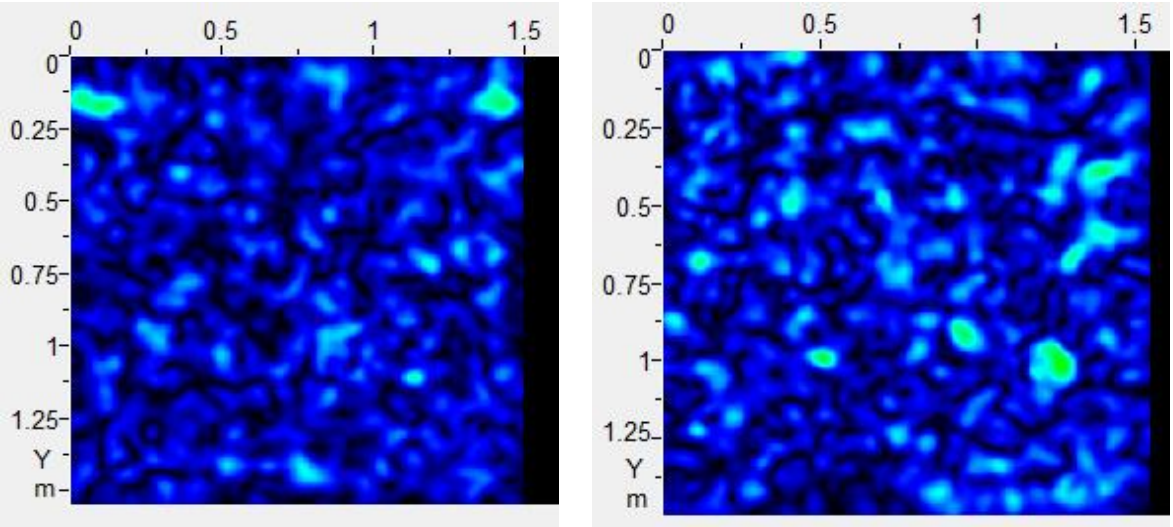

(a) Slab I at a Depth of 150 mm (5.9 in.)

(b) Slab IV at a Depth 180 mm (7.1 in.)

Figure 3.4: C-Scans of Plain Slabs

3.4.2 Reinforced Slabs without Defects

This section discusses reinforced slabs without any simulated defects. This includes Slabs II, III, V, and VI. The overall depth of Slab II and III are 457 mm (18.0 in.), and 305 mm (12.0 in.), respectively, whereas Slab V has a total depth of 610 mm (24.0 in.) and Slab VI has an overall depth of 381 mm (15.0 in.). All slabs contain two layers of No. 5 rebar at a depth of 127 mm (5.0 in.) from the top and bottom surface of the slab, without any simulated defects.

A review of the C-Scan images of the slabs does not reveal any features before a depth of 100 mm (3.9 in.). A grid develops at an approximate depth of 100 mm (3.9 in.) with the contrast becoming most apparent at depths of 120 mm (4.7 in.) and 130 mm (5.1 in.). Figure 3.5 shows the C-scans of all the reinforced slabs at a depth of 120 mm (4.7 in.) or 130 mm (5.1 in.). From these images, it is evident that the grid shape corresponds to the first layer of reinforcement. The image visualization program reads only to the nearest centimeter and the images shown in Figure 3.5 have the greatest contrast area between depths of 120 mm (4.7 in.) and 130 mm (5.1 in.). This corresponds to the actual depth of the rebar at 127 mm (5.0 in.) from the surface of the slab. The diameter of a No. 5 bar is 16 mm (0.63 in.), and at locations where the horizontal and vertical rebar overlap the overall diameter is 32 mm (1.3 in.). The images reflect the first indication of the rebar at a depth of 100 mm (3.9 in.), which is within 11 mm (0.43 in.) of the actual edge of the first layer of rebar at a depth of 111 mm (4.7 in.). A depth of 111 mm (4.7 in.) is where the layer should start to emerge at points where the horizontal and vertical rebar overlap. This difference is off by 2.4% of the total depth of the slab, which is well within the manufacturer's tolerance of 10% of the total depth of the specimen.

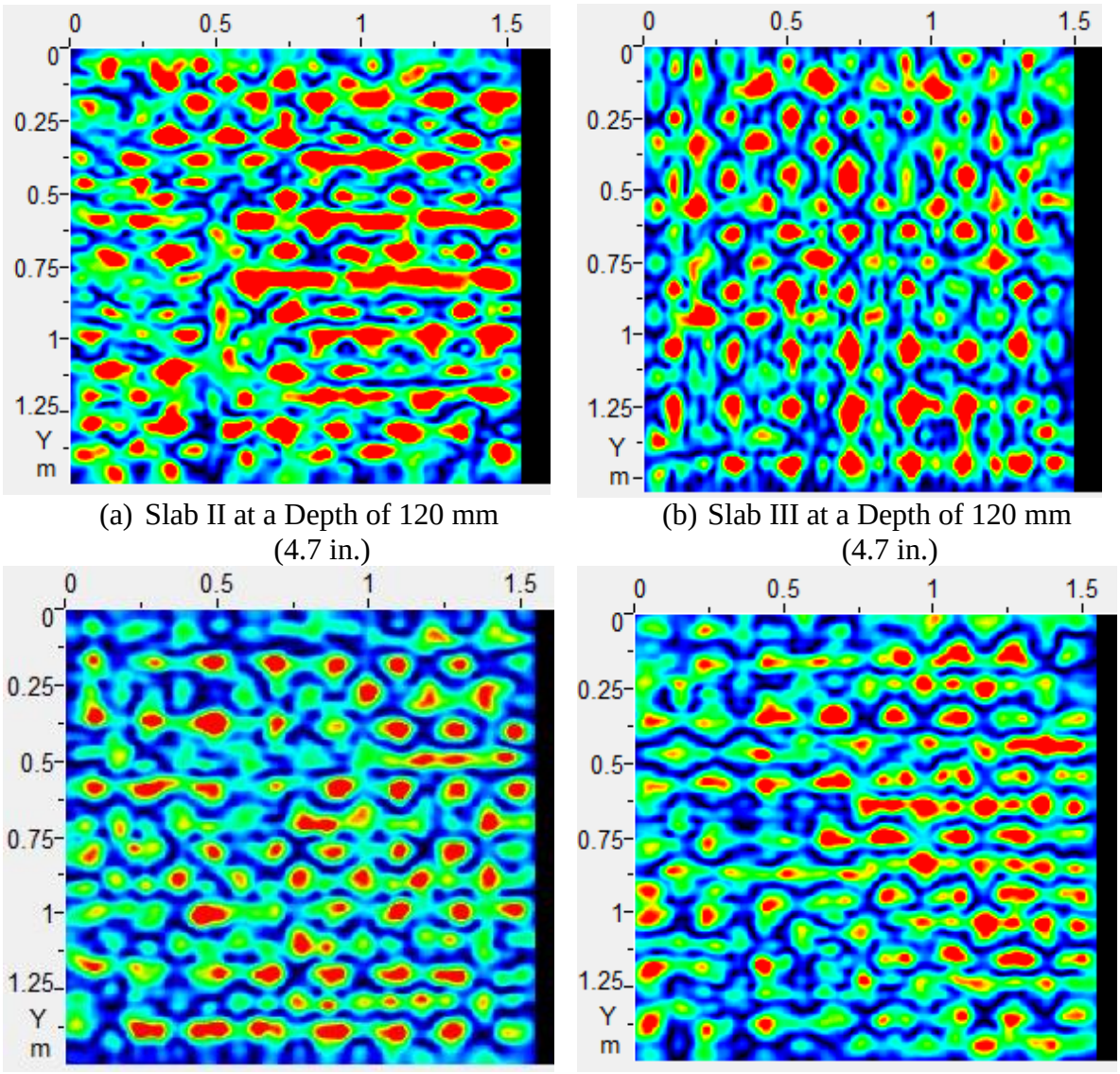

(a) Slab II at a Depth of 120 mm (4.7 in.)

(b) Slab III at a Depth of 120 mm (4.7 in.)

(c) Slab V at a Depth 130 mm (5.1 in.)

(d) Slab VI at a Depth of 120 mm (4.7 in.)

Figure 3.5: C-Scans of Reinforced Slabs without Defects

Since the depth of each slab differs, the location of the second layer of rebar in each slab differs as well. In Slab II, a second rough grid image emerges at a depth of 330 mm (13.0 in.), but become more apparent at a depth of 370 mm (14.6 in.). The center of the second layer of reinforcement is at an actual depth of 330 mm (13.0 in.). The scan provides a good indication of the second layer of rebar. The lower accuracy may be attributed to the greater attenuation

of the ultrasonic waves. The end of the concrete slab is estimated to be at 460 mm (18.1 in.), 3 mm (0.12 in.) greater than the actual depth of 457 mm (18.0 in.). It is important to note that the shallow natural crack on the surface of Slab II, which is visible, was not detected by the scan measurements. However, these surface cracks are not deep enough to affect the internal integrity of the slab.

In the case of Slab III, the second layer of rebar appears at a depth of 210 mm (8.3 in.), with a more well-defined grid emerging at a depth of 220 mm (8.7 in.). The actual depth of the second layer of No. 5 rebar is at a depth of about 180 mm (7.1 in.). This discrepancy in the estimated depth of the second reinforcement layer may be attributed to the close proximity of the two layers of rebar. A significant amount of the wave energy gets reflected back to the transducers after encountering the first layer of rebar, which limits the amount of wave energy hitting the second layer of rebar. Overall, the system does detect the second layer and is within 30 mm (1.2 in.) of its exact location, which is within the manufacturer's 10% margin of error for a 305 mm (12.0 in.) thick slab. The overall depth of the slab is estimated to be 300 mm (11.8 in.), which compares well with the actual depth of the slab of 305 mm (12.0 in.).

C-Scan images of Slab V do not show the presence of any defects or reinforcement between depths of 150 mm (5.9 in.) to 480 mm (18.9 in.). At 480 mm (18.9 in.) a vague grid starts to appear, with it being most clear at a depth of 530 mm (20.5 in.). However, the documented depth of the second layer of rebar is at 480 mm (18.9 in.). The error of 50 mm (2.0 in.) in locating the second layer of reinforcement is again attributed to the greater attenuation of the ultrasonic waves as the waves travel deeper into the reinforced concrete slab. This may alter the signal and slightly skew the depth of the second layer of reinforcement, but is still within the device's 10% accuracy.

Similar to Slab V, C-Scan images of Slab VI do not show any red contrast from a depth of 150 mm (5.9 in.) to a depth of 280 mm (11.0 in.). At 280 mm (11.0 in.), the second layer of rebar appears as a faint grid, with it becoming more apparent at 300 mm (11.8 in.). The estimated depth of the reinforcement layer is 46 mm (1.8 in.) away from the actual location of the reinforcement at 254 mm (10.0 in.). This results in an accuracy of 12% of the overall depth of the slab, which is slightly above the manufacturer's 10% accuracy limit. This difference is once more attributed to the attenuation of ultrasonic waves. The bottom of the slab was determined to be at 380 mm (15.0 in.) which corresponds closely with the actual depth of 381 mm (15.0 in.).

A comparison of the scans from the vertical and horizontal orientation of the transducers provided similar results. Both scan orientations indicate the first signs of rebar at a depth of approximately 100 mm (3.9 in.) with it being most visible between depths of 120 mm (4.7 in.) and 130 mm (5.1 in.) for all the reinforced slabs. Both orientations clearly depict the location of the first layer of rebar, though the images are slightly different. Additional C-Scan images for these slabs can be found in Appendix A. The vertical orientation of the transducer shows the rebar parallel to the X-axis more clearly, while the horizontal orientation of the transducer shows the rebar parallel to the Y-axis better. This is due to the orientation of the waves emanating from the emitting transducers. Since the waves propagate in a different direction depending on the transducer orientation, they are able to locate either the horizontal or vertical rebar more clearly. Though these images are slightly different, the location and depiction of the rebar is unmistakable, meaning both orientations provide reasonable images of the interior condition of the slab at various depths. Though the images are clear and provide reasonable results, this indicates that the device may have difficulty detecting defects that are

parallel to the device's orientation. Overall, the system successfully locates two layers of rebar and their approximate locations for each slab, with less accuracy in locating the second layer.

3.4.3 Reinforced Slabs with Thin Plastic Defects

This section discusses reinforced slabs that contain simulated 0.05 mm thin plastic defects. These include Slabs VII, VIII, and IX. All slabs are 381 mm (15.0 in.) thick, and contain two layers of rebar at 127 mm (5.0 in.) and 254 mm (10.0 in.), with varying depths of the thin plastic defect.

Slab VII has a plastic defect at a depth of 51 mm (2.0 in.) from the top surface. The C-Scan images did not display any contrast between 0 mm to 60 mm (2.4 in.). At around 60 mm (2.4 in.), a faint square appears but becomes clearer at 70 mm (2.8 in.), and is most apparent at a depth of 80 mm (3.2 in.) as demonstrated in Figure 3.6(a). The initial indication of the plastic defect at 60 mm (2.4 in.) is relatively close to its actual depth of 51 mm (2.0 in.). The difference of 9 mm (0.35 in.) corresponds to 2.4% accuracy. It is also important to note that the actual defect is only 0.05 mm (0.002 in.) thick, but the C-Scan images show the presence of the defect from a depth of 60 mm (2.4 in.) to 190 mm (7.5 in.). This is because the ultrasonic waves do not penetrate through the defect, therefore, creating a shadowing effect beyond the initial location of the defect.

Similar to Slab VII, a square defect starts to emerge in Slab VIII at a depth of approximately 80 mm (3.2 in.) with it becoming more apparent at a depth of 90 mm (3.5 in.), as displayed in Figure 3.6(b). The first sign of the defect at a depth of 80 mm (3.2 in.), corresponds well with the actual location of the defect located at a depth of 76 mm (3.0 in.).

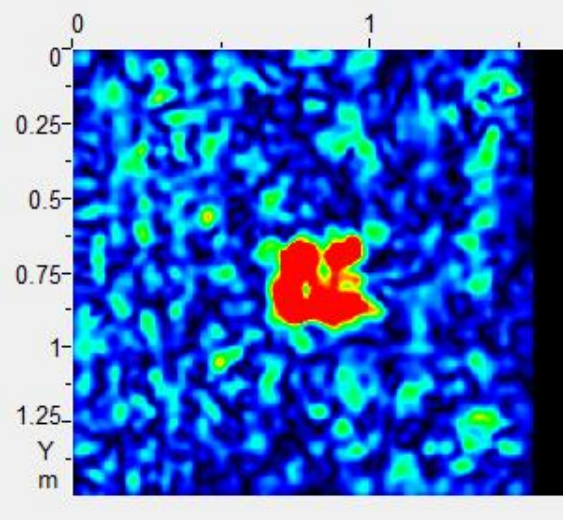

(a) C-Scan of Slab VII at a Depth of 80 mm (3.2 in.)

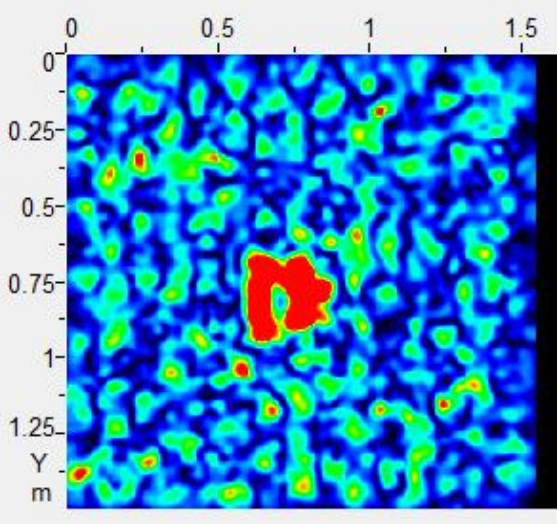

(b) C-Scan of Slab VIII at a Depth of 90 mm (3.54 in.)

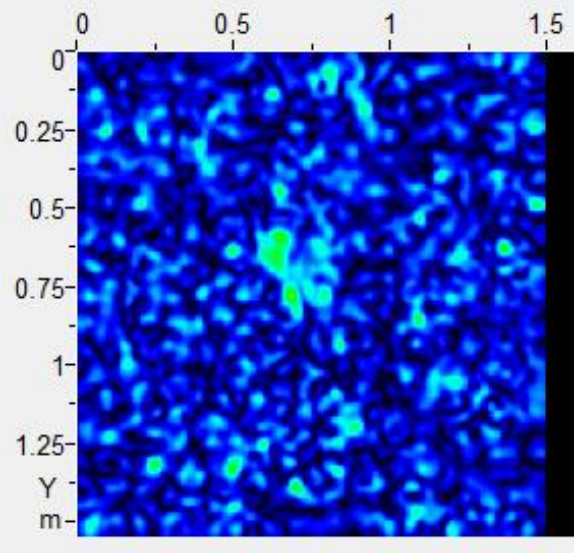

(c) C-Scan of Slab IX at a Depth of 30 mm (1.2 in.)

Figure 3.6: C-Scans of Reinforced Slabs with Thin Plastic Defects

In Slab IX, the thin plastic defect that is located at a depth of 25 mm (1.0 in) from the top surface of the slab but it was not positively detected by the ultrasonic tomography device. In Figure 3.6(c), a small portion of the defect can be seen, but it is not as prominent as other plastic defects.

In the case of Slab VII and VIII, since ultrasonic waves are generally unable to penetrate through the plastic defect, a shadowing effect can be seen throughout the slab. Whole or partial images of the square shape can be seen at various depths further than the location of the defect. Also, at the bottom of the slab, a rough square outline can be seen in blue tones with the rest of the image being a deep red tone.

Additionally, in all three slabs, a layer of reinforcing steel appears at a depth of 100 mm (3.9 in.) with it most prominent at depths between 120 mm (4.7 in.) and 130 mm (5.1 in.) from the top of the slab. This is close to the actual location of the rebar which ranges between 110 mm (4.3 in.) and 150 mm (5.9 in.). After a depth of approximate 160 mm (6.3 in.) the first layer of steel disappears in the C-Scan. This is reasonable since at overlapping points of vertical and horizontal rebar the total diameter is 32 mm (1.3 in.). The second layer of rebar in each slab is not as clear as the first because of the attenuation of ultrasonic waves, as in previous cases. For Slab VII, the lattice is most visible at 290 mm (10.6 in.), while in Slabs VIII and IX it is most prominent at 270 mm (10.6 in.) and 250 mm (9.4 in.), respectively. The second layer has a documented located of 254 mm (5.0 in.) in all cases. The difference ranges from 4 mm (0.16 in.) to 36 mm (1.4 in.). The differences in depth over the total depth of the slab is within 10%, within the manufacturer's tolerance. Slab VII and IX are determined to be 380 mm (15.0 in.) thick, while Slab VIII is determined to be 370 mm (14.6 in.), which are close to the actual documented depth of 381 mm (15.0 in.) for each slab.

When comparing the transducer orientations, no undocumented defects were detected. The difference is that the vertical orientation shows the left and bottom edges of the plastic defect more clearly, while the horizontal orientations show the top and bottom edges. The actual depth of the plastic defect is only 0.05 mm (0.002 in.) thick in all the slabs. However,

they are present in a majority of the C-Scans beyond the initial appearance of the defect, indicating that the device is unable to accurately depict the thickness of the defect. Additional images for Slabs VII, VIII, and IX can be found in Appendix A.

3.4.4 Reinforced Slabs with Air-Filled Voids

This section discusses reinforced slabs that contain air-filled voids. The overall depth of Slab X is 381 mm (15.0 in.), and it contains two layers of rebar at 127 mm (5.0 in.) and 254 mm (10.0 in.). The air-filled void is simulated using a 13 mm (0.51 in.) thick piece of foam and is located at a depth of 203 mm (8.0 in.). Slab X also has a noticeable crack on the surface of the slab, but it was not detected by the ultrasonic tomography device. Similar to the other slabs, a rebar grid emerges at a depth of approximately 100 mm (3.9 in.). The grid is most clearly visible at a depth of 130 mm (5.1 in.). This corresponds to the first layer of rebar. After the first layer of rebar, a defect starts to appear approximately in the center of the slab at a depth at 210 mm (8.3 in.). As shown in Figure 3.7, the defect becomes most apparent at a depth of 220 mm (8.7 in.).

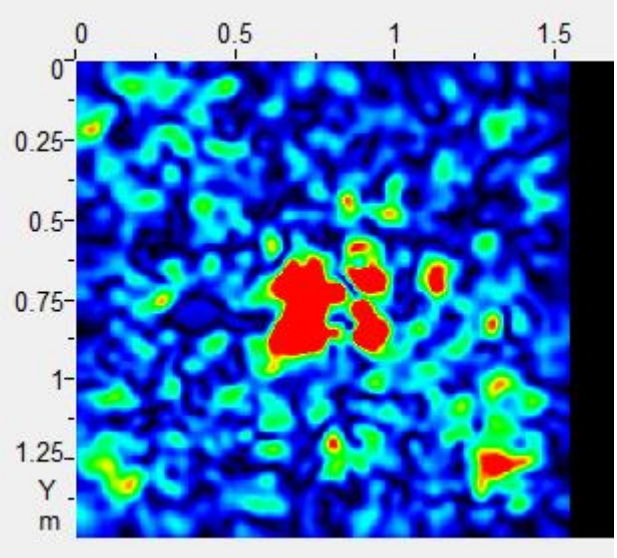

Figure 3.7: C-Scan of Slab X at 220 mm (8.7 in.)

The defect can also be seen at 230 mm (9.1 in.) and 250 mm (9.8 in.). The difference in contrast was evident in C-scans up to a depth of 250 mm (9.8 in.). The recorded bottom edge of the foam is located at 218 mm (8.58 in.), while the measured bottom edge is at 250 mm (9.8 in.), a difference of 32 mm (1.3 in.), which is within the acceptable 10% accuracy specified by the manufacturer. Beyond this point, small reflections may be observed. However, they are not well defined, and therefore are not considered to be part of the defect. The device was not able to clearly locate the second layer of rebar which is located at a depth of approximately 254 mm (10.0 in.) from the top of the slab. In Figure 3.7, some contrast can be seen around the air-void, this may be due to the limited amount of wave energy reaching this depth. From the measurements, the slab is determined to be 380 mm (15.0 in.) thick, which is very close to the actual slab thickness though the bottom of the slab is not as clear when compared with other slabs. This may be due to the limited wave energy traveling the whole depth of the slab due to a significant amount of energy being reflected by the rebar and air-void.

A comparison is also made between the scan measurements obtained from the horizontal and vertical orientations of the transducers. The crack on the surface of Slab X did not penetrate the surface and was not detected by either transducer orientation. No defects were detected in Slab X, by either scan measurements, up to a depth of 100 mm (3.9 in.). At a depth of 100 mm (3.9 in.), both scans show the emerging rebar, centrally located at a depth of 127 mm (5.0 in.). Similar to other comparisons, the vertical transducer orientation displays a clear image of the horizontal rebar, whereas with the horizontal orientation the vertical rebar is more apparent. Though the scans are not identical, they provide similar information and clearly indicate the location and presence of the reinforcing steel. A defect starts to appear in Slab X at a depth of 210 mm (8.3 in.), and the air-filled void becomes more apparent at a depth of 220

mm (8.7 in.) for both transducer orientations. The two separate scans indicate the defect is present from a depth of 210 mm (8.3 in.) through 250 mm (9.8 in.). The scans show a shadow beyond the location of the defect due to the shadowing effect that was previously described. Most importantly, the scans correspond to one another at every point throughout the slab, though they are not identical. Neither scan was able to clearly identify the second layer of rebar, but with some experience the user can see suggestions that it is present within the slab. Further information regarding Slab X can be seen in Appendix A.

3.4.5 Reinforced Slabs with Water-Filled Voids

Slab XI is a reinforced concrete slab that is 381 mm (15.0 in.) thick. The slab has two layers of reinforcement at depths of 127 mm (5.0 in.) and 254 mm (10.0 in.). The water-filled void is simulated by embedding a Ziploc bag filled with water. The defect is located at a depth of 203 mm (8.0 in.) from the surface of the concrete slab. From the C-scans, it is evident that no defects are present up to a depth of 90 mm (3.5 in.). At approximately 90 mm (3.5 in.), a grid pattern emerges and is thickest at a depth of 120 mm (4.7 in.), indicating the presence of rebar. This corresponds well with the actual location of the rebar which is located at a depth of 127 mm (5.0 in.). In the C-scan images, at a depth of 200 mm (7.9 in.), a change in color begins to faintly appear in the center of the slab. However, as displayed in Figure 3.8, the contrast is highest at a depth of 210 mm (8.3 in.).

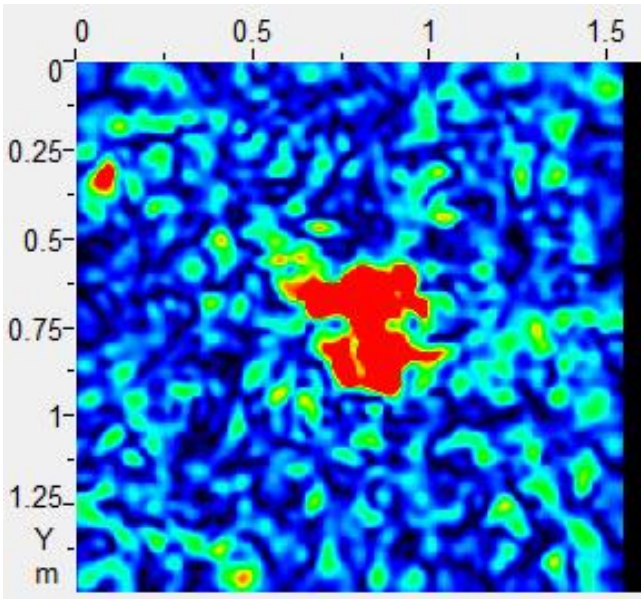

Figure 3.8: C-Scan of Slab XI at 210 mm (8.3 in.)

Beyond this point it begins to dissipate and disappears completely after a depth of 250 mm (9.8 in.). This compares well with the actual location of the water defect, which is located at a depth of 203 mm (8.0 in.) from the top of the slab. The ultrasonic tomography results also accurately determine the thickness of the defect, unlike plastic or air defects. The estimated thickness of the defect is 50 mm (2.0 in.), which is close to the actual defect thickness of 58.4 mm (2.3 in.). After the defect, a faint rebar grid appears thickest at a depth of 300 mm (11.8 in.). The reflection of the water-void is also seen in the bottom of the slab. This was observed in all slabs with an artificial defect near the center of the slab, with it being least prevalent in the case of the air-void, Slab X.

From scans using two different transducer orientations, Slab XI was determined to be roughly 380 mm (15.0 in.) deep. Each scan successfully identified two layers of rebar and a water-void and did so at the same depths, providing identical results. This indicates that transducer orientation does not significantly affect the device's abilities in identifying water-

filled voids in reinforced concrete slabs. Additional images of Slab XI can be seen in Appendix A.

3.5 Comparison of Image Quality from Overlapping and Non-overlapping Scans

Ultrasonic tomography relies on the SAFT algorithm to construct complete 2-D or 3-D images from a compilation of individual pulse echo scans. The scans typically overlap one another in order to produce a higher resolution image. The clarity produced by using overlapping images can help when identifying defects within a concrete component. High resolution images come with a cost since more overlap requires a greater number of scans. This task aims to determine if defects can still be detected to a sufficient level of detail without the use of overlapping scans. Figure 3.9 shows the difference between the grids with overlap, and no overlap. The black rectangle represents the transducer with the vertical orientation in reference to the grid.

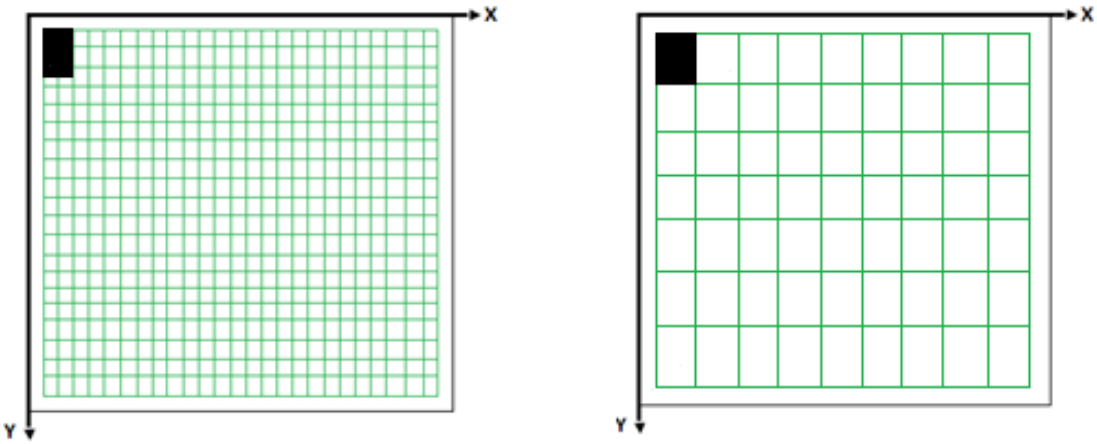

(a) For Overlapping Scans. (b) For Non-Overlapping Scans.

Figure 3.9: Grid with Overlapping vs without Overlapping Measurements

In Figure 3.9(a), a grid is shown that is representative of each square being 50 mm (2.0 in.) along the X-axis by 50 mm (2.0 in.) along the Y-axis, which allows for a minimum of 30 mm (1.2 in.) overlap for the 80 mm (3.2 in.) by 120 mm (4.7 in.) transducer. Figure 3.9(b)

displays a grid that was used for no overlap with the transducer in the vertical orientation. This means the shorter side of the transducer is parallel to the X-axis, so each rectangle is 80 mm (3.2 in.) along the X-axis and 120 mm (4.7 in.) along the Y-axis. To scan the slab with no overlap in the horizontal orientation, each rectangle in the grid would be 120 mm (4.7 in.) parallel to the X-axis and 80 mm (3.2 in.) parallel to the Y-axis.

Slab VIII was chosen to investigate the effects of overlapping scans since it contains a defect as well as two layers of rebar. Comparison of overlapping and non-overlapping scans in both the vertical and horizontal transducer orientation is critical for project feasibility. The two orientations with overlapping measurements were analyzed with a contrast of -10 dB, while the two orientation with non-overlapping measurements were analyzed with a contrast of -5 dB. The non-overlapping scan is not as refined and therefore requires less contrast to see defects.

Figure 3.10 shows a comparison of the C-scans at a depth of 30 mm (1.2 in.), obtained with and without overlapping scans with the vertical and horizontal orientation of the transducer. No defects are revealed in any of the four C-scan images presented in Figure 3.10, which corresponds with the actual condition of Slab VIII. Figure 3.10(c) and (d) do not have the same resolution as the images in Figure 3.10 (a) and (b), but they are able to convey identical information to the user.

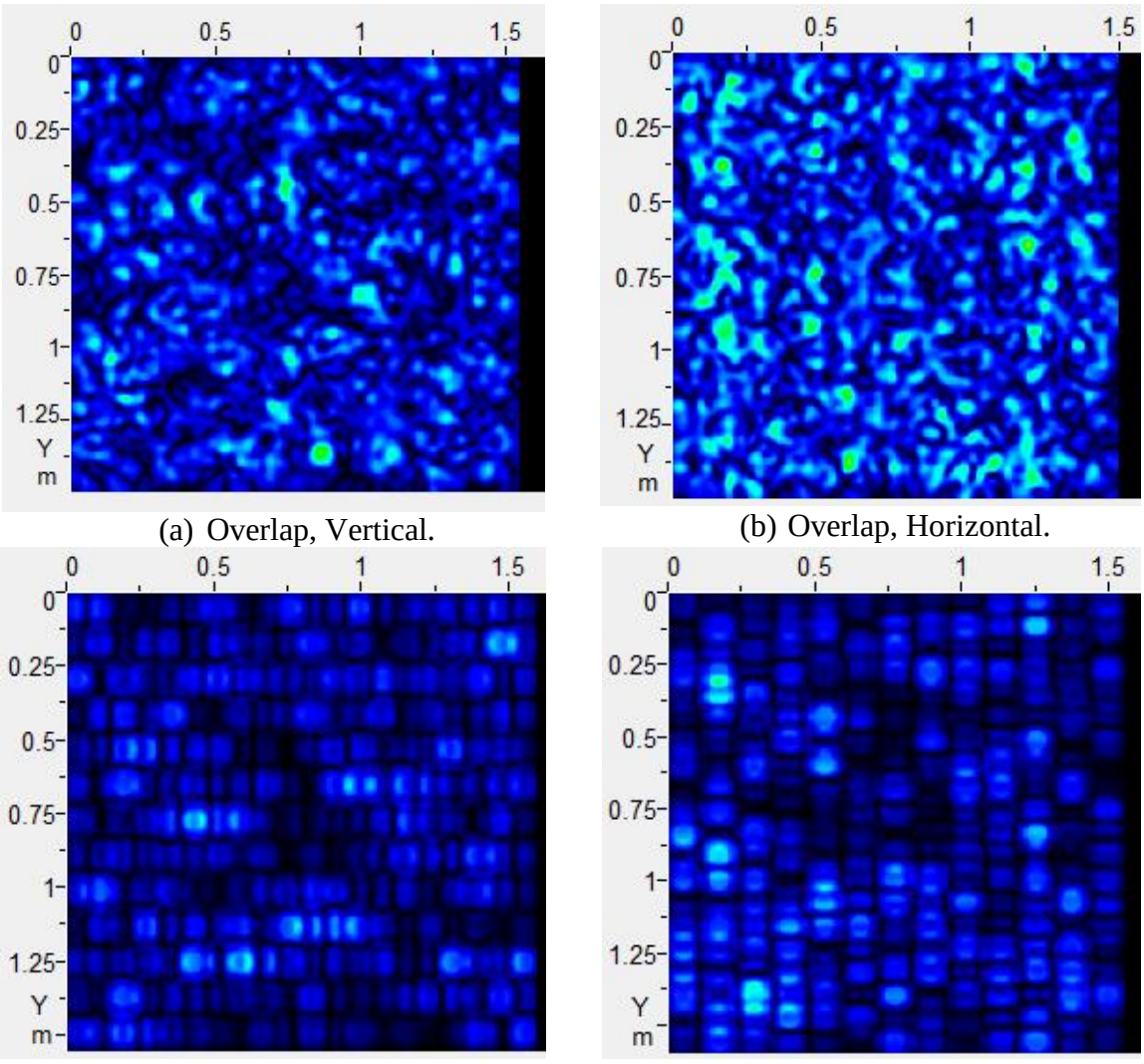

(a) Overlap, Vertical. (b) Overlap, Horizontal.

(c) No Overlap, Vertical. (d) No Overlap, Horizontal.

Figure 3.10: Comparison of C-Scans Obtained from Scan with and without Overlap – Slab VIII at a Depth of 30 mm

Figure 3.11 compares the scans at a depth of 80 mm (3.2 in.). As shown in Figure 3.11(a) and (b), the plastic defect is clearly visible near the center of the slab with measurement overlap. Figure 3.11 (c) depicts a vertical transducer orientation with no overlap. In this image, red portions are indicative of the thin plastic defect, but the resolution is limited and only an experienced eye would be able to identify these red marks as a defect. Figure 3.11 (d), the

horizontal scan with no overlap, has a better clarity than Figure 3.11 (c), vertical no overlap, showing a slightly more defined square defect near the center of the slab.

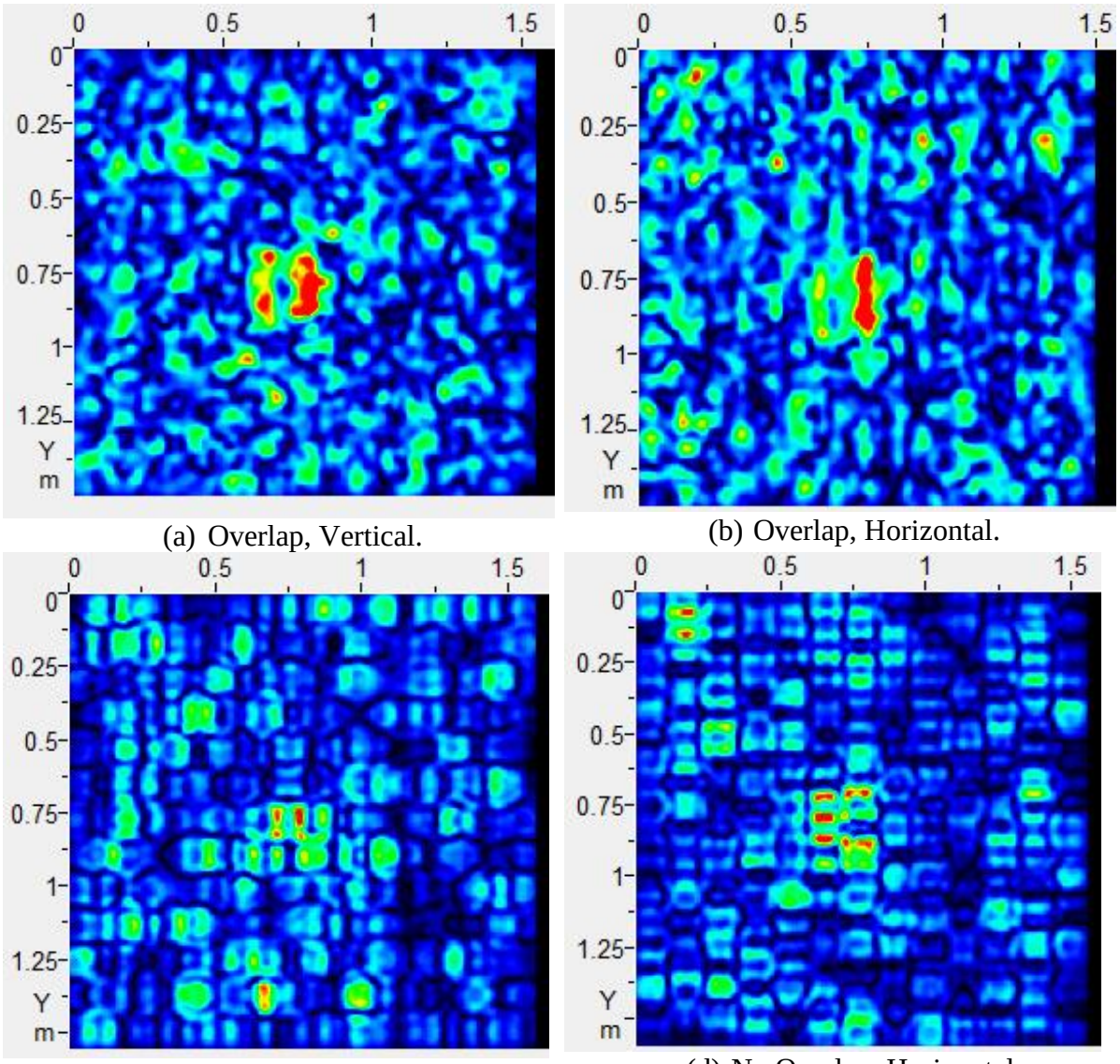

(a) Overlap, Vertical. (b) Overlap, Horizontal.

(c) No Overlap, Vertical. (d) No Overlap, Horizontal.

Figure 3.11: Comparison of C-Scans Obtained from Scan with and without Overlap – Slab VIII at a Depth of 80 mm

Figure 3.12 shows a comparison of C-scan images at a depth of 100 mm (3.9 in.). Rebar emerges at a depth of 100 mm (3.9 in.). With overlapping measurements, seen in Figure 3.12(a) and (b), the thin plastic defect is prominent at the center of the slab, with the shape of the

reinforcing steel grid surrounding it. With no overlapping measurements, the thin plastic defect can still be identified unmistakably near the center of the slab as shown in Figure 3.12(c) and (d), but the rebar is not as evident. It is more evident at 100 mm (3.9 in.) than at 80 mm (3.2 in.) for the scans taken with no overlapping measurements, indicating that the depth may not be as accurate but the device can still locate the defect within 10% of the total depth.

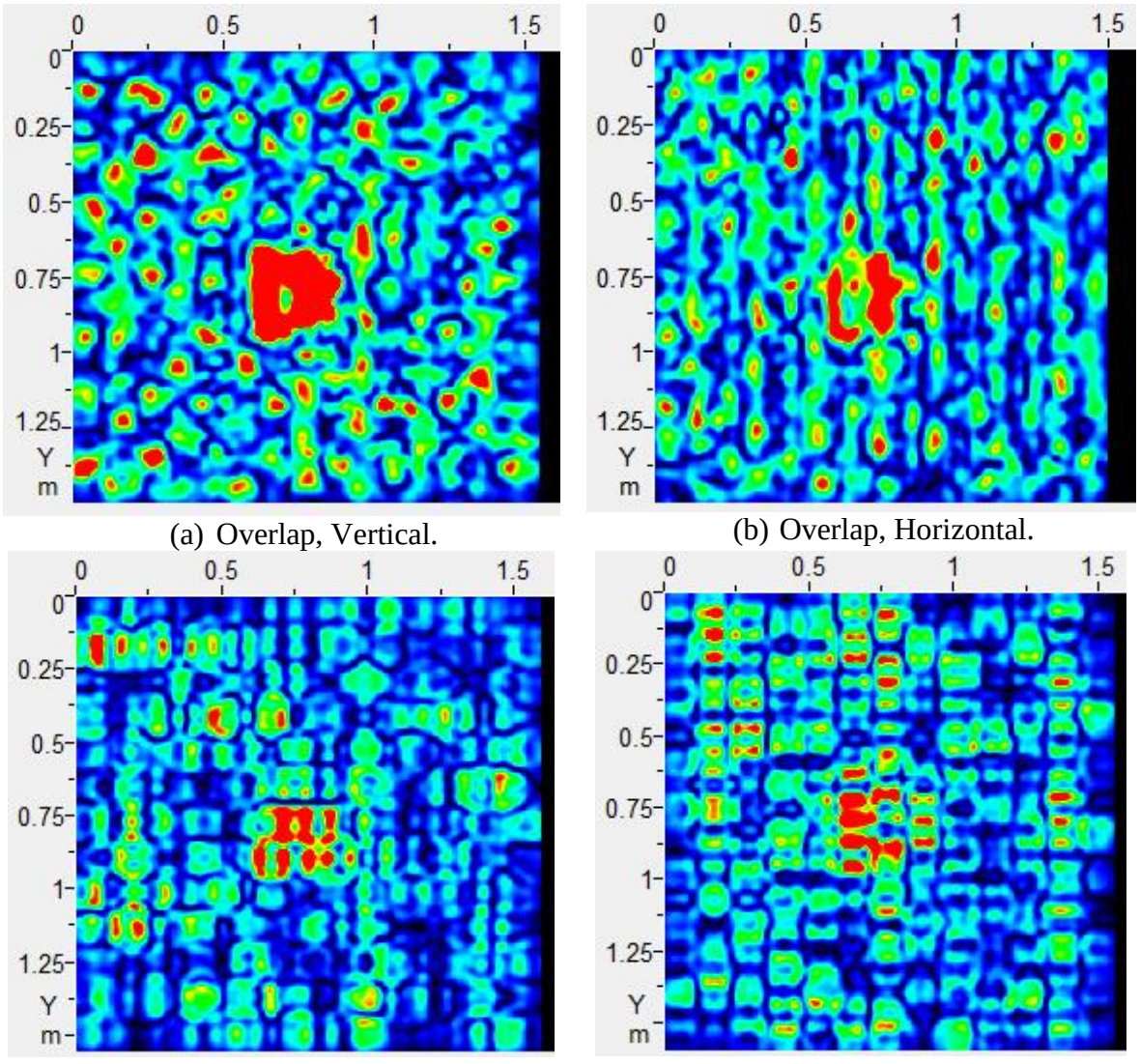

(a) Overlap, Vertical. (b) Overlap, Horizontal.

(c) No Overlap, Horizontal. (d) Overlap, Vertical.

Figure 3.12: Comparison of C-Scans Obtained from Scan with and without Overlap – Slab VIII at a Depth of 100 mm

3.6 Conclusion

Table 3.5 provides a summary of the defects detected in each slab. If the slab contained reinforcing steel, the first layer is described in the table. Slabs that contained an artificial defect are also described in the summarizing table. The error ranges from 0.66 to 2.3 percent for the detection of reinforcement. For defects, the error range is from 1 to 2.4 percent. Error in Table 3.5 is defined as the absolute value of the detected depth minus the actual depth divided by the total depth of the slab and is presented in the accuracy over depth column as a percentages. Table 3.6 summarizes the device's accuracy when determining specimen thickness. Errors for determining thickness ranged from 0 to 2.9 percent. Error in Table 3.6 is defined as the actual depth minus the detected depth over the actual depth.

Table 3.5: Summary of Defects

	Reinforcement			Defect		
Slab Number	**True Depth (mm)**	**Determined Depth (mm)**	**Accuracy Over Depth (%)**	**True Depth (mm)**	**Determined Depth (mm)**	**Accuracy Over Depth (%)**
I	N/A	N/A	N/A	N/A	N/A	N/A
II	127	130	0.66	N/A	N/A	N/A
III	127	120	2.3	N/A	N/A	N/A
IV	N/A	N/A	N/A	N/A	N/A	N/A
V	127	130	0.66	N/A	N/A	N/A
VI	127	130	0.66	N/A	N/A	N/A
VII	127	130	0.66	60	51	2.4
VIII	127	130	0.66	80	76	1
IX	127	130	0.66	Not Identified	25	N/A
X	127	130	0.66	210	203	1.8
XI	127	120	1.8	210	203	1.8

Table 3.6: Summary of Specimen Thickness

Slab Number	True Thickness (mm)	Determined Thickness (mm)	Error (%)
I	305	300	1.7
II	457	460	0.66
III	305	300	1.7
IV	610	610	0
V	610	610	0
VI	381	380	0.26
VII	381	380	0.26
VIII	381	370	2.9
IX	381	380	0.26
X	381	380	0.26
XI	381	380	0.26

A comparison of results obtained from the vertical and horizontal scan orientations show some interesting trends. First, the vertical scan orientation more clearly detected the horizontal rebar while the horizontal scan orientation showed the vertical rebar. This observation was made consistently in all slabs that contained reinforcing steel. The simulated defects do not present the exact same image in each orientation, but enough information is provided for the user to come to the same conclusion about the defect location. Also, in every slab with a defect, a shadow of the defect, the blue color and the shape of the defect, can be seen at the bottom of the slab. Slab IX didn't contain a clear shadow, but it did have a slight outline of where the defect would be located. In addition, Slab IX was the only slab where the device was not able to clearly identify the defect. This is due to the lack of wave energy penetrating the full thickness of the slab. When comparing images obtained from overlapping scans with images obtained from scans without overlap, the former provided better clarity of

the defects; however, the defect could be seen with the latter case as well. For the latter case, familiarity with interpreting scan images may be required to determine the location of the defects.

Scanning the concrete slabs with overlap, as described above, takes an average of 2.5 hours per slab (6 ft by 6 ft). To scan a concrete slab without overlap takes 45 minutes. While the device can identify, localize, and size defects in concrete structures, it is labor intensive and costly. Additionally, this time does not include data processing, which could add several extra hours of work. To combat these issues, a zero-intrusive ultrasonic tomography device is necessary for the future to non-destructively test bridge decks.

4. PRELIMINARY DESIGNS

4.1 Design Process

Design is a methodical, iterative process and consists of several steps:

1. define the problem.
2. conduct research on the background of the problem and potential solutions.
3. brainstorm ideas to solve the problem.
4. develop preliminary solutions.
5. analyze the preliminary design solutions.
6. decide on a final prototype design.
7. test the prototype.
8. analyze results.
9. improve and adjust the prototype.
10. reiterate Steps 7 through 9 until a final design is determined.

The process allows for improvements and adjustments to be made throughout the design stage. The problem is clearly defined in the first and second chapters: concrete deteriorates at a rapid rate, especially below the surface, and current non-destructive evaluation techniques are time consuming, costly, cause traffic disturbances, and require a significant amount of training to be effective. To combat these issues, a zero-intrusive non-destructive bridge maintenance device is a necessity to maintain and improve infrastructure.

Several non-destructive testing methods were investigated and considered to be implemented into a high speed device, but ultrasonic tomography, which relies on ultrasonic pulse echo, is most suited for the task since it provides clear, unmistakable images of the interior condition of concrete structures. These refined images, due to the SAFT algorithm, make it possible for any user to identify a variety of flaws beneath the surface, including; delamination, water-voids, and air-voids. Through validation, discussed in Chapter 3, a handheld ultrasonic pulse echo device is able to characterize and localize all of these flaws. A key feature of this handheld device are the spring loaded, low-frequency transducers, which allow for proper contact on textured surfaces. The operational frequency of 50 kHz helps eliminate noise and interference when the signal is reflected by a defect or layer of rebar. Another desirable feature of the handheld device is its ability to record useful data in map mode in approximately two seconds per measurement with only one-sided access to the structure. The wear-resistant piezoceramic tips of the transducer array are dry-point-contact; therefore eliminating the need for contact gels and expediting the scanning process. For these reasons, the transducers used in this device are desired for the automation of ultrasonic tomography.

This chapter focuses on Steps 4 and 5 of the design process. Five preliminary mechanical designs are going to be discussed and analyzed as potential solutions. The ultimate goal is to create a lightweight, maneuverable, and portable device that can quickly and effectively identify and localize flaws within a concrete bridge deck. It is desired to integrate the spring-loaded, dry-contact transducers into the device due to their advantages. This also allows for design simplicity, since existing technology will be re-purposed into a faster, more effective form.

4.2 Automated Stepping Design: Option 1

The current transducer array requires the user to apply pressure in order to ensure proper contact with the surface for a successful measurement. The user applies the pressure and presses “Enter” on the handheld computer to send the signal. Moments later, the reflected wave is received and recorded in map mode. Recording in map mode allows the user to later apply the SAFT algorithm to a set of measurements, which is responsible for producing a high resolution image. This ability to collect a database of scans and apply the SAFT algorithm is the basis of ultrasonic tomography. This first design is based on the manual process. Initially, an automated stepping design is considered with two commercially available 4 by 6 transducer arrays mounted to two separate legs. The legs are hydraulically connected to a frame, which has several purposes. The frame provides weight to counteract the hydraulic force used to press the transducer array into the surface while providing stability. Pressing the array lightly into the surface ensures proper contact for a successful measurement.

The device moves comparable to human legs. The transducers start off next to one another, transducer array 2 then moves forward the desired step size. Pressure is applied with the hydraulic system in the legs to ensure the transducer array is in proper contact with the specimen surface, capturing a single measurement in map mode. Then transducer array 1 moves up next to the first transducer array, it is then pressed down by the hydraulic system and a measurement is taken. The stepping process is described in detail in Figure 4.1. The red arrow indicates the direction of movement.

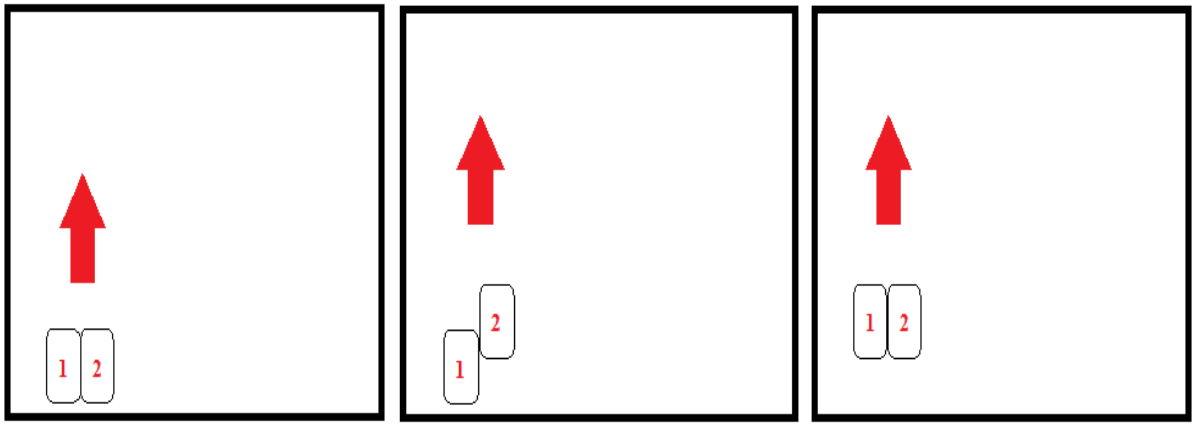

(a) Starting Position, Transducers are Aligned

(b) Transducer 2 Moves Forward and Takes Measurement

(c) Transducer 1 Moves to Align with Transducer 2

Figure 4.1: Detailed Movement of the Device

Figure 4.1 shows a general "step" with some overlap between measurements. This allows the SAFT algorithm to produce higher resolution images, which is a strength of this design. Additionally, due to the design, the step sized is customizable in order to accommodate varying scanning needs. Figure 4.1 shows the device scanning in the vertical direction, but it can also be rotated 90 degrees to scan in the horizontal direction, creating overlap in both directions to produce quality images. Due to movement being parallel to the surface of the specimen, it is easy for the data to be transmitted to a stationary computer for immediate analysis. Though these aspects are desirable, there are drawbacks to the design. The legs connecting the frame to the transducers would need to be motorized in order to move continuously, adding cost and weight. Also, due to the stepping design, it would need a "running" motion to operate at anything more than a few miles per hour and would not be able to reach highway speeds of 50 to 70 miles per hour. For this reason, this preliminary design will not be implemented.

A second, more refined version of the stepping design is presented in Figures 4.2 and 4.3. This system constitutes a smaller frame with two transducers on sliding rails. This allows for measurements to be taken in a similar manner as the first stepping design, but also provides more freedoms.

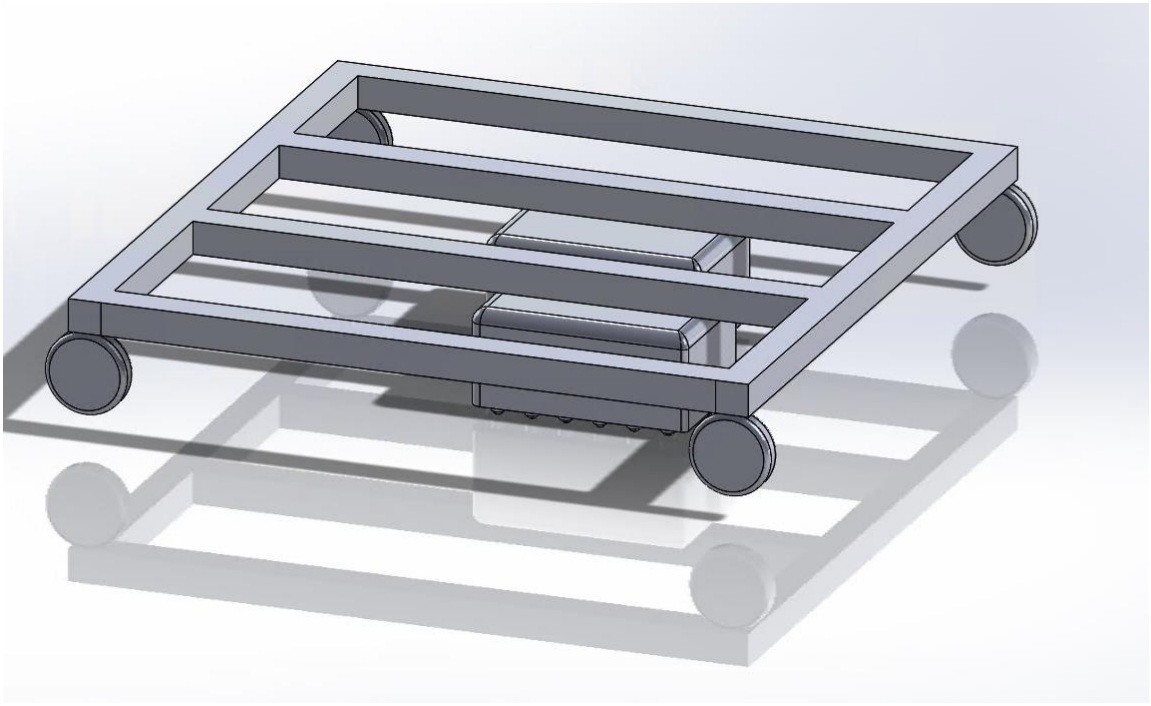

Figure 4.2: Sliding Rail System

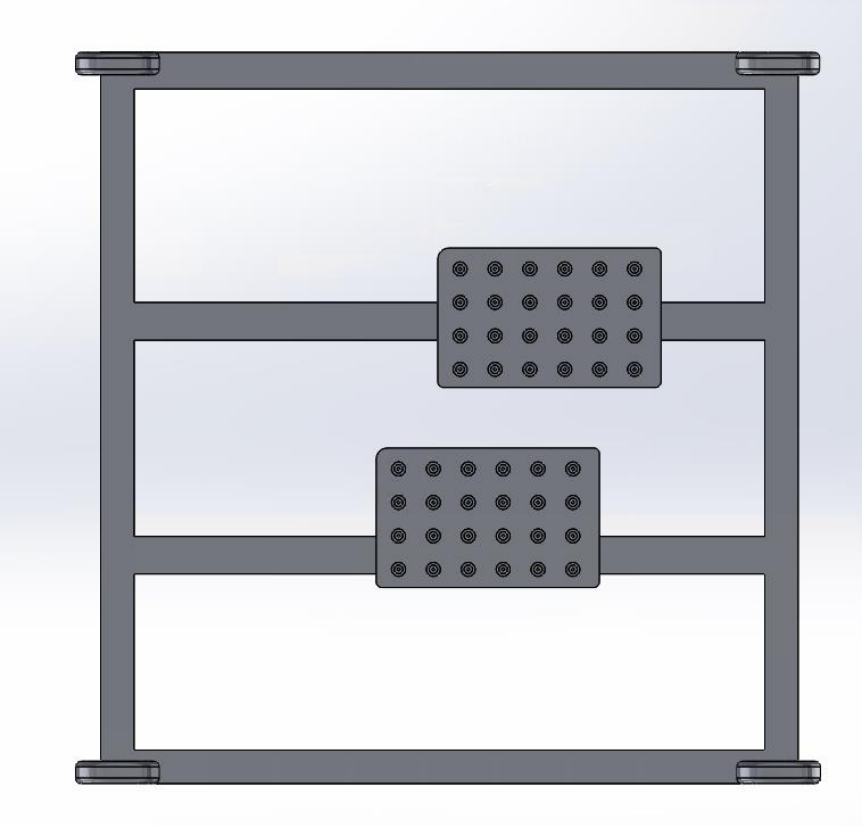

Figure 4.3: Sliding Rail System Bottom View

The frame provides mobility and stability for the transducer arrays. The arrays are mounted to a rail system, where the rails can be moved within the frame to move the transducer arrays closer together or further apart than the configuration in Figure 4.3. This system can move in stepping motions, like the leg-based system, where one transducer moves forward with the other following. Additionally, both transducers can move together, if desired, scanning a larger area in one measurement. Like the stepping design, this design allows for overlapping measurements to produce high resolution images and can easily transmit data from the system to a computer for immediate analysis. The transducer array will still need a hydraulic connection to the rails in order to place the tips in proper contact with the specimen. For the movement of the system, there are several options. The device can have the transducer arrays set in a permanent position and pulled behind a truck. However, the truck would need

to move the desired step size and allow the hydraulics to press the transducers into the ground for a measurement. Though automatic, this is time consuming. In contrast, the entire system can also be motorized where the transducers move together or each transducer can be motorized independent and moved by “stepping”. This provides a variety options for the user.

In each case, motorizing the system creates complications. The mechanical system increases the complexity of the solution and will need additional space and financial support to be implemented. Additionally, the variations of movement, while adding options, will need multiple motorized systems and more complicated programming in order to operate properly. If these issues can be addressed, the hydraulic system has speed limitations, limiting the overall system. For these reasons this design, while capable of operating automatically and having customizable options, it is unable to operate at highway speeds.

4.3 Continuous Track System: Option 2

As brainstorming progresses, a continuous track system, resembling the track of a tank, is considered. The continuous track has transducers equally spaced around the rubber perimeter. Figure 4.4 provides an image of a general configuration. A final design would require more details regarding the motorized system.

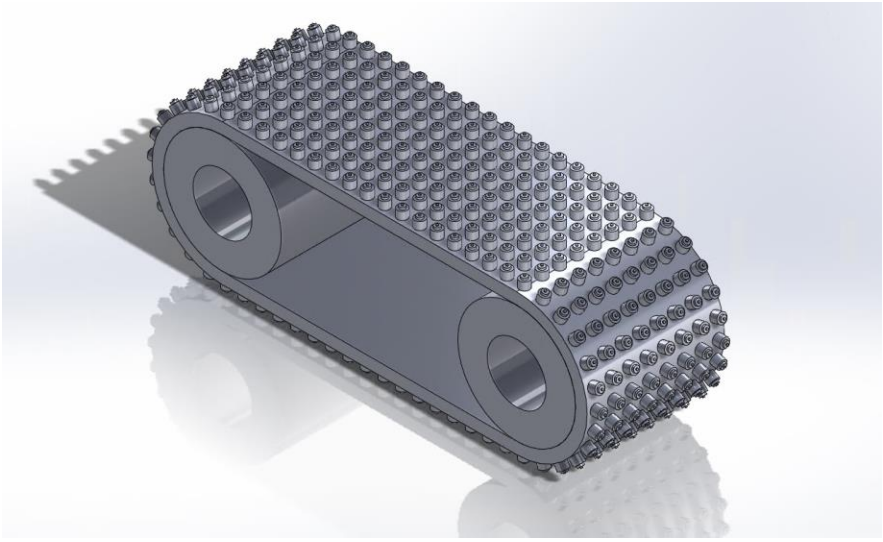

Figure 4.4: Preliminary Continuous Track Design

Figure 4.4 displays the transducer configuration for the continuous track system. In order to accomplish the transducer arrangement, multiple transducer arrays would need to be merged. This would increase the complexity of the wiring since the transducers would needs to be rearranged from their current wiring configuration. It also induces the challenge of transmitting a signal from a device that both rotates and translates to a stationary computer for immediate analysis.

The device can move with a motorized system or pulled manually with a truck. The self-weight provides enough force for the tips to make proper contact with the ground or specimen. It is essential that a more refined design would include more wheels than Figure 4.4 for evenly applied pressure and proper movement. A consequence of the design is that the transducers will be under a compressive force for an extended period of time due to the length of the continuous track. This makes the transducers more prone to wear, reducing their life span and ultimately becoming costly.

With the current transducer array, half the transducers are used for transmitting and half are used for receiving. Therefore, programming would need to be implemented to

determine which transducers are in contact with the ground for a signal to be sent and received for meaningful data collection. This makes the design more complicated. However, if this can be overcome, it would allow for the device to take measurements at various step sizes, providing overlap and therefore clarity.

The continuous track provides a larger surface area, therefore when taking measurements without overlap, a large area can be covered with a single measurement. Though it can cover a large surface area, historically, continuous tracks are unable to operate at high speeds due to their mechanical complexity. The mechanical system also shortens the operating life span, causing frequent repair. The track can potentially fall off the guiding wheels, making the device unreliable. A continuous track design has strengths, but also drawbacks that are too great for the intended application. After this point, rolling configurations are considered.

4.4 Rolling Design with Existing Transducer Arrays: Option 3

The continuous track design placed pressure on the transducers for a longer period of time than what is needed to acquire data. Due to this exposure and mechanical complexity the focus shifts to circular rolling designs. The initial rolling design relies on currently available transducer arrays for simplicity. Figure 4.5 presents the rolling design that incorporates existing transducer arrays.

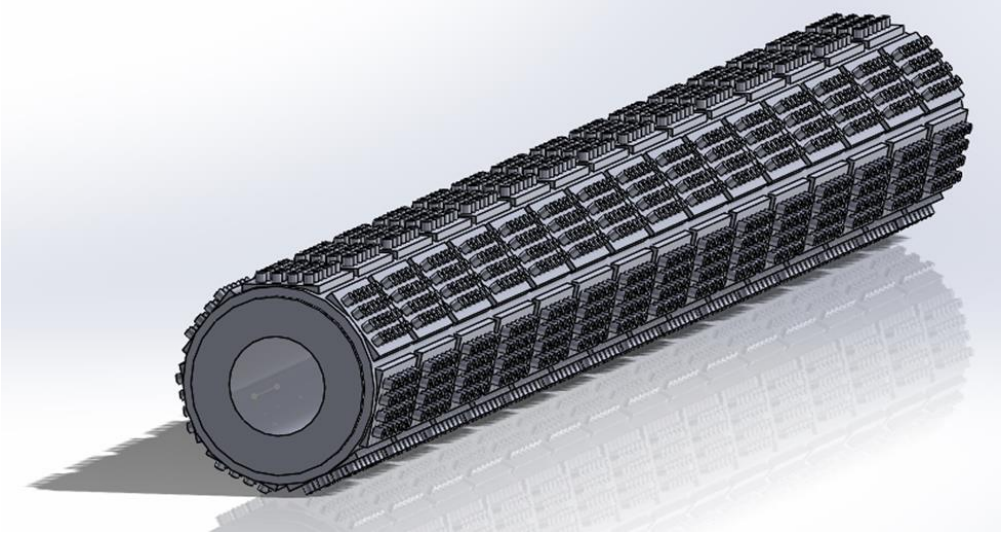

Figure 4.5: Rolling Design with Existing Transducer Arrays

The design provides simplicity since the transducer arrays have been proven to be functional and reliable. It would be easier to integrate correctly configured transducer arrays for a larger array. Measurements would be taken when a row of commercially available transducers were in contact with the ground. Again, self-weight would provide enough force to ensure the piezoceramic tips are in proper contact with the surface. Due to the circular design, they will not be under prolonged pressure, reducing wear.

However, this design is not without difficulties. The transducer arrays would need to be properly mounted so dynamic motion would not cause them to become loose. Additionally, correct spacing would be difficult to determine with the current commercially available transducers arrays since an entire row arrays would need to be in contact before taking a measurement. It is critical for spacing to be optimal so the edges can handle the impact when rotating. When going from prototype to full size, the device would need to be scaled properly in order to meet spacing requirements, this limits customization. Using currently available transducer arrays also incorporates unnecessary weight due to existing casings. Determining a way to transmit data from a rotating device to a stationary computer for processing remains a

challenge. Even with these limitations, a rolling design is ideal to be pulled behind a truck, eliminating the need for a motorized design.

4.5 Rolling Design with Existing Arrays and Individual Transducers: Option 4

A viable option, expanding on design Option 3, is to incorporate individual transducers in between the existing transducer arrays. The force applied to the edge of each array is a concern because the edges will be impacted directly as the device rolls. The current outer casing is composed of mostly plastic, which will results in damage after very little use at highway speeds. Individual transducers can be placed in between the existing arrays shown in Figure 4.5 to prevent damage and allow the device to roll more smoothly.

The primary issue with this design is how to program the transducers to send and receive the signals. In the previous rolling design, Option 3, when a row transducer arrays were in contact with the ground a signal would be emitted and received, but adding additional transducers in between the preconstructed arrays complicates this process. Advanced programming and reconfiguration of the wiring would need to be done in order for the device to work properly.

4.6 Rolling Design with Equally Spaced Transducers: Option 5

To combat spacing issues and impact in Options 3 and 4, the transducers will be taken out of their current casing and curved along a circular path. The current plastic outer shell can be removed, leaving a rubber securement that spaces the transducers. The rubber securement can be seen in between the transducers in Figure 4.6.

Figure 4.6: Rubber Securement In-between Transducers

The existing rubber between the transducers is flexible, meaning the transducers can be curved along a circular path while still maintaining current functionality and dependability. The challenge would be to determine how many 4 by 6 transducer arrays are needed in order to provide enough space for the portion of the transducer extending towards the center of the circle. Figure 4.7 shows the preliminary design option.

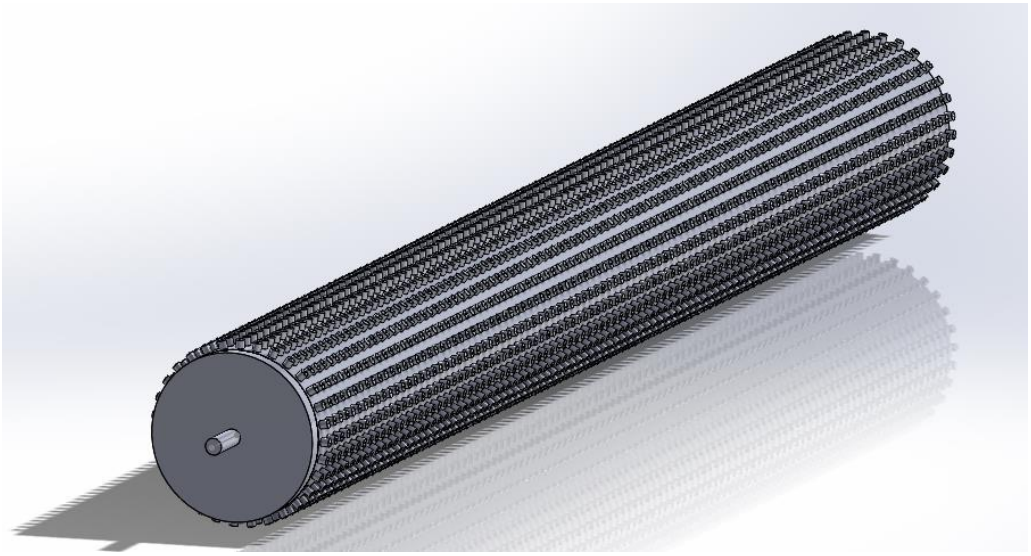

Figure 4.7: Rolling Design with Equally Spaced Transducers

The ability to remove the outer plastic casing saves weight and also allows for more freedom regarding overall device size. The wiring of the prototype will be simple since it will only be the width of a single transducer array. Signal timing issues can also be eliminated with

this design by programming the device to emit a signal when a row of transducers make contact with the ground. After verification of the finalized prototype design, it can be scaled to a larger size, similar to Figure 4.7. To reach this size, the transducers would need to be rewired so that one half of the device emits the signal while the remaining half receives it, similar to the current handheld ultrasonic device operation mode described in Chapter 2. While this would take effort, it is not as complicated as design Option 4. Additionally, a rolling design with equally spaced transducers would allow for a signal to be emitted when the transducers make proper contact with the ground, eliminating timing issues. All rolling designs have the capabilities to move at high speeds.

4.7 Comparison and Conclusion of Design Options

Each design option has their capabilities and limitations, but only a single option can be considered for a final prototype design. Table 4.1 summarizes the strengths and weaknesses of each design option.

Table 4.1: Summary of Design Options

Design Option	Strengths	Weaknesses
1	• Customizable step sizes for high resolution images	• Unable to operate at high speeds • Motorization increases complexity
2	• Capable of continuous measurements • Able to take overlapping measurements for high resolution images	• Continuous tracks are mechanically complex • Challenge to transmit signal • Unable to move at high speeds
3	• Reliable core processes have already been validated • Self-weight provides proper contact • Able to operate at high speeds	• Damage prone due to impact • Challenge to transmit signal • Spacing and data collection challenges • Lack of custom ability • Need optimization of SAFT for quick data analysis
4	• Reduces damage on edge of existing transducer arrays in Option 3 • Can potentially operate at high speeds	• Difficult to program signals for proper timing and data collection • Potentially jerking motion when rolling due to design • Bulkiest option • Need optimization of SAFT for quick data analysis
5	• Easily curved in a circle using verified existing array • Wiring already configured and reliable for prototype • Minimal damage from impact • Can potentially operate at high speeds • Signal timing issues eliminated	• Transmitting data from a rolling device to a stationary computer for immediate processing • Need optimization of SAFT for quick data analysis

From analyzing the potential designs presented, design Option 5 presents significant strengths with relatively few challenges. The challenges listed can be overcome with a more refined design. The rotating wheel of transducers will need to be connected to a non-rotating frame that supported by the truck pulling the device. Wiring can run from the device, through the frame, to a laptop inside the cab for immediate image analysis. Potential solutions for transmitting data from a rotating device include; slip rings, rotary transformers, or commutators coupled with carbon brushes. These are all viable options depending on the detailed interior of the prototype design. Currently, the SAFT algorithm coupled with EYECON is too slow to collect data at highway speeds. This will need refinement in order to develop the final product. Ultimately, design Option 5, a rolling design with equally spaced transducers provides a stable base for furthering the design.

5. REQUIREMENTS FOR HIGH SPEED APPLICATION

5.1 Introduction

In the previous chapter, numerous preliminary designs were analyzed. Ultimately, a rolling design with equally spaced transducers is ideal to construct a prototype and final product. Creating a prototype is an essential part of the design process and allows for validation and optimization prior to construction of a larger, more costly device. The prototype needs to be scaled smaller than the design presented in Chapter 4 in order for researchers to perform testing, modifications, re-testing, and demonstrations. First iterations will move at slower speeds in order to verify the capabilities of ultrasonic tomography and will be closer to the manual speed of data collection. Following this phase, the prototype will need to be scaled the width of a road lane, which will require significantly more material and time to construct. However, upon completion, it can gather data regarding a bridge deck in a matter of minutes. In order for this to be possible, several aspects need to be considered prior to building a prototype. These topics include; durability, signal processing, and full scale adjustments.

5.2 Durability

A primary concern is the durability of the system. As it moves at highway speeds, it will be prone to impact and dynamics forces which will eventually damage the device. The piezoceramic tips are primarily in compression as the device rolls, but the ceramic materials have a high stiffness values in compression, which make them durable for this purpose (PI Ceramics, 2008). Slip and shear forces factor in when the device is rolling and therefore shear and compressive strength of the transducers needs to be determined according to ASTM testing

standards with an MTS testing machine. These values should be determined prior to prototype manufacturing in order to determine limitations and prevent transducer failure.

Since the device will be subjected to vibrations while traveling, the device needs to be constructed in a manner that allows for easy assembly and disassembly. This allows for interior changes, maintenance, and adjustments. For this reason, welding, tight fitting, and other permanent connections should be avoided unless absolutely necessary. By implementing a bolted design, the users can make necessary changes during the prototype phase while allowing for easy maintenance of the final product.

5.3 Signal Processing

Signal processing is a key component of success for this project. Eventually, the final product will be able to produce real-time images representing the interior condition of concrete bridge deck. Manually, each measurement takes up to three seconds to record with the current handheld EYECON device. This limitation is primarily due to processing times on the handheld computer that comes with EYECON, not the ability to emit and receive ultrasonic waves, which only takes a fraction of a second. Therefore, rapid data collection is possible but a different, highly efficient processing system must be developed in order to meet speed requirements. Initially, this processing system may not have a user friendly interface in order to minimize processing times, but an interface could be integrated at a later phase.

Another primary concern is how the transducers will trigger a signal. Currently, an ultrasonic wave is generated by pressing “Enter” on the handheld computer while the transducers are in contact with the specimen. The transducer array uses half the transducers to emit and the remaining half to receive, which depending on the design, could cause timing issues. Two separate wheels could be used, where one wheel of transducers emits the ultrasonic waves while the other receives them, but this would complicate timing. Instead, all transducers should be on one wheel, configured where the left hand side emits the signal and the right have side receives the signal or vice-versa, similar to the existing transducer array. The signal should be triggered when the transducer row makes contact with the ground, essentially activating the row of transducers. Data then will only be gathered from the transducers in contact with the specimen, making it reliable and able to operate at varying speeds without altering the settings of the device. Limiting speeds will need to be determined throughout the prototype phase of the zero-intrusive high speed ultrasonic device.

Bridges and roadways are known to contain potholes, cracks, rough textures, and a variety of other small obstacles. There is an extremely small probability that a transducer or row could get stuck in a crack or hole. Surfaces with varying textures were testing as part of the experimental program in Chapter 3 and did not influence results since only a small number of the transducers were affected. This occurred primarily when measurements were taken over an area where formwork was present, which was comprised of a hollow steel rod that was used during the construction process. In Figure 5.1, four hollow steel rods can be seen on the surface of Slab II in addition to a surface crack. At times, a few tips of the transducers would be placed within the hollow rods while taking a measurement due to the step size, but this did not alter the data.

Figure 5.1: Hollow Rods Shown in the Four Corners of Slab II

Additionally, different ultrasonic transducers have previously been verified on a variety of surface textures through additional testing of shotcrete specimens and in-service bridges (Wimsatt et al., 2013). Therefore, if a minimal number of spring loaded transducers are unable to make contact with the specimen due to a hole or crack, useful data can still be collected.

Programming will be an extensive component in the continuation of this design due to the high speed application. It will need to account for trigging signal, transferring data, and processing data into useful images for the inspection of concrete bridge decks and potentially other surfaces.

5.4 Full Scale Adjustments

The system needs to be able to relate data to specific locations. A global positioning system (GPS) could be used to record locations while data is being collected, but would be difficult to relate visually. Digital mapping is a useful solution because it combines a topographical virtual map, similar to Google Maps, with processed data regarding the interior

condition of the concrete bridge deck. This technology can overlay the C-scans of the most critical defects located within a bridge deck on a virtual map, allowing for engineers to quickly determine bridge decks in need of maintenance. It can provide an overall image of the deck's condition, but engineers will still need to reference detailed data regarding the depth, size, and type of defect in order to correctly prioritize the bridges. Overall, integration of this technology into the final product, after the verification of the prototype, would be extremely beneficial for establishing a database.

5.5 Summary

Once a final prototype design is developed, the transducers need to be tested to determine maximum allowable compressive and shear stresses. It is important to thoroughly investigate these limitations because excessive forces applied to the prototype and final design could have severe consequences. Manufacturing of the prototype will be straightforward and must be constructed in a way to allow for changes and repairs. The most difficult aspect of the design will be to expedite the processing of the data and application of the SAFT algorithm. It is essential to create real-time images of defects below the surface. Testing and prototype development can be performed concurrently with development of the processing system since data can be post processed to confirm results.

6. CONCLUSIONS AND FUTURE WORK

6.1 Conclusions

This research validates handheld ultrasonic tomography, presents preliminary design options, and discusses requirements for a final product. The handheld ultrasonic tomography device was able to clearly recognize a variety of artificial defects at different depths; including, rebar, a thin piece of plastic representing delamination, water-voids, and air-voids. The initial presence of the defects was successfully determined in all but one concrete slab. The defect in this slab, Slab IX, was located about a 25 mm (1.0 in.) beneath the surface, the shallowest of any defect, indicating there may be near-sighted limitations with the handheld system. Transducer orientation makes a significant impact on the processed images, but provides similar information for the user. With the transducer in the horizontal orientation, vertical defects are more apparent, while the vertical orientation reveals horizontal defects more clearly. Also, all specimens with thin plastic defects present a shadowing effect throughout the slab since the ultrasonic waves are unable to penetrate the plastic. In general, the ultrasonic tomography device successfully located a variety of defects and rebar layers, proving to be capable for fast pace integration.

Initial scans used overlapping measurements to produce a refined image using the SAFT algorithm, but scans without overlap also conveyed evidence of defects, demonstrating that overlapping scans provide clarity but are not absolutely necessary in localizing and characterizing the defects. From the experimental program, it can be concluded that ultrasonic tomography is a feasible non-destructive testing method that is capable of detecting flaws in

concrete decks. However, in the current stage, scanning concrete surfaces is time-consuming and costly. Therefore, a high speed ultrasonic tomography device will be developed to optimize bridge inspection in the future.

Five preliminary design options are considered for prototype development. The first design option, a stepping device, allows for overlapping measurements for high resolution images but its configuration would not be able to operate at high speeds. Design Option 2, a continuous track, is capable of continuous measurements and could be programmed to trigger signals for overlapping measurements. However, continuous tracks are mechanically complicated and are not known for high speed application. A third design option capitalizes on the existing transducer array configuration in a rolling scheme. It is more reliable since the core processes have been verified, but issues with spacing and impact could limit the speed and durability. Preliminary design Option 4 expands on the third option by adding individual transducers in between existing arrays. This would reduce potential damage and provide a smoother rolling operation, but it would be difficult to configure all the transducers so they emit and receive signals at the proper time. The fifth design option takes the rubber securement and transducers out of the existing case and forms them into a cylindrical shape for rolling. This provides reliability, equal spacing for minimal damage, and signal timing issues are eliminated. Signal processing will need to be expedited for high speed application.

The design of the zero-intrusive ultrasonic tomography system should contain several key features. A variety of aspects were considered regarding durability, signal processing, and full scale adjustments. First, the transducers do not require any coupling agent, which decreases operating costs and time. Additionally, the transducers are spring loaded with a piezoceramic tip, therefore allowing for proper contact with the test surface irrespective of the

texture of the surface, which increases durability. The prototype needs to be lightweight, making it maneuverable and portable. Lastly, the design should permit future iterations and improvements by allowing for quick and easy assembly and disassembly of the components. Signal processing will be the main challenge when implementing the device at highway speeds. Additionally, digital mapping will be integrated to generate a visual database of concrete bridge deck conditions at a later phase.

This research conducted initial investigations into handheld ultrasonic tomography and designs, but additional research will need to be conducted to develop a final prototype design. Following the prototype design, assembly, validation, improvements, and re-testing will reveal additional changes needed for full speed implementation.

6.2 Future Work

The next phase of this research is comprised of several tasks. First, a detailed prototype design must be developed incorporating the features discussed in this thesis. Computer aided design (CAD) drawings need to be produced detailing the outer arrangement of the transducers and specifying the internal configuration. Several iterations of design will need to be conducted prior to manufacturing and construction of the prototype. Next, necessary components to manufacture and assemble the prototype need to be acquired, including additional transducer arrays. The handheld ultrasonic system successfully detected a variety of defects at an operational frequency of 50 kHz, but it should also be tested at frequencies ranging from 30 kHz to 80 kHz to determine the optimal operating frequency. This should be determined prior to assembly.

After initial assembly of the prototype, a real-time data collection system needs to be developed so engineers can swiftly accumulate and analyze data regarding the condition below the surface. Currently, data is acquired and partially processed during scanning and then post processed to produce images. By increasing computation speed and streamlining the process, the system will be able produce real-time images for immediate use. This will then need to be integrated with the assembled prototype for testing and validation. The completed prototype will then be used to test the same slabs used in Chapter 3, along with a concrete bridge girder located at Texas A&M University RELLIS Campus in Bryan, Texas. This will allow the team to monitor accuracy, precision, and ease of use to make necessary changes to optimize the hardware and software.

Upon completing of testing, modifications will be made in order to improve the system and make it more precise, more accurate, and/or increase testing speed. After any modifications, the system will be retested. Additionally, the implementation of digital map imaging (DMI) into the device shall be evaluated. DMI could provide a physical location correspondence to defects that may be more useful than global positioning systems (GPS).

REFERENCES

Acoustic Control Systems, “Ultrasonic Tomograph for Imaging of Concrete Structures A1040 MIRA”. Acoustic Control Systems, Moscow, Russia. (2015).

ACI Committee. 318-14. “Building Code Requirements for Structural Concrete (ACI 318-14) and Commentary.” American Concrete Institute, Farmington Hills, Michigan, USA. (2014).

ASCE. 2013. “2013 Report Card for America's Infrastructure.” ASCE. (2013).

Bamler, R. “A Comparison of Range-Doppler and Wavenumber Domain SAR Focusing Algorithms Delay.” Geoscience and Remote Sensing, IEEE Transactions. 30, 706-713. (1992).

Barnes, C.L., and Trottier, J.F. “Ground Penetrating Radar for Network Level Concrete Deck Repair Management”. ASCE Journal of Transportation Engineering, 126(3), 257–262. (2000).

Bishko, A.V., Samokrutov, A., and Shevaldykin, V.G. “Ultrasonic Echo-Pulse Tomography of Concrete Using Shear Waves Low-Frequency Phased Antenna Arrays.” Proc. 17th World Conference on Non-destructive Testing, Shanghai, China. (2008).

Burr, E, Große, C., and Reinhardt, H.-W. “Application of a Modified SAFT-Algorithm on Synthetic B-scans of Coarse Grained Materials.” NDT.net, Vol. 3 No. 2. (1998).

Chase, S.B., and Laman, J.A. “Dynamics and Field Testing of Bridges.” Transportation in the New Millennium, Transportation Research Board. (2000).

Cheng, C.C, and Sansalone, M. “Determining the Minimum Crack Width That Can Be Detected Using the Impact-Echo Method.” Materials and Structure, 28(6), 74–82. (1995).

Dengzhi, W. “Non-linear Synthetic Aperture Focusing Technology Ultrasonic Imaging Applied in Non-destructive Testing” NDT.net. Vol. 12 No. 9. (2014).

Farny, J. A., and Kerkhoff, B. “Diagnosis and Control of Alkali-Aggregate Reactions in Concrete”. Portland Cement Association IS413, Washington, D.C., USA. (2007).

Germann Instruments. "EYECON - GERMANN." Germann RSS. Germann Instruments. (2015).

Gowers, K.R., and Millard, S.G. “Measurement of Concrete Resistivity for Assessment of Corrosion Severity of Steel Using Wenner Technique.” ACI Materials Journal, 96(5), 536-542. (1999).

Gucunski, N., Imani, A., Romero, F., Nazarian, S., Yuan, D., Wiggenhauser, H., Shokouhi, P., Taffe, A., and Kutrubes, D. “Non-destructive Testing to Identify Concrete Bridge Deck Deterioration.” Report No. S2-R06A-RR-1, Strategic Highway Research Program, Transportation Research Board, Washington, D.C. (2013).

Hall, T.E., Doctor, S.R. and Reig, L.D. “A Real-Time SAFT System Applied to the Ultrasonic Inspection of Nuclear Reactor Components.” Pacific Northwest Laboratory, Richland, WA. (1986).

Hillger, W., Buhling, L., and Ilse, D. "Review of 30 Years Ultrasonic Systems and Developments for the Future."11th European Conference on Non-Destructive Testing. Prague, Czech Republic. (2014).

Hoegh, K. E. “Ultrasonic Linear Array Evaluation of Concrete Pavements.” Thesis. The University of Minnesota Department of Civil, Environmental, and Geotechnical Engineering. (2013).

Im, S., Hurlebaus, S. and Trejo, D. “Inspection of Voids in External Tendons of Posttensioned Bridges.” Transportation Research Record: Journal of the Transportation Research Board, TRB, National Research Council, Washington, D.C., 2172, 115–122. (2010).

Johnson, G. "Ultrasonic Flaw Detectors...And Beyond." Quality Magazine RSS. BNP Media, 19. (2013).

Kotoky, N., and Shekhar, S. “Damage Identification Using SAFT Algorithm.” International Journal of Innovative Research in Science, Engineering and Technology, 3(4), 194-199. (2014).

Kurz, J., H. Rieder, M. Stoppel, and A. Taffe. "Control and Data Acquisition of Automate Multi-sensor Systems in Civil Engineering." Non-Destructive Testing in Civil Engineering: Ndt.net. (2009).

Nitske, W. R. “The Life of Wilhelm Conrad Röntgen: Discoverer of the X-Ray.” Tucson: U of Arizona. (1971).

PI Ceramics, "Forces and Stiffnesses." PI Piezo Technology. PI Ceramics. (2008).

Quillin, K. “IP 11/01 Delayed Ettringite Formation: in-situ concrete.” BRE Press. (2001).

Reichling, K., M. Raupach, H. Iggenhauser, M. Stoppel, G. Dobmann, and Kurz, J. "BETOSCAN – Robot Controlled Non-destructive Diagnosis of Reinforced Concrete Decks." NDTCE 2009, Non-destructive Testing in Civil Engineering. (2009).

“Report on Texas Bridges.” Bridge Division, Texas Department of Transportation. (2014).

"Revolutionary RABIT™ Bridge Deck Assessment Tool." Rutgers University. Center for Advanced Infrastructure and Transportation. (2014).

Ryden, N., M. J. S. Lowe, and Cawley, P. "Non-contact Surface Wave Testing of Pavements Using Microphones." The Journal of the Acoustical Society of America J. Acoust. Soc. Am. 124.4: 2576. (2008).

Shokouhi, P., Wöstmann, J., Schneider, G., Milmann, B., Taffe, A., and Wiggenhauser, H. “Non-destructive Detection of Delamination in Concrete Slabs.” Transportation Research Record: Journal of the Transportation Research Board, TRB, National Research Council, Washington, D.C., 2252, 103. (2011).

Stepinski, T. “An Implementation of Synthetic Aperture Focusing Technique in the Frequency Domain.” Ultrasonics, Ferroelectrical and Frequency Control, IEEE Transactions. 54, 1399-1408. (2007).

Stimolo, M. “Passive Infrared Thermography as Inspection and Observation Tool in Bridge and Road Construction.” Proc. International Symposium, Berlin, Germany, 1-6. (2003).

Tinkey, Y., L. D. Olson, R. Bedon, and Lieberle, C. "Impact-Echo Scanning Technology for Internal Grout Condition Evaluation in Post-Tensioned Bridge Ducts." Impact-Echo Scanning Technology for Internal Grout Condition Evaluation in Post-Tensioned Bridge Ducts. Non-destructive Testing in Civil Engineering. (2003).

White, J., S. Hurlebaus, S. Nazarian, and Shokouhi, P. "SHRP 2 R06G: Tunnel Non-destructive Testing Equipment User's Manual." Transportation Research Board of the National Academies, Washington, D.C. (2014).

White, J. B. "Ultrasonic Tomography for Detecting and Locating Defects in Concrete Structures". Thesis. Texas A&M University. College Station: Texas A&M U. (2012).

Wimsatt, A.; White, J.; Leung, C.; Scullion, T.; Hurlebaus, S.; Zollinger, D.; Grasley, Z.; Nazarian, S.; Azari, H.; Yuan, D.; Shokouhi, P. and Saarenketo., T.: "Mapping Voids, Debonding, Delaminations, Moisture, and Other Defects Behind or Within Tunnel Linings." SHRP 2 Final Report S2-R06 (G)-RW. Strategic Highway Research Program 2, Washington, D.C. (2013).

Wimsatt, A., Zollinger, D., Scullion, T., Lytton, R., Fernando, E., Walker, R., and Hurlebaus, S.: "A Plan for Developing High-Speed, Non-destructive Testing Procedures for Both Design Evaluation and Construction Inspection.", Final Report, Federal Highway Administration, SHRP2 Final Report, Strategic Highway Research Program 2, Washington, D.C. (2008).

Woo, J. "Early History of Metal Flaw Detectors." Early History of Metal Flaw Detectors. Resource Discovery Network, University of Oxford. (2002).

Zhu, J., and Popovics, J. "Imaging Concrete Structures Using Air-Coupled Impact-Echo." Journal of Engineering Mechanics, ASCE. (2007).

APPENDIX A: SLAB IMAGES

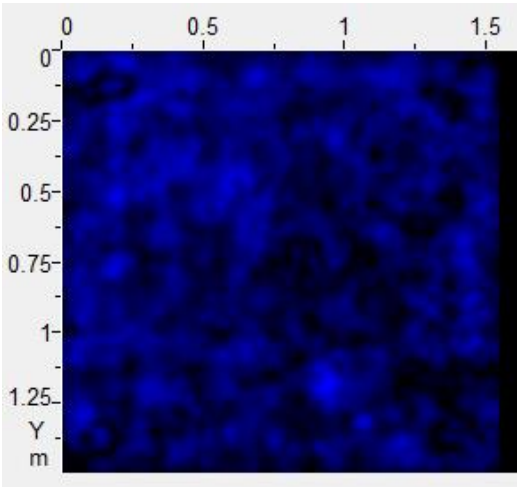

(a) Top of the Slab z =0 m

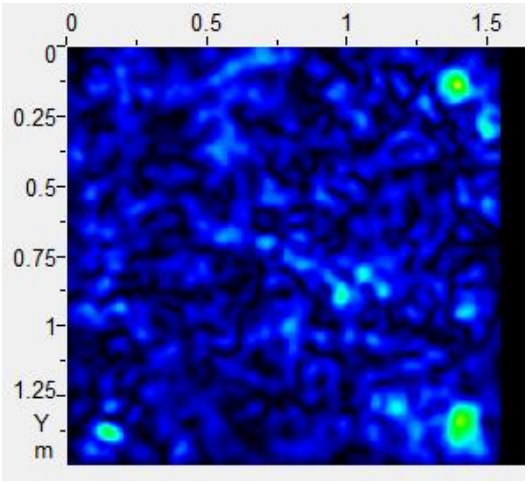

(b) Depth of 90 mm z =0.09 m

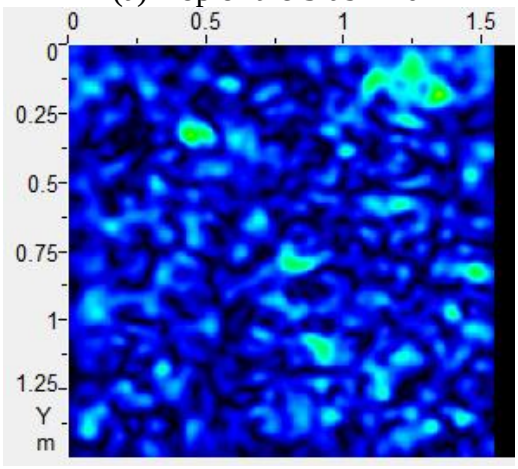

(c) Depth of 190 mm z =0.19 m

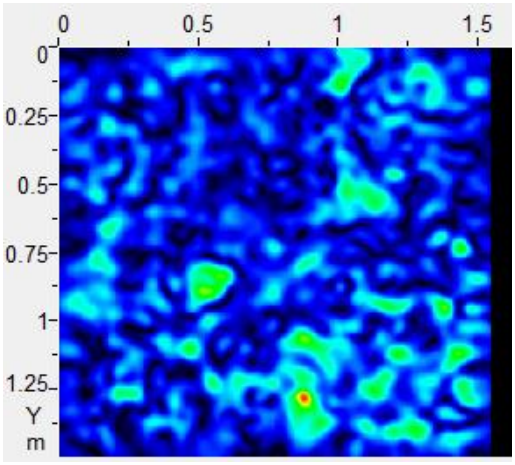

(d) Depth of 240 mm z =0.24 m

Figure A.1: C-Scans of Slab I at Various Depths using Vertical Transducer Orientation

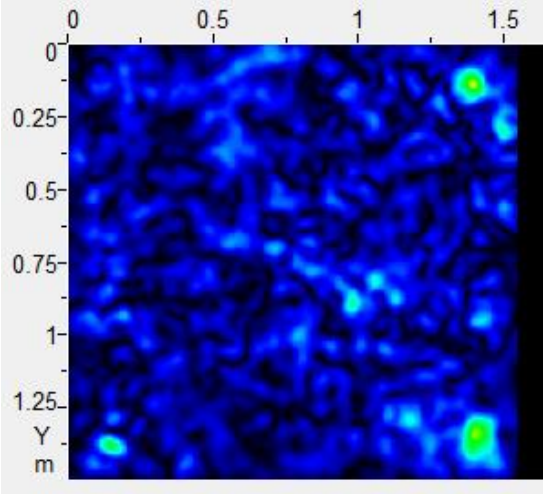

(a) Depth of 90 mm, Vertical Orientation

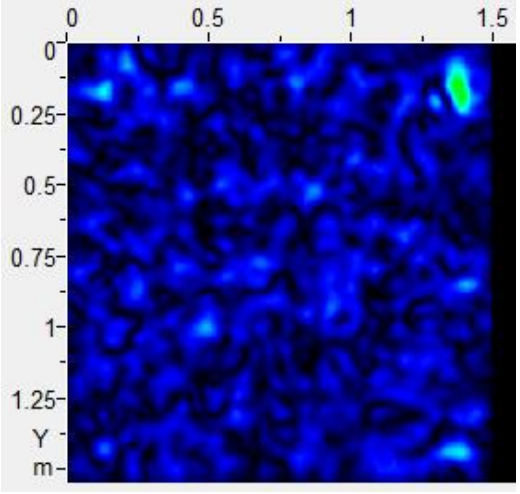

(b) Depth of 90 mm, Horizontal Orientation

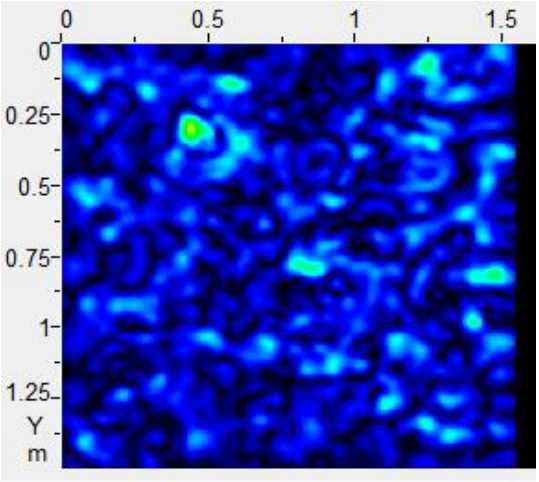

(c) Depth of 150 mm, Vertical Orientation

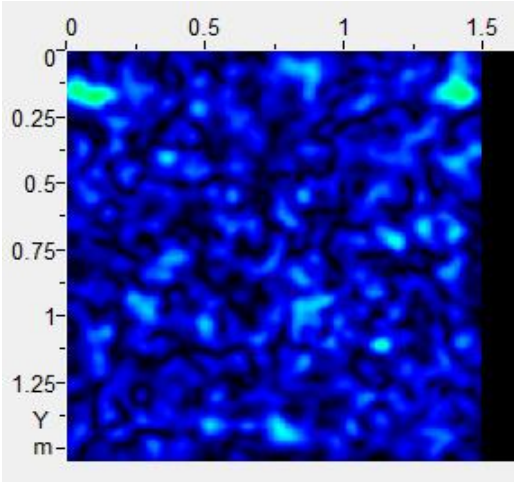

(d) Depth of 150 mm, Horizontal Orientation

Figure A.2: C-Scans of Slab I with the Vertical (left) and Horizontal (right) Orientations at 90 mm and 150 mm

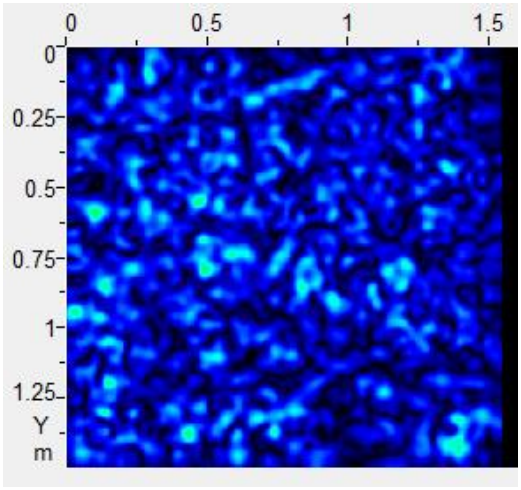

(a) Depth of 60 mm z =0.06 m

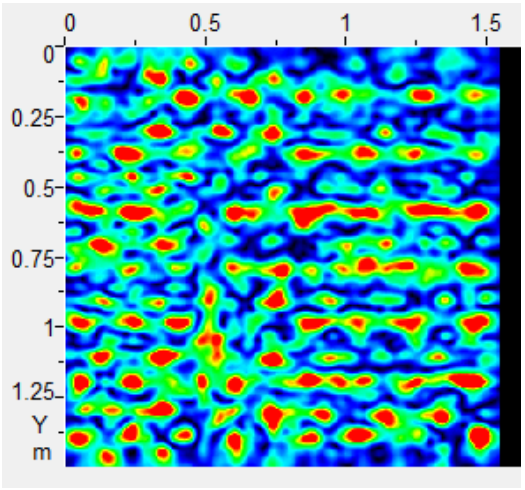

(b) Depth of 100 mm z =0.10 m

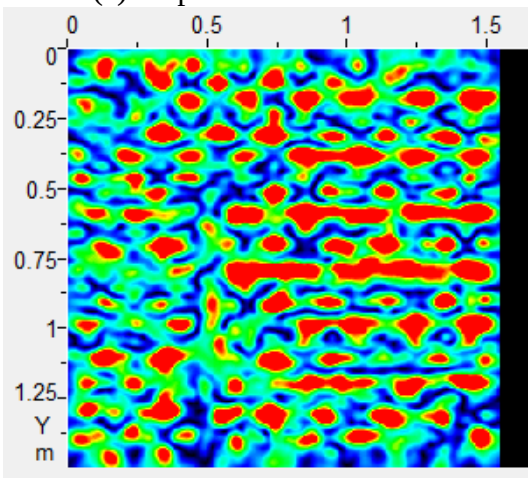

(c) Depth of 120 mm z =0.12 m

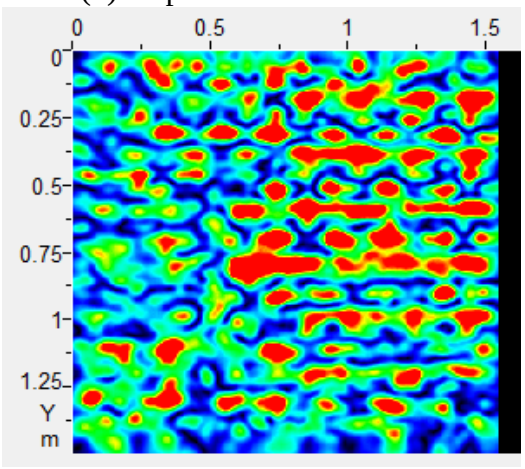

(d) Depth of 130 mm z =0.13 m

Figure A.3: C-Scans of Slab II at Various Depths from 60 mm to 130 mm

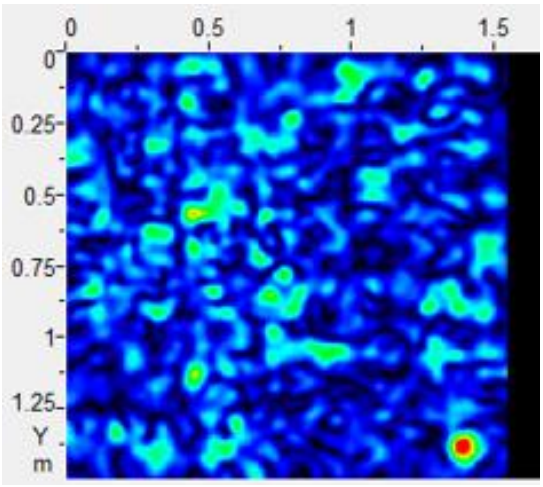

(a) Depth of 270 mm z =0.27 m

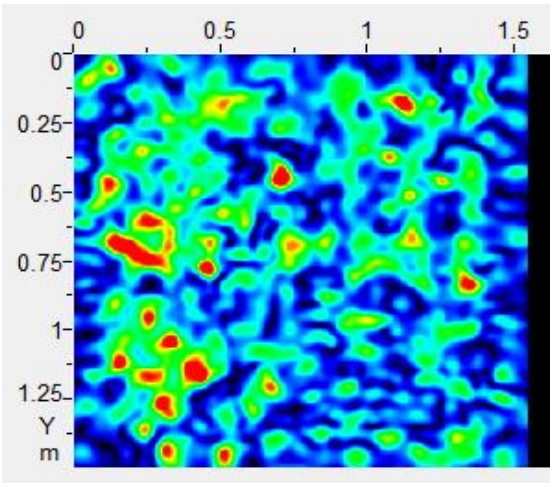

(b) Depth of 330 mm z =0.33 m

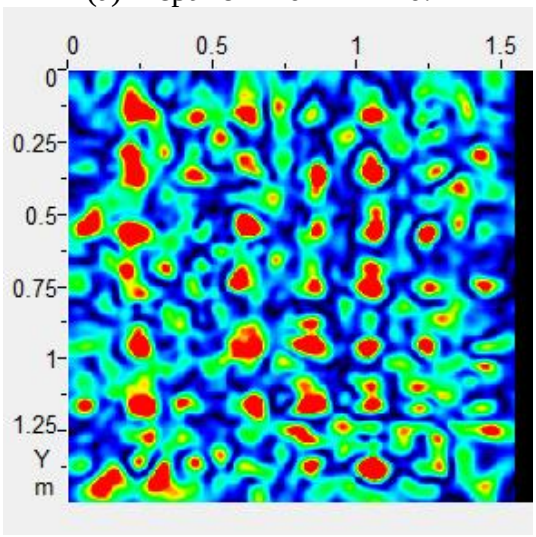

(c) Depth of 370 mm z =0.37 m

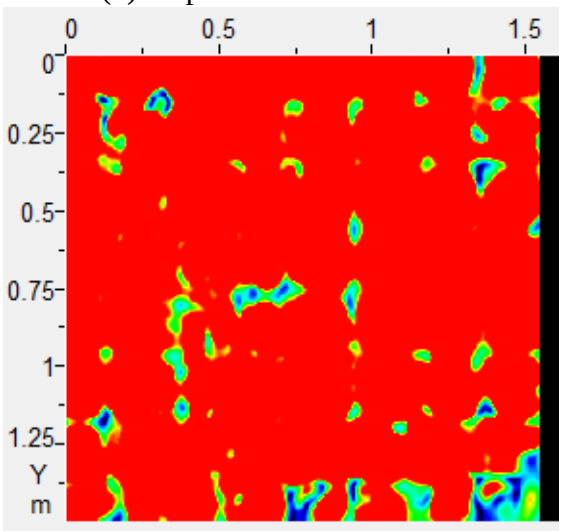

(d) Depth of 460 mm z =0.46 m

Figure A.4: C-Scans of Slab II at Various Depths from 270 mm to 460 mm

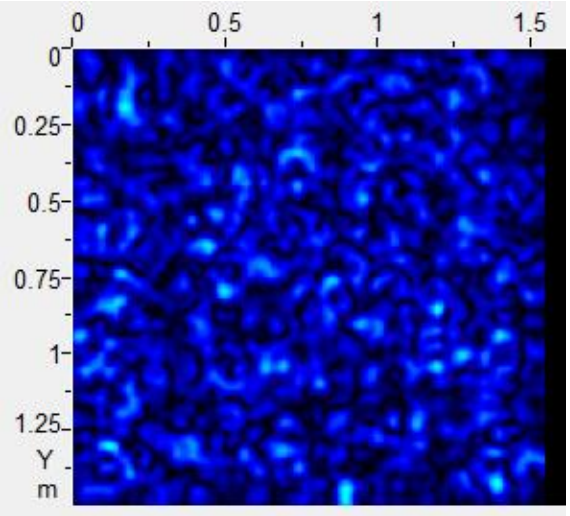

(a) Depth of 30 mm, Vertical Orientation

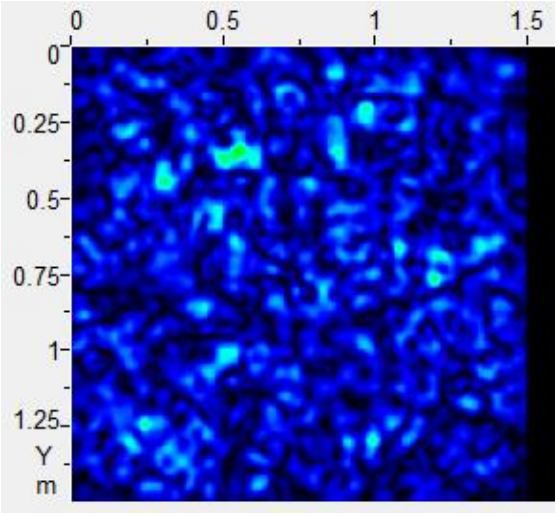

(b) Depth of 30 mm, Horizontal Orientation

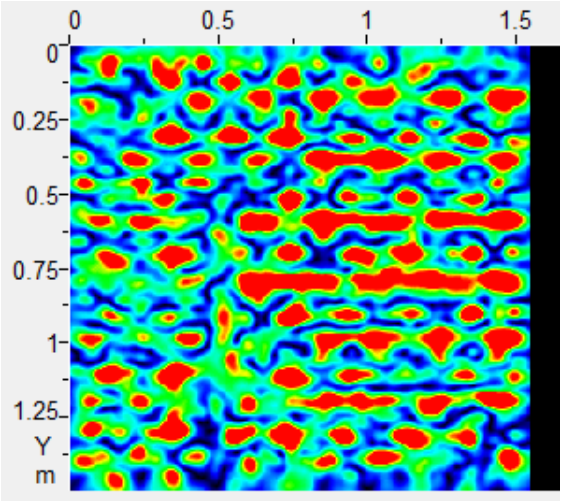

(c) Depth of 120 mm, Vertical Orientation

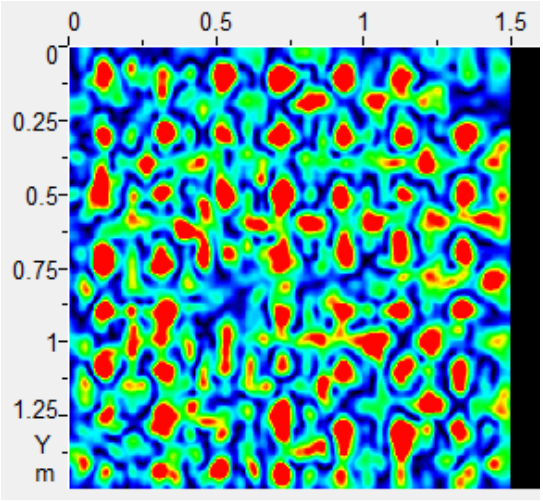

(d) Depth of 120 mm, Horizontal Orientation

Figure A.5: C-Scans of Slab II with the Vertical (left) and Horizontal (right) Orientations at 30 mm and 120 mm

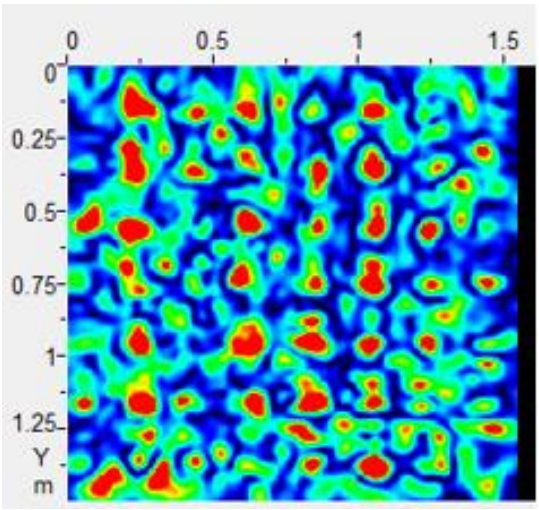

(a) Depth of 370 mm, Vertical Orientation

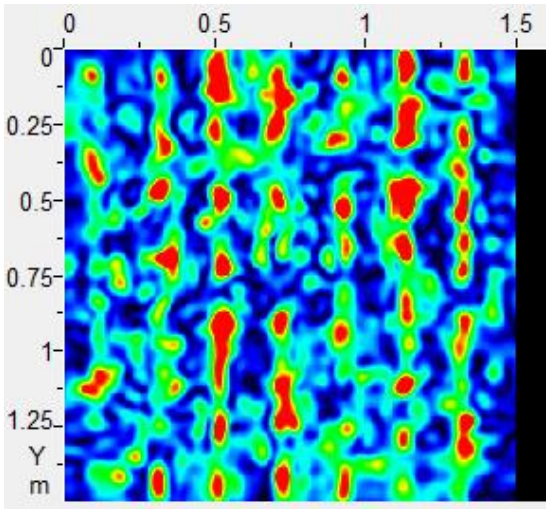

(b) Depth of 370 mm, Horizontal Orientation

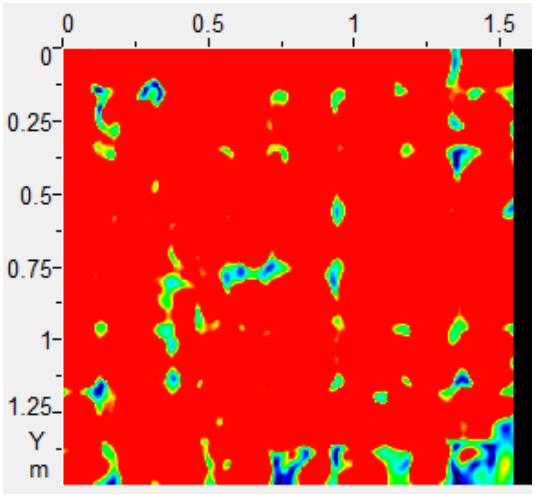

(c) Depth of 460 mm, Vertical Orientation

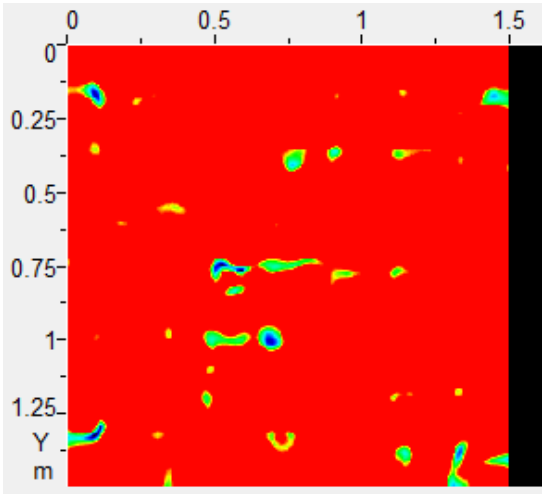

(d) Depth of 460 mm, Horizontal Orientation

Figure A.6: C-Scans of Slab II with the Vertical (left) and Horizontal (right) Orientations at 370 mm and 460 mm

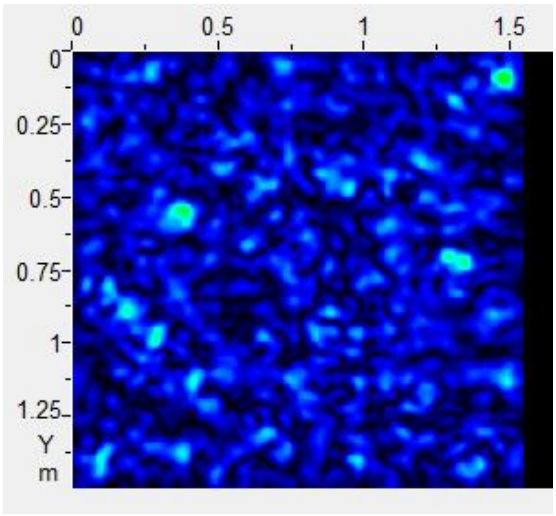

(a) Depth of 60 mm z =0.06 m

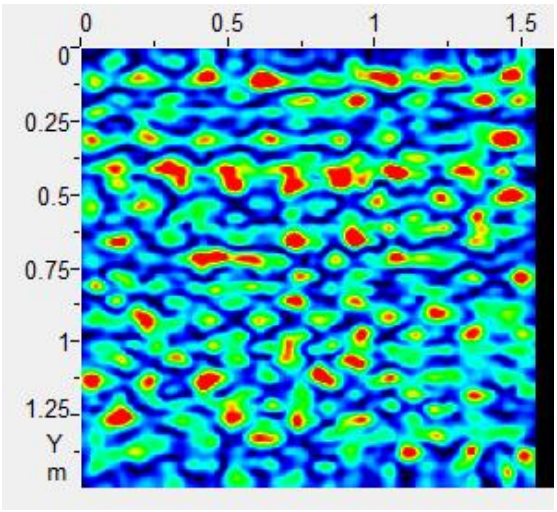

(b) Depth of 100 mm z =0.10 m

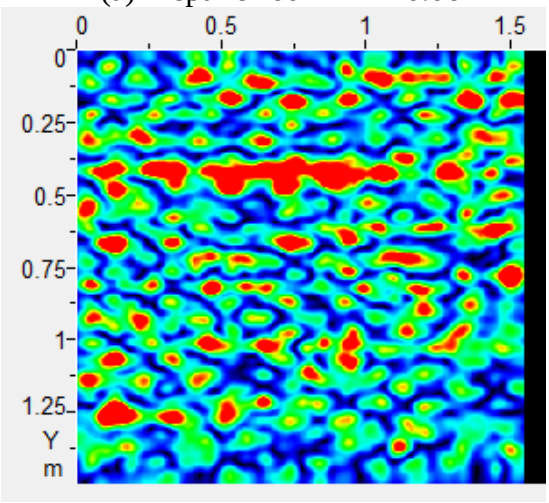

(c) Depth of 130 mm z =0.13 m

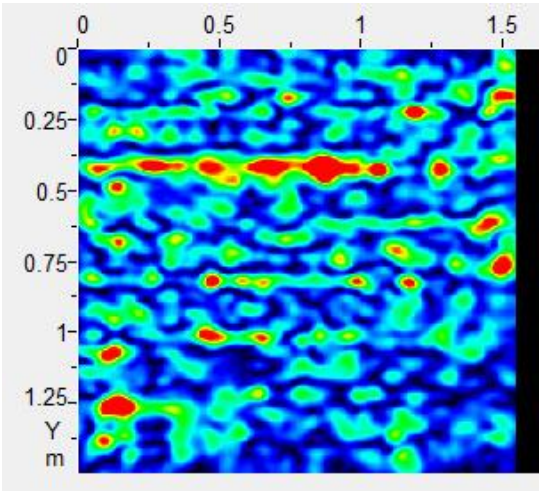

(d) Depth of 150 mm z =0.15 m

Figure A.7: C-Scans of Slab III at Various Depths from 60 mm to 150 mm

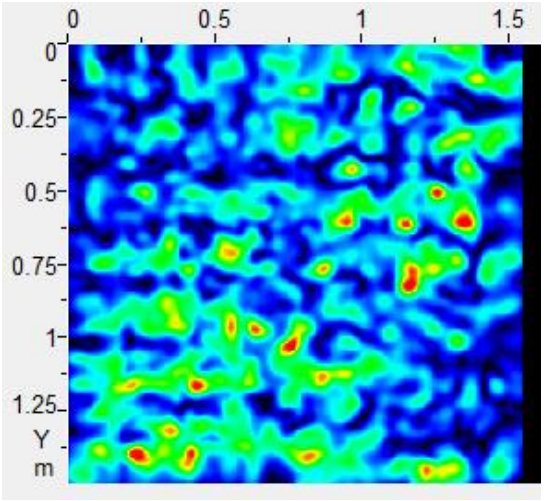

(a) Depth of 210 mm z =0.21 m

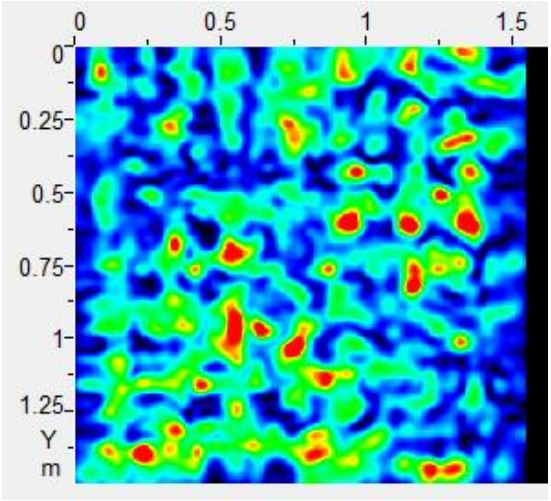

(b) Depth of 220 mm z =0.22 m

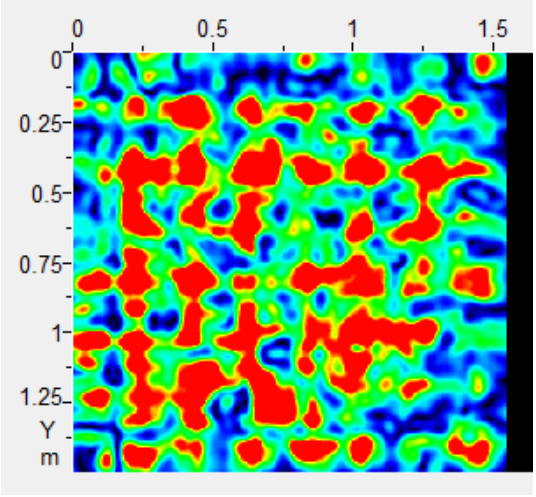

(c) Depth of 280 mm z =0.28 m

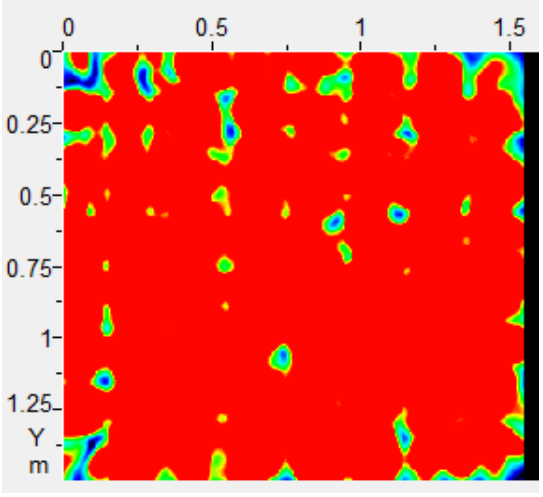

(d) Depth of 300 mm z =0.30 m

Figure A.8: C-Scans of Slab III at Various Depths from 210 mm to 300 mm

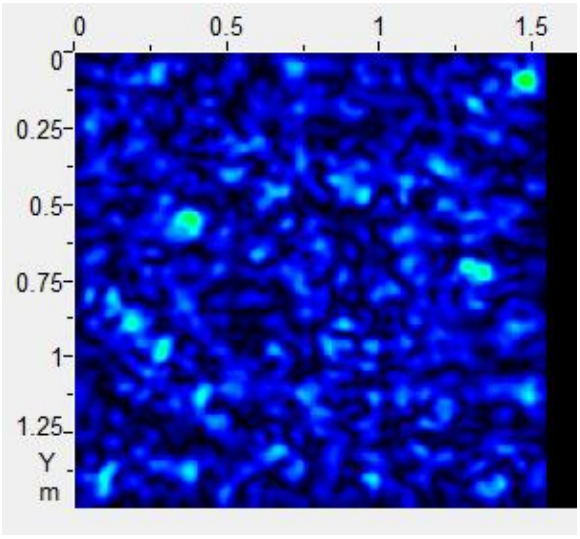

(a) Depth of 60 mm, Vertical Orientation

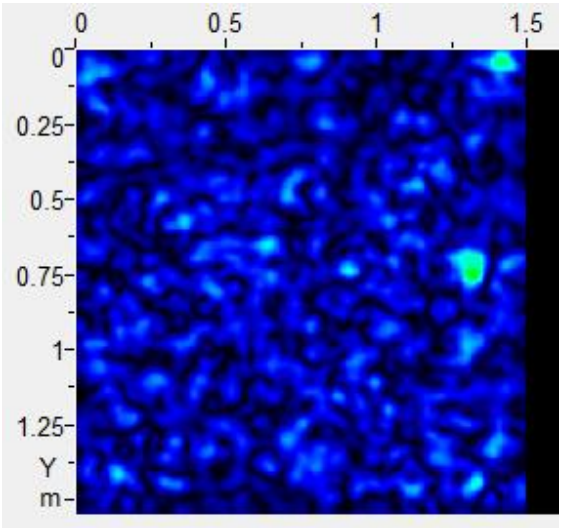

(b) Depth of 60 mm, Horizontal Orientation

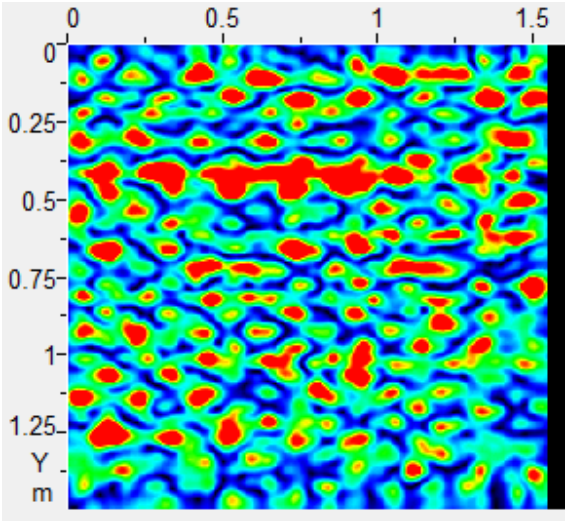

(c) Depth of 120 mm, Vertical Orientation

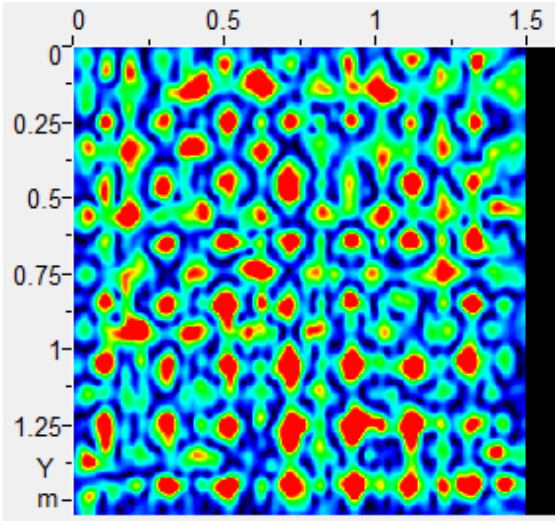

(d) Depth of 120 mm, Horizontal Orientation

Figure A.9: C-Scans of Slab III with the Vertical (left) and Horizontal (right) Orientations at 60 mm and 120 mm

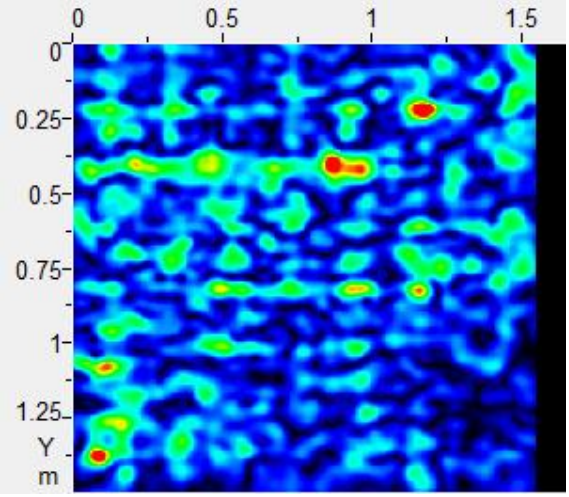

(a) Depth of 170 mm, Vertical Orientation

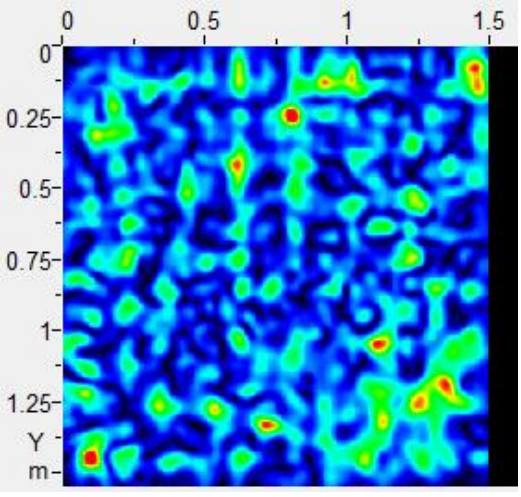

(b) Depth of 170 mm, Horizontal Orientation

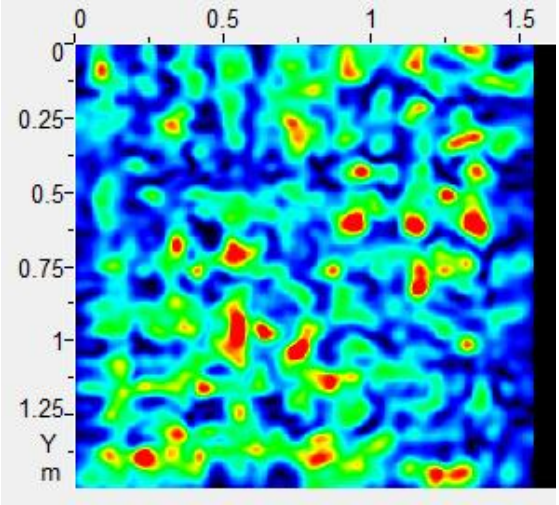

(c) Depth of 220 mm, Vertical Orientation

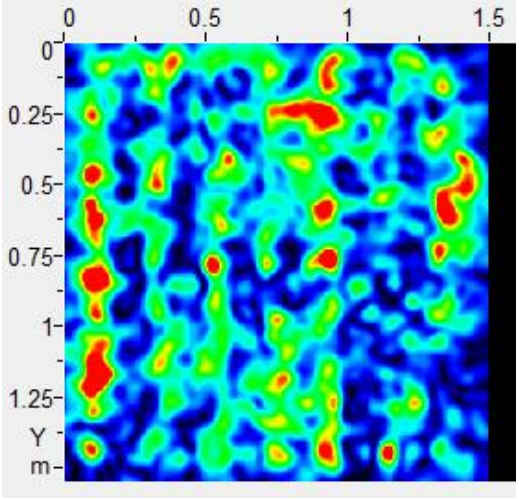

(d) Depth of 220 mm, Horizontal Orientation

Figure A.10: C-Scans of Slab III with the Vertical (left) and Horizontal (right) Orientations at 170 mm and 220 mm

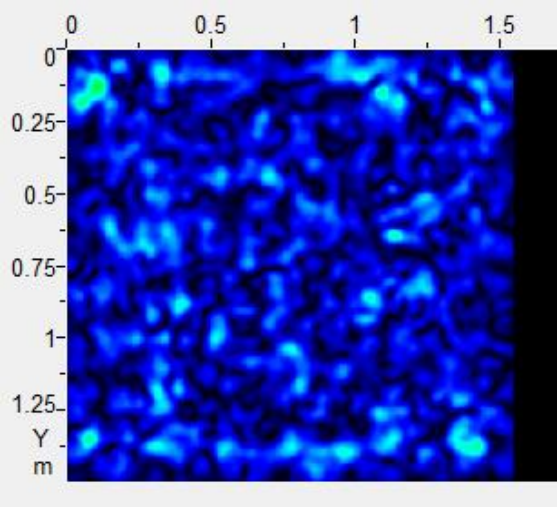

(a) Depth of 90 mm z =0.09 m

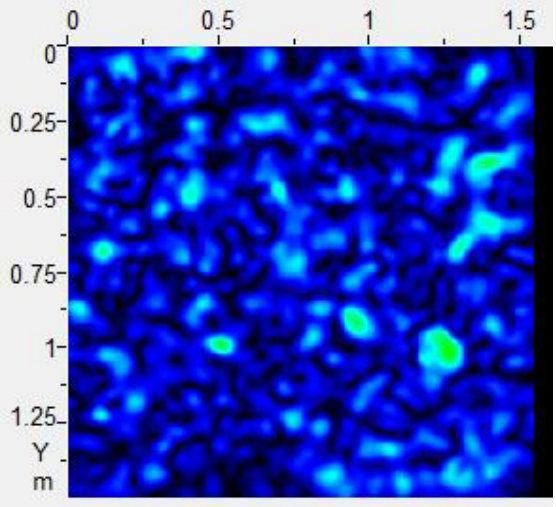

(b) Depth of 180 mm z =0.18 m

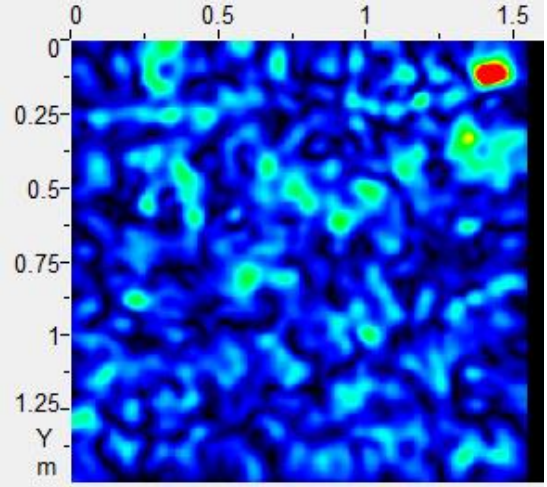

(c) Depth of 330 mm z =0.33 m

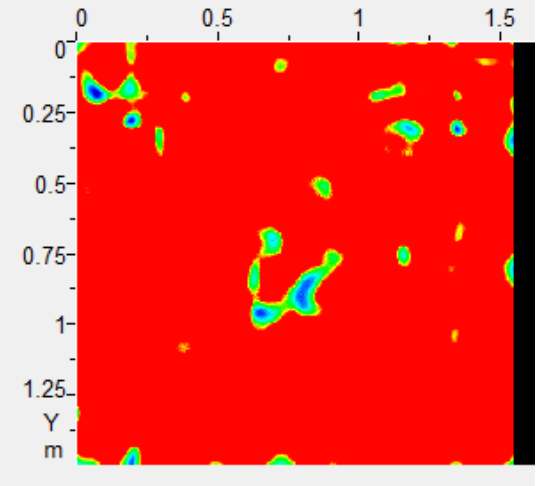

(d) Depth of 610 mm z =0.61 m

Figure A.11: C-Scans of Slab IV at Various Depths from 90 mm to 610 mm

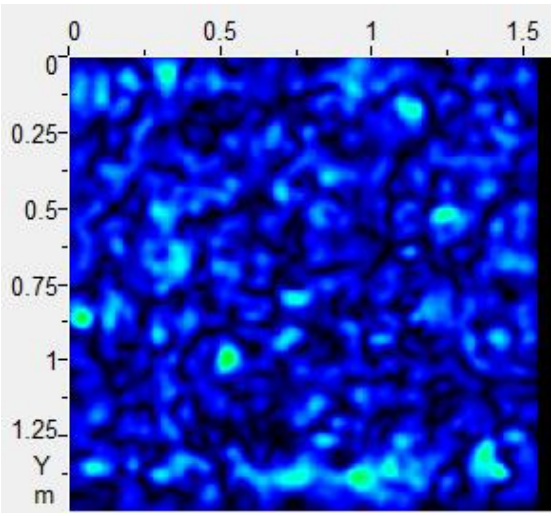

(a) Depth of 120 mm, Vertical Orientation

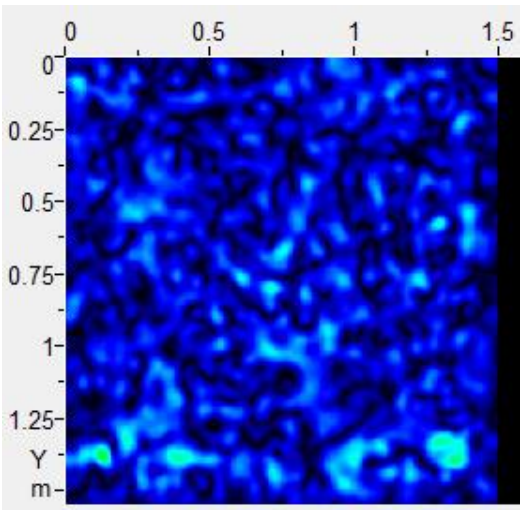

(b) Depth of 120 mm, Horizontal Orientation

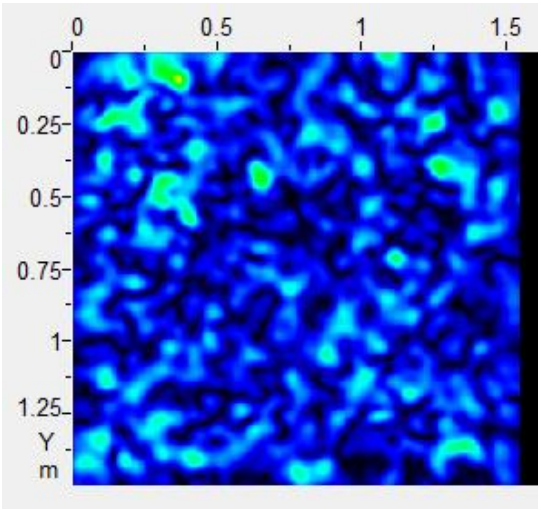

(c) Depth of 240 mm, Vertical Orientation

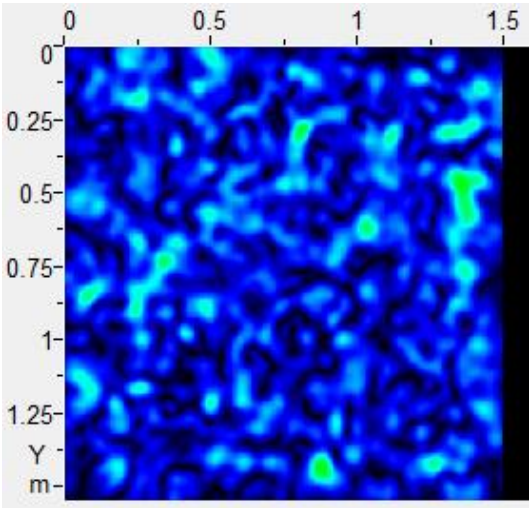

(d) Depth of 240 mm, Horizontal Orientation

Figure A.12: C-Scans of Slab IV with the Vertical (left) and Horizontal (right) Orientations at 120 mm and 240 mm

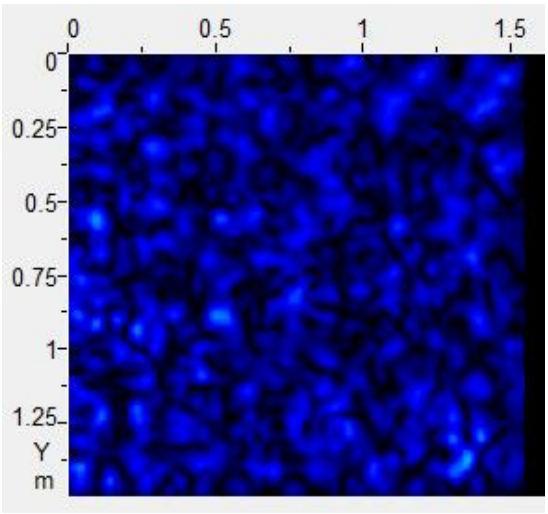

(a) Depth of 60 mm z =0.06 m

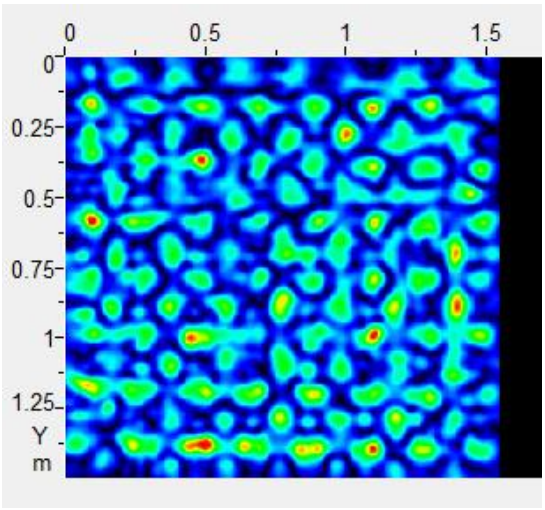

(b) Depth of 100 mm z =0.10 m

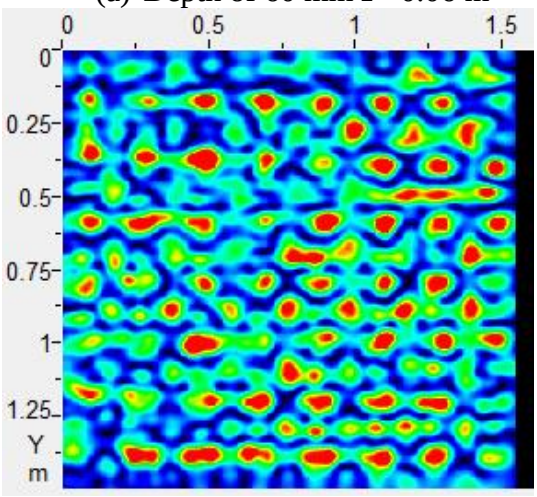

(c) Depth of 130 mm z =0.13 m

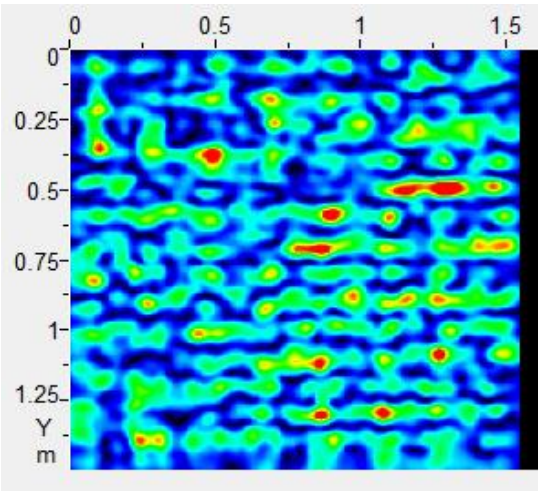

(d) Depth of 150 mm z =0.15 m

Figure A.13: C-Scans of Slab V at Various Depths from 60 mm to 150 mm

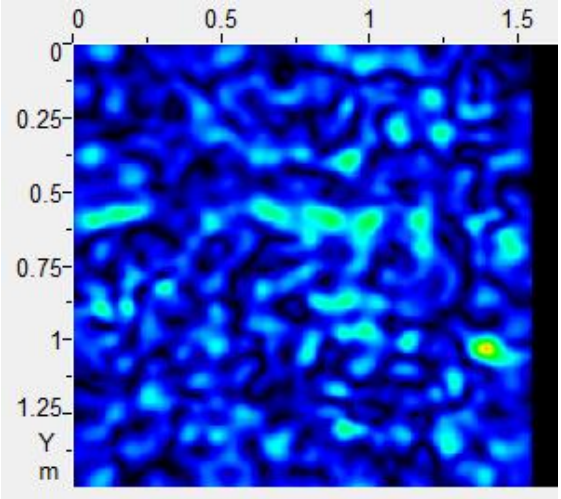

(a) Depth of 330 mm z =0.33 m

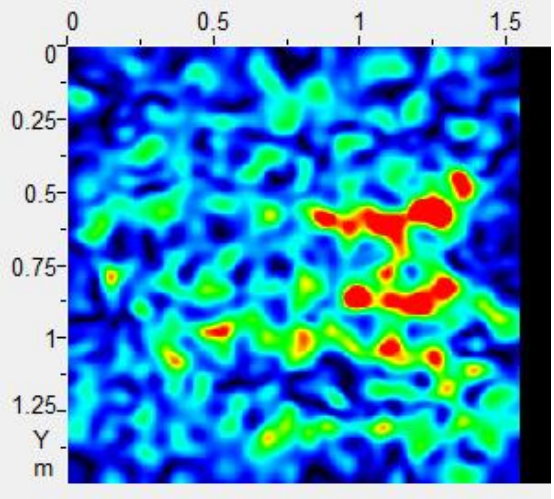

(b) Depth of 480 mm z =0.48 m

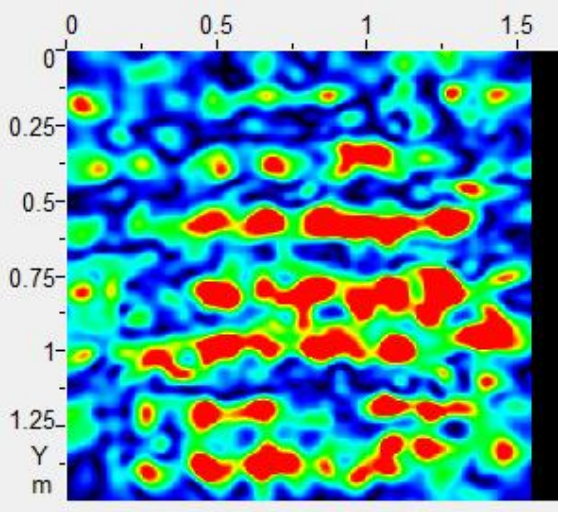

(c) Depth of 530 mm z =0.53 m

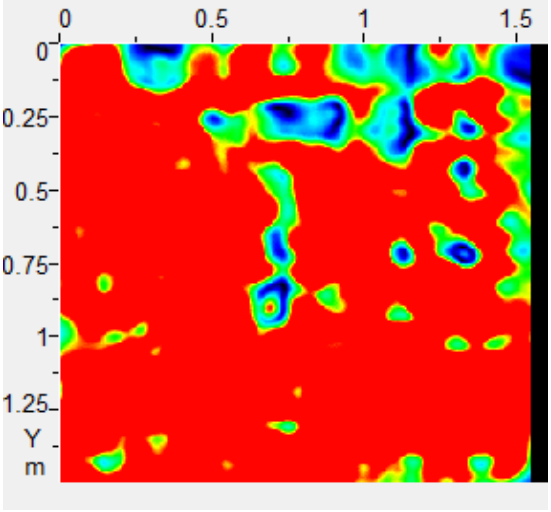

(d) Depth of 610 mm z =0.61 m

Figure A.14: C-Scans of Slab V at Various Depths from 330 mm to 610 mm

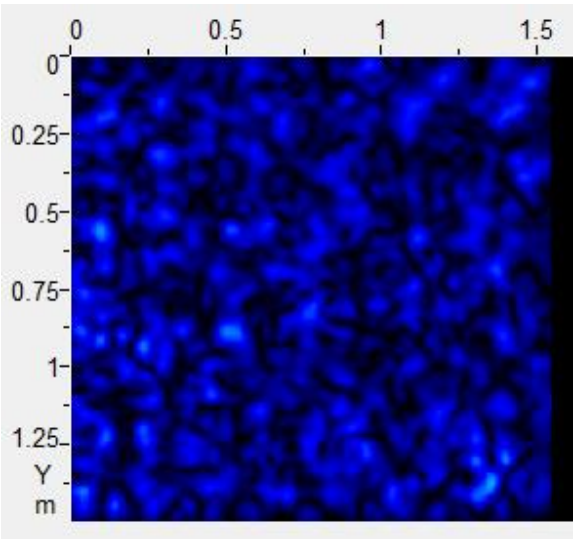

(a) Depth of 60 mm, Vertical Orientation

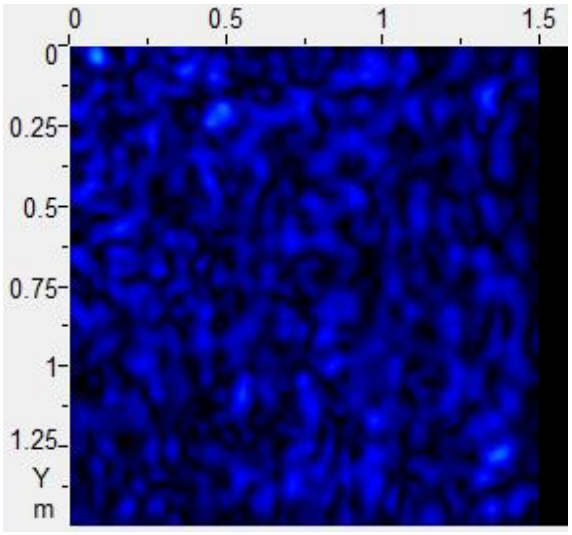

(b) Depth of 60 mm, Horizontal Orientation

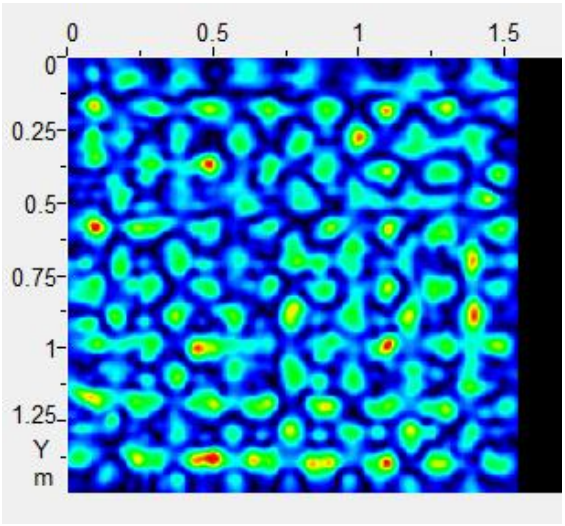

(c) Depth of 100 mm, Vertical Orientation

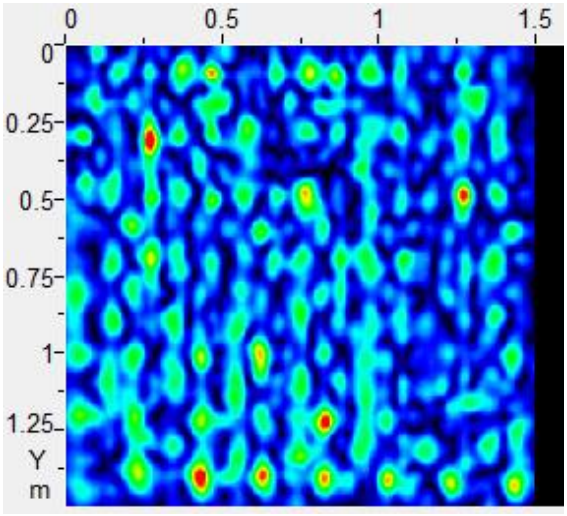

(d) Depth of 100 mm, Horizontal Orientation

Figure A.15: C-Scans of Slab V with the Vertical (left) and Horizontal (right) Orientations at 60 mm and 100 mm

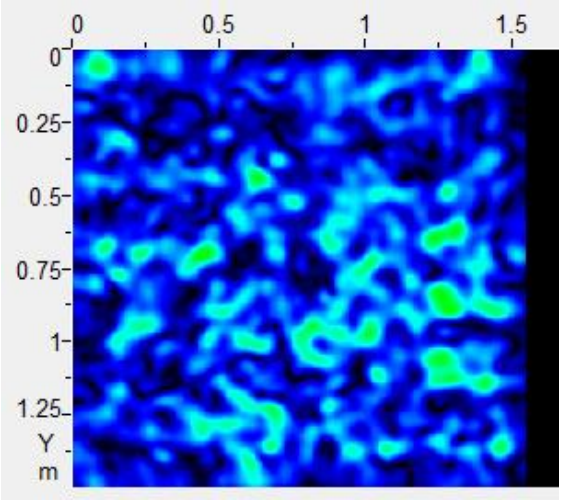

(a) Depth of 240 mm, Vertical Orientation

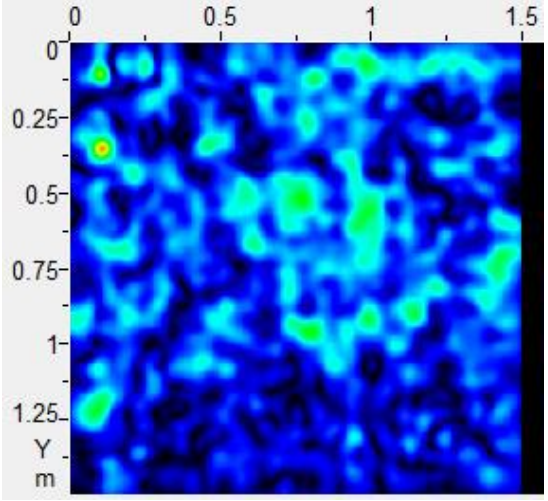

(b) Depth of 240 mm, Horizontal Orientation

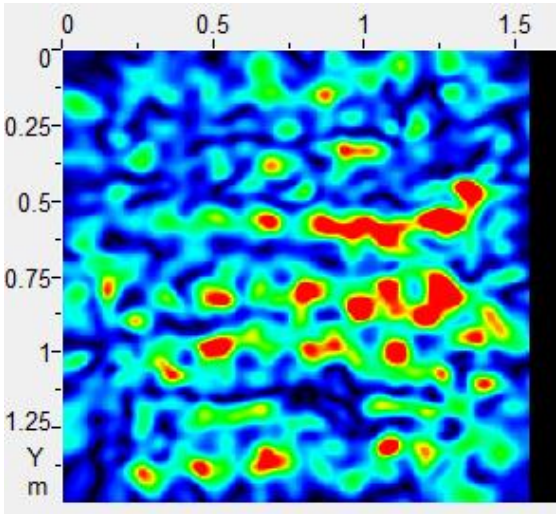

(c) Depth of 520 mm, Vertical Orientation

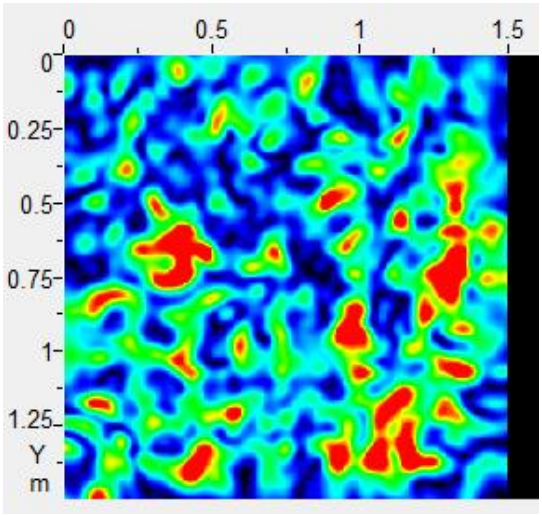

(d) Depth of 520 mm, Horizontal Orientation

Figure A.16: C-Scans of Slab V with the Vertical (left) and Horizontal (right) Orientations at 240 mm and 520 mm

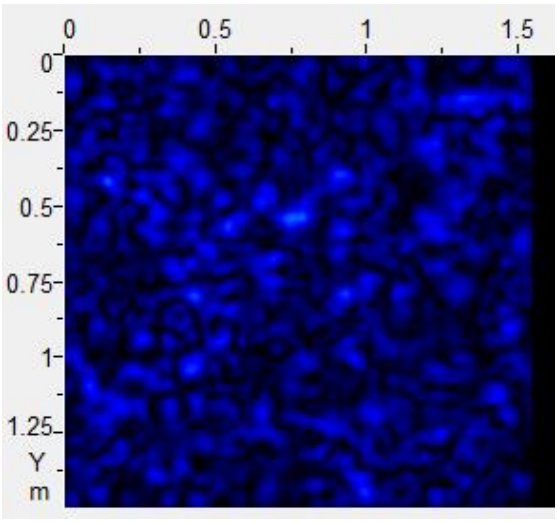

(a) Depth of 30 mm z =0.03 m

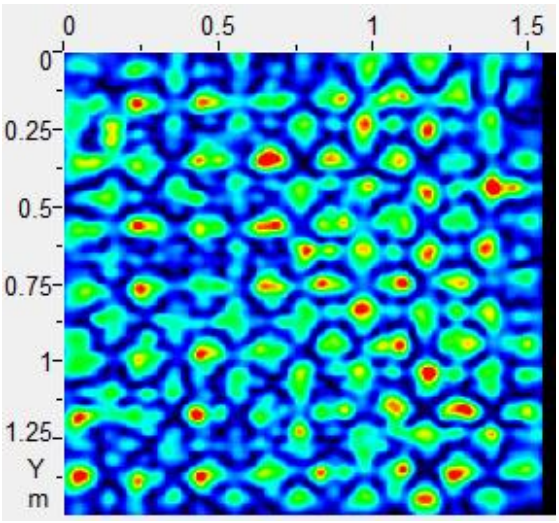

(b) Depth of 100 mm z =0.10 m

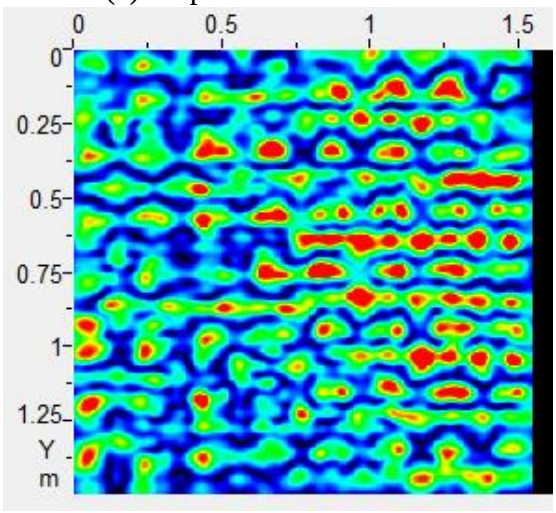

(c) Depth of 130 mm z =0.13 m

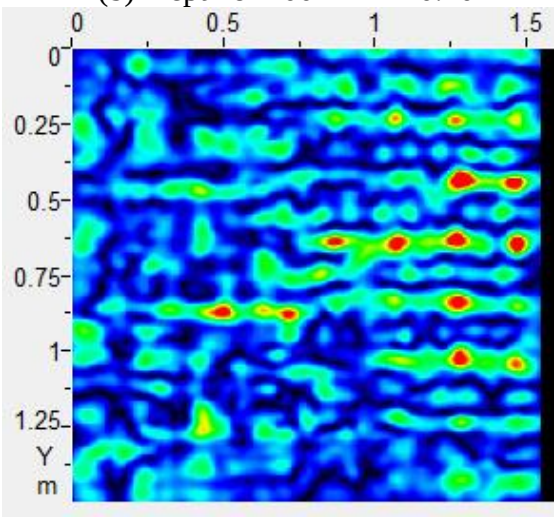

(d) Depth of 150 mm z =0.15 m

Figure A.17: C-Scans of Slab VI at Various Depths from 30 mm to 150 mm

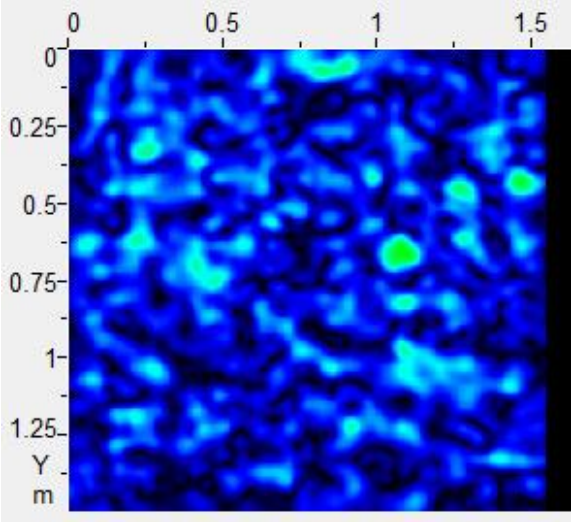

(a) Depth of 200 mm z =0.20 m

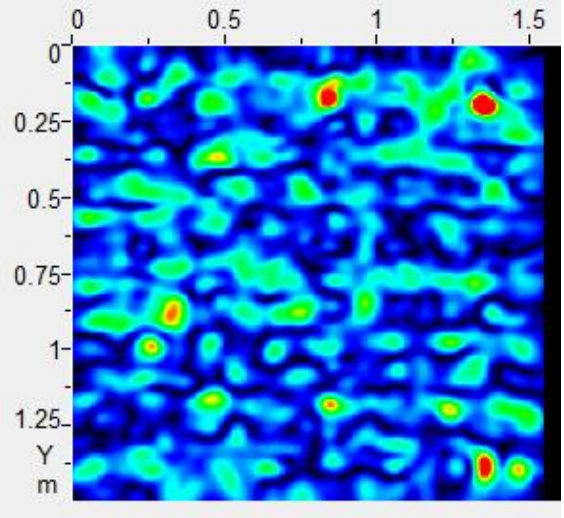

(b) Depth of 280 mm z =0.28 m

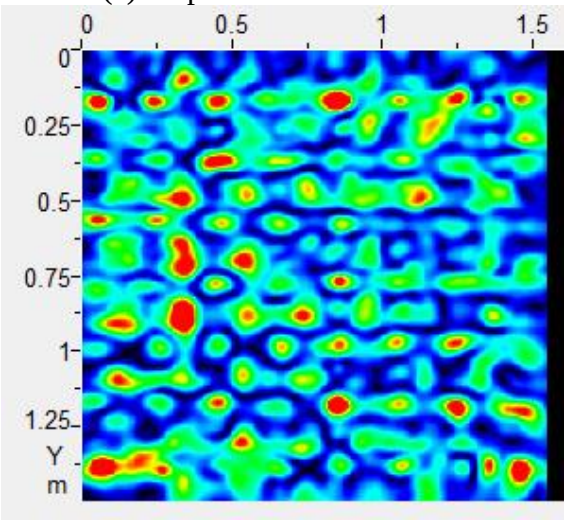

(c) Depth of 300 mm z =0.30 m

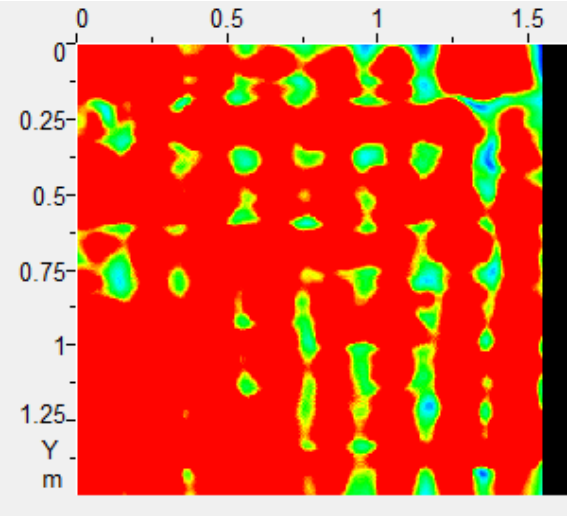

(d) Depth of 380 mm z =0.38 m

Figure A.18: C-Scans of Slab VI at Various Depths from 200 mm to 380 mm

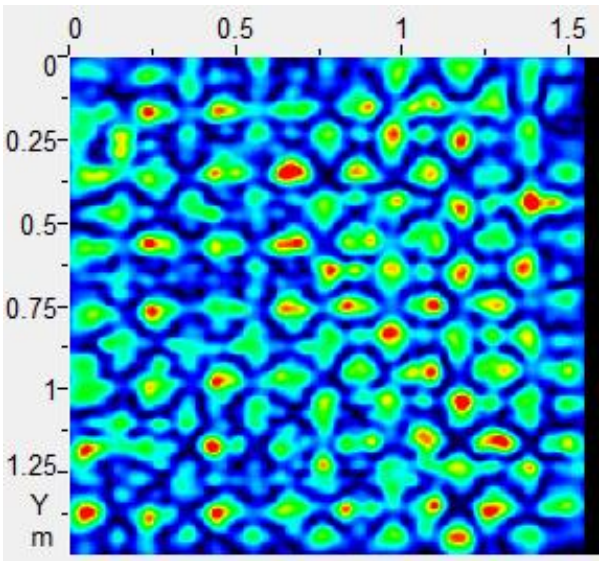

(a) Depth of 100 mm, Vertical Orientation

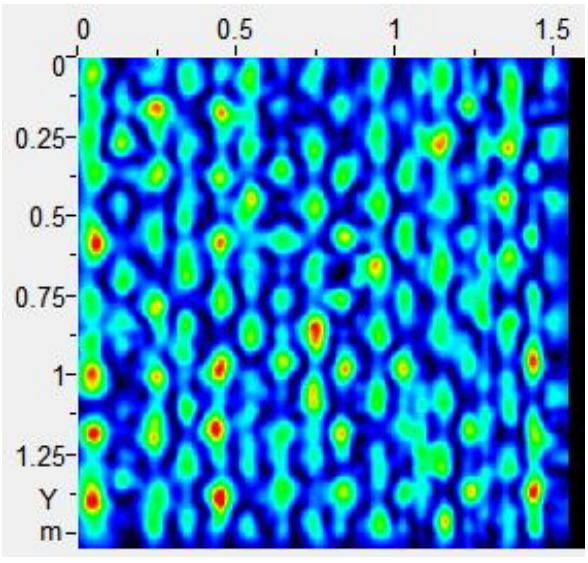

(b) Depth of 100 mm, Horizontal Orientation

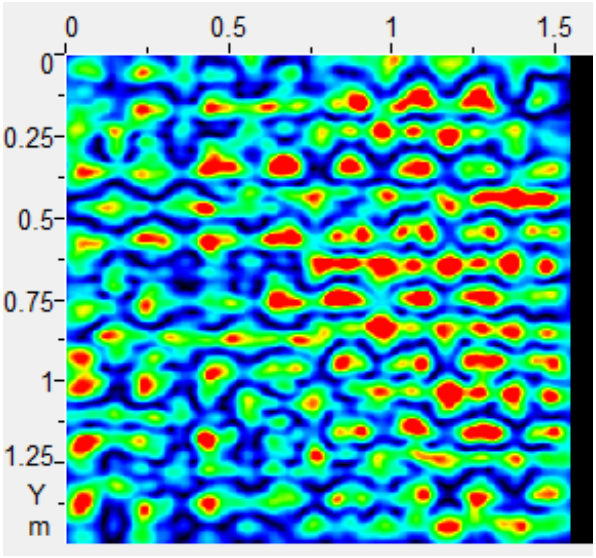

(c) Depth of 120 mm, Vertical Orientation

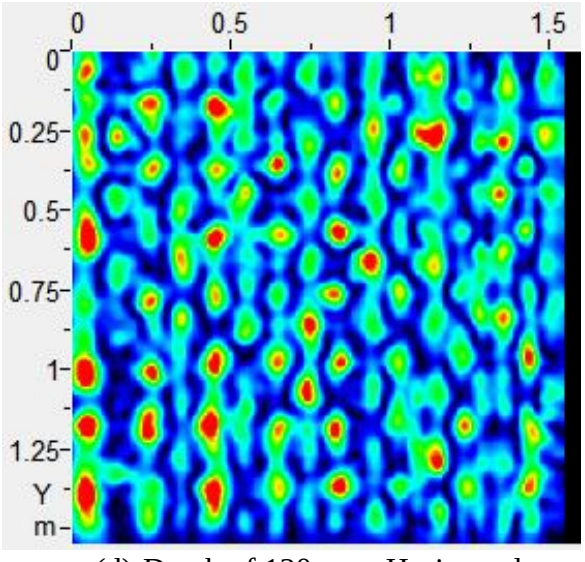

(d) Depth of 120 mm, Horizontal Orientation

Figure A.19: C-Scans of Slab VI with the Vertical (left) and Horizontal (right) Orientations at 100 mm and 120 mm

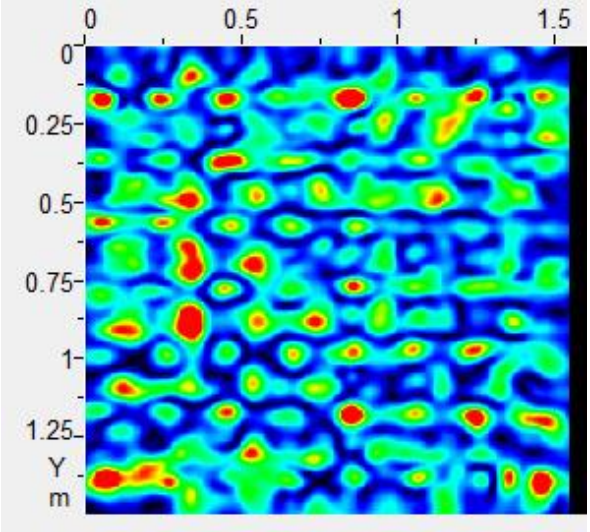

(a) Depth of 300 mm, Vertical Orientation

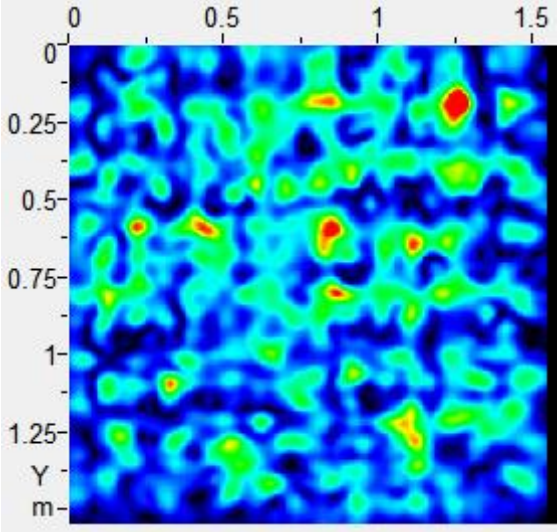

(b) Depth of 300 mm, Horizontal Orientation

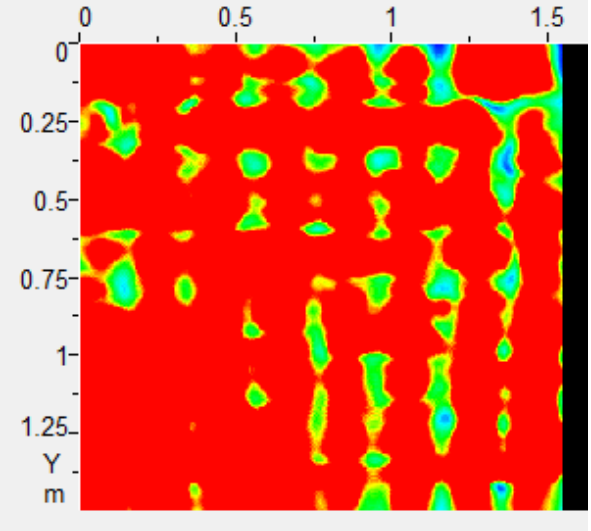

(c) Depth of 380 mm, Vertical Orientation

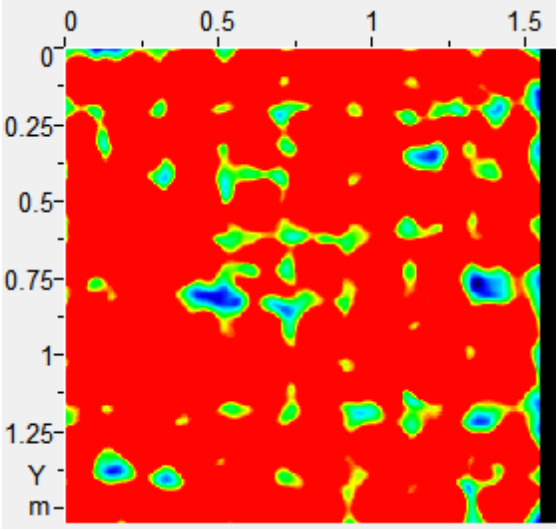

(d) Depth of 380 mm, Horizontal Orientation

Figure A.20: C-Scans of Slab VI with the Vertical (left) and Horizontal (right) Orientations at 300 mm and 380 mm

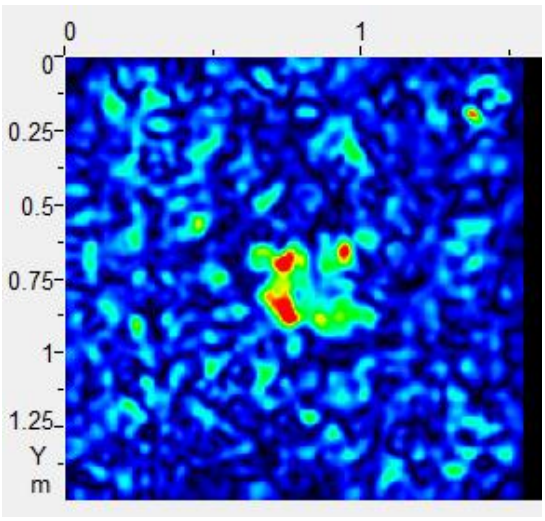

(a) Depth of 70 mm z =0.07 m

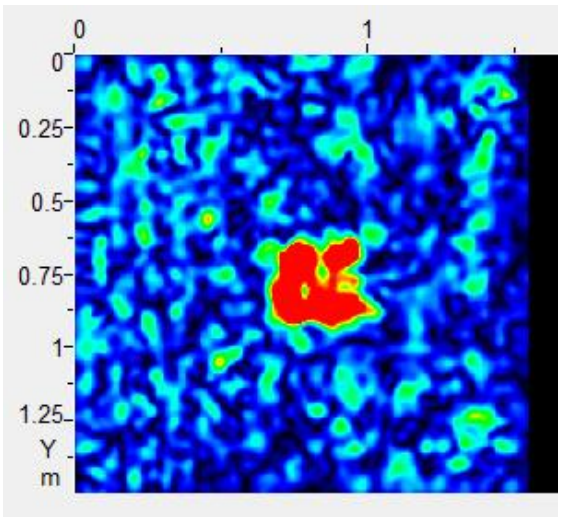

(b) Depth of 80 mm z =0.08 m

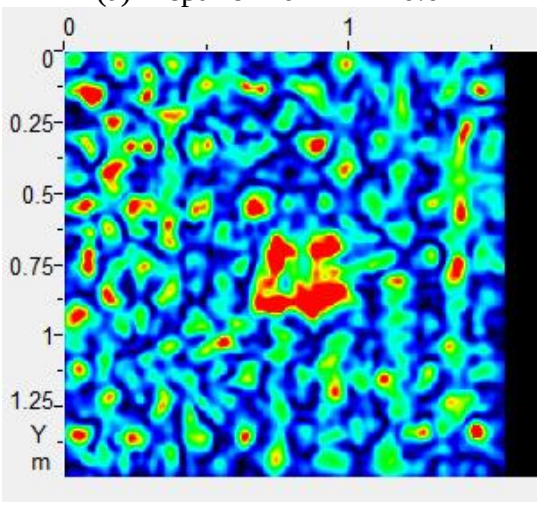

(c) Depth of 100 mm z =0.10 m

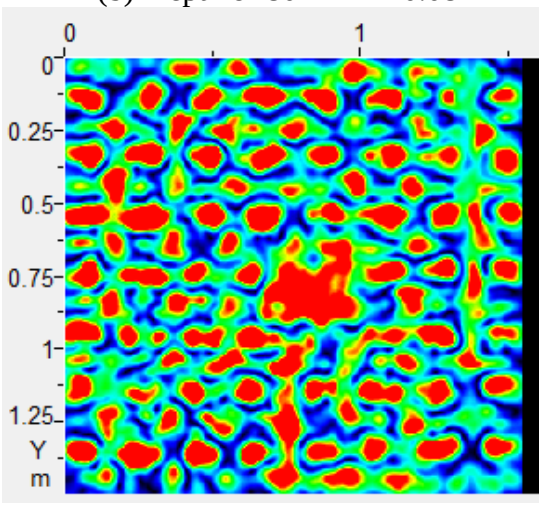

(d) Depth of 130 mm z =0.13 m

Figure A.21: C-Scans of Slab VII at Various Depths from 70 mm to 130 mm

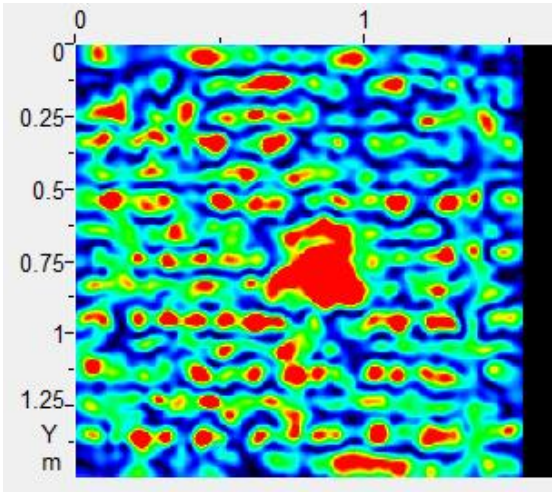

(a) Depth of 160 mm z =0.16 m

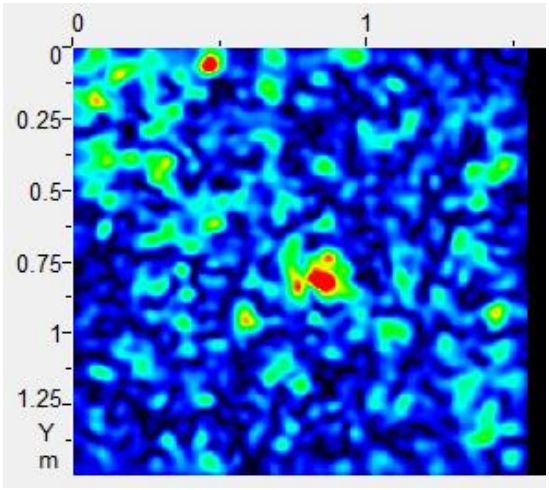

(b) Depth of 190 mm z =0.19 m

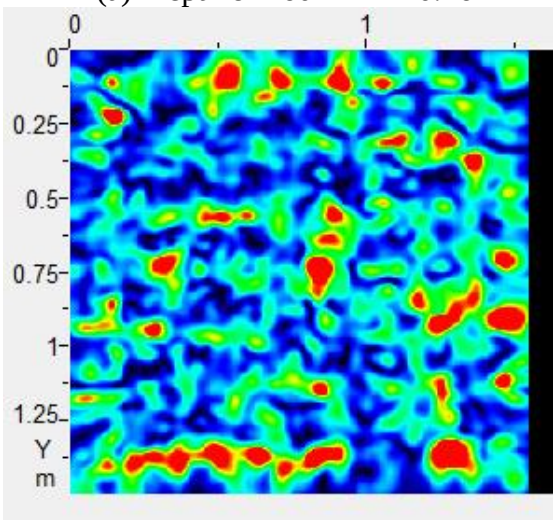

(c) Depth of 290 mm z =0.29 m

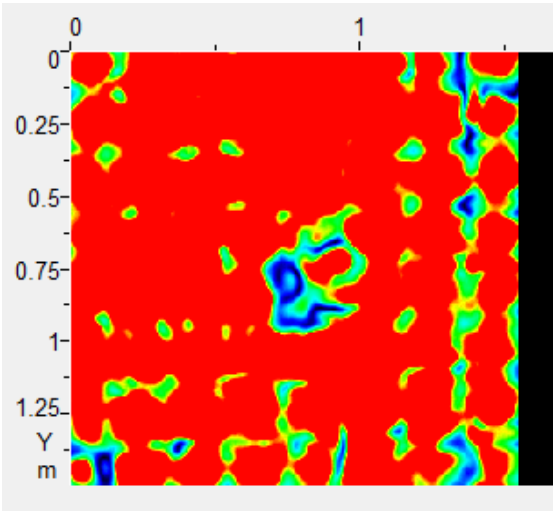

(d) Depth of 380 mm z =0.38 m

Figure A.22: C-Scans of Slab VII at Various Depths from 160 mm to 380 mm

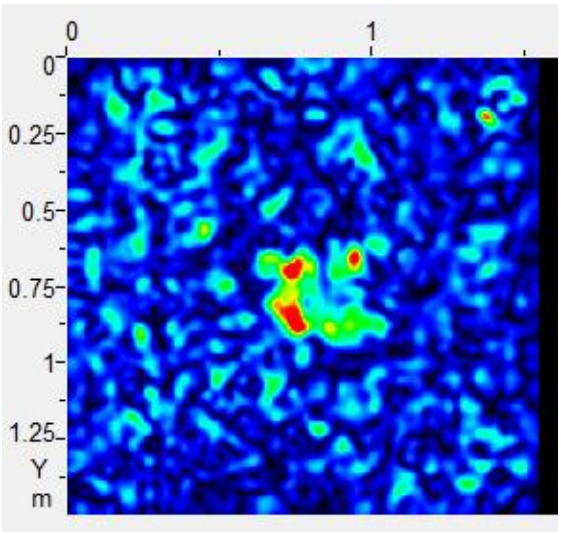

(a) Depth of 70 mm, Vertical Orientation

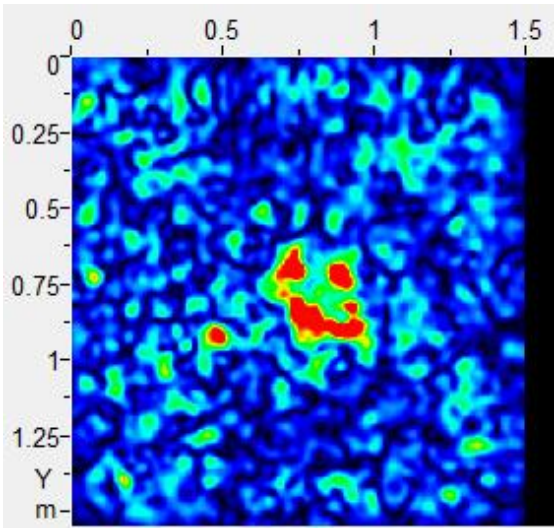

(b) Depth of 70 mm, Horizontal Orientation

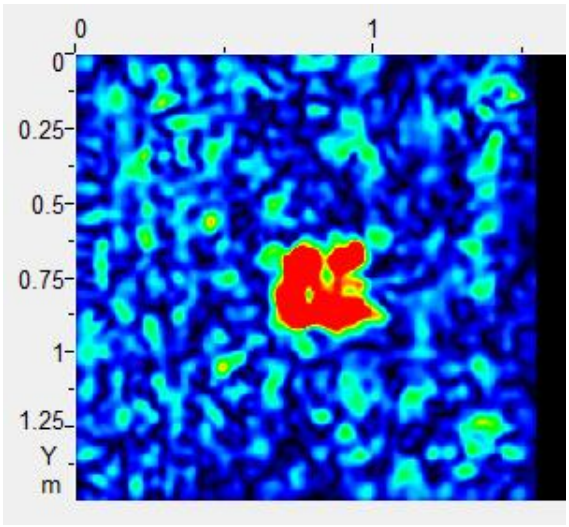

(c) Depth of 80 mm, Vertical Orientation

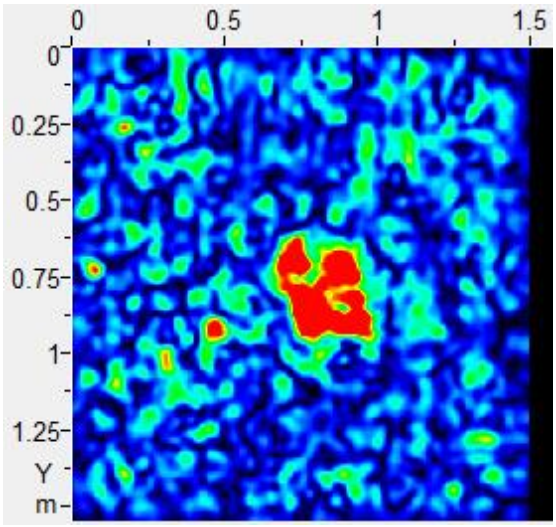

(d) Depth of 80 mm, Horizontal Orientation

Figure A.23: C-Scans of Slab VII with the Vertical (left) and Horizontal (right) Orientations at 70 mm and 80 mm

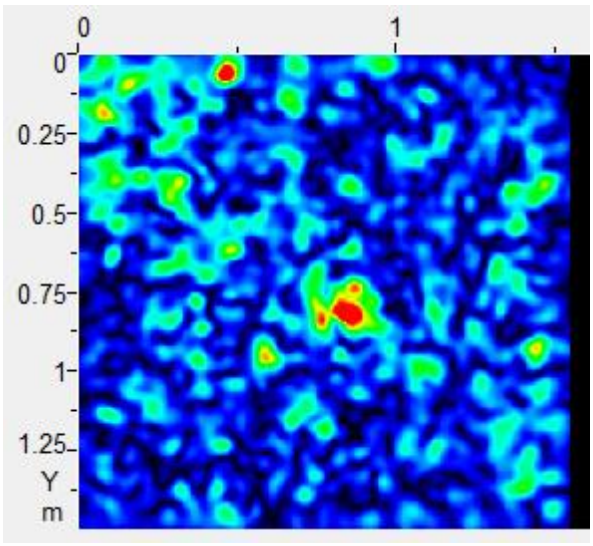

(a) Depth of 190 mm, Vertical Orientation

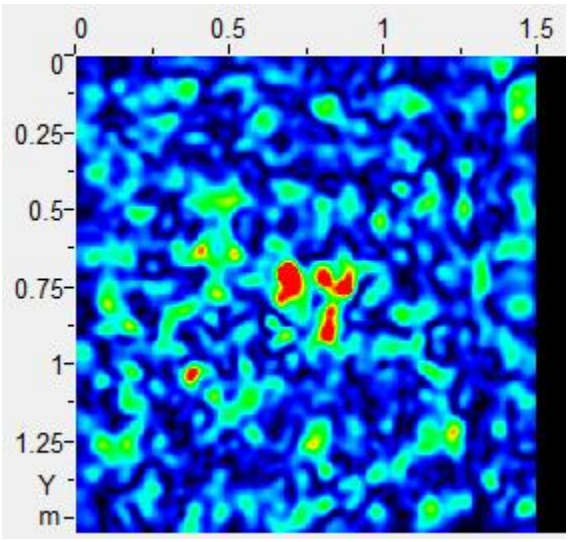

(b) Depth of 190 mm, Horizontal Orientation

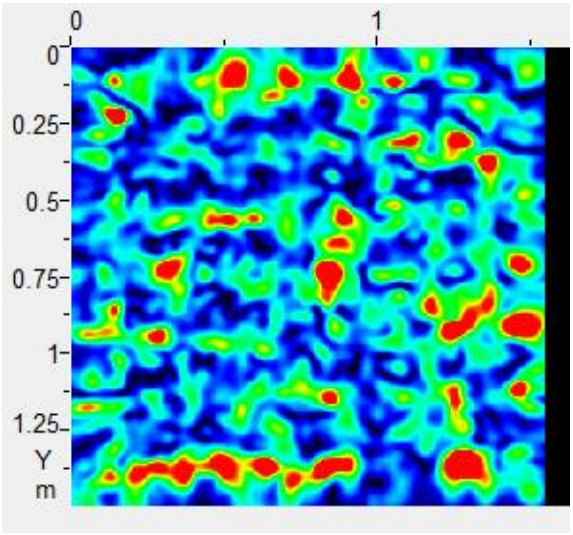

(c) Depth of 290 mm, Vertical Orientation

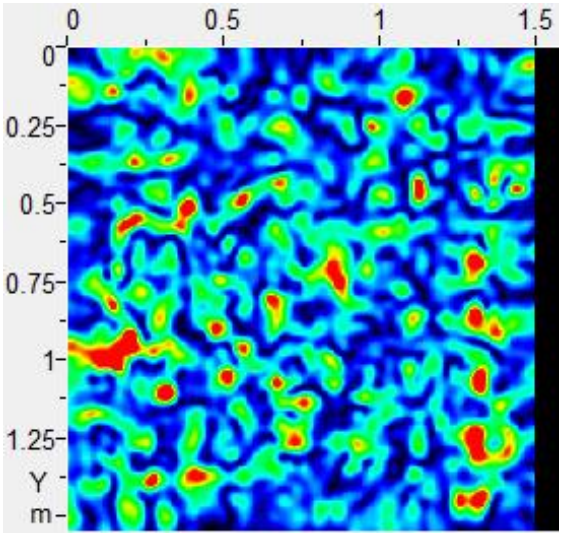

(d) Depth of 290 mm, Horizontal Orientation

Figure A.24: C-Scans of Slab VII with the Vertical (left) and Horizontal (right) at 190 mm and 290 mm

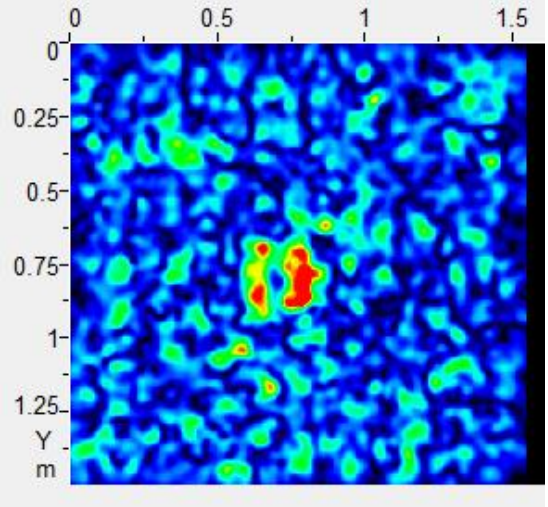

(a) Depth of 80 mm z =0.08 m

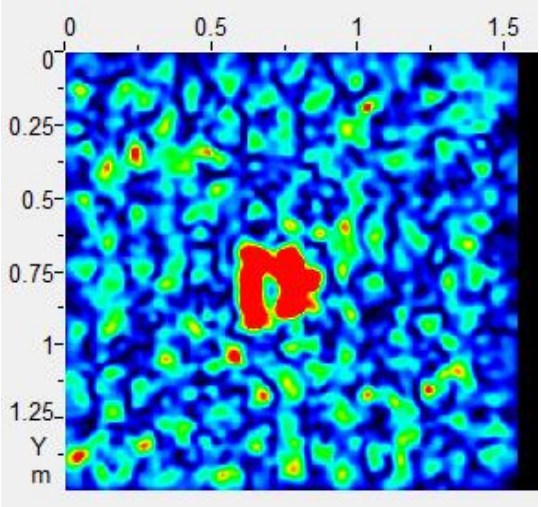

(b) Depth of 90 mm z =0.09 m

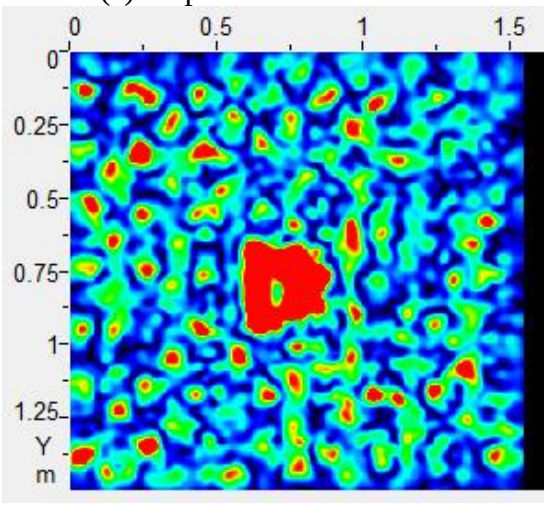

(c) Depth of 100 mm z =0.10 m

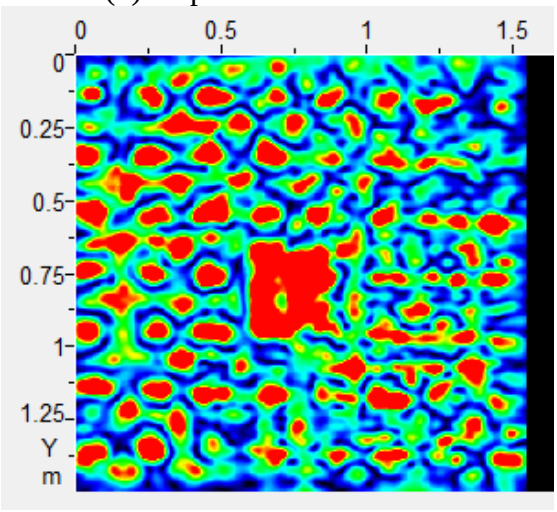

(d) Depths of 130 mm z =0.13 m

Figure A.25: C-Scans of Slab VIII at Various Depths from 80 mm to 100 mm

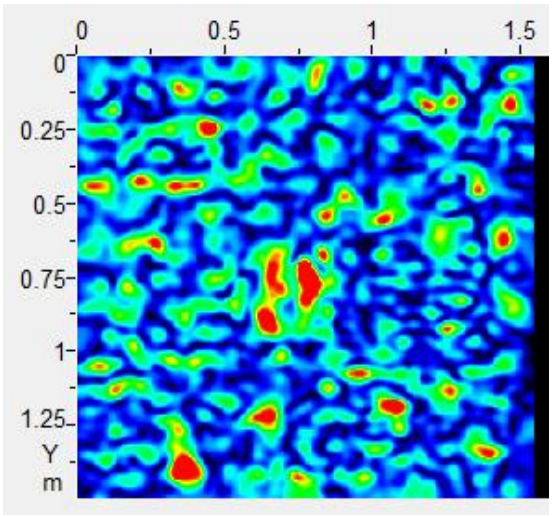

(a) Depth of 160 mm z =0.16 m

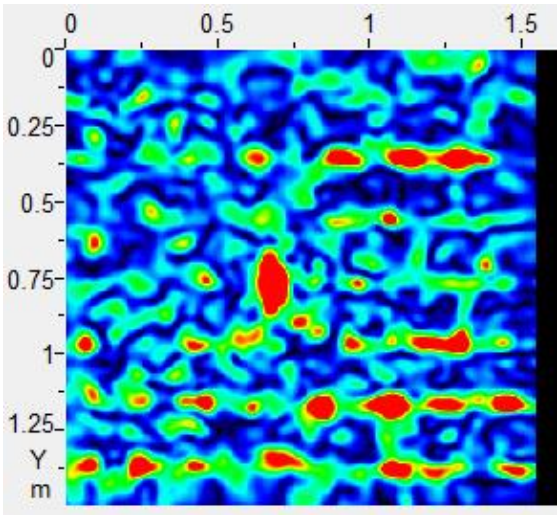

(b) Depth of 260 mm z =0.26 m

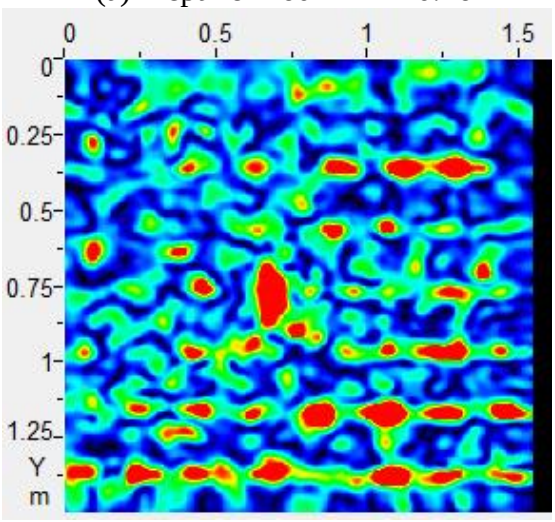

(c) Depth of 270 mm z =0.27 m

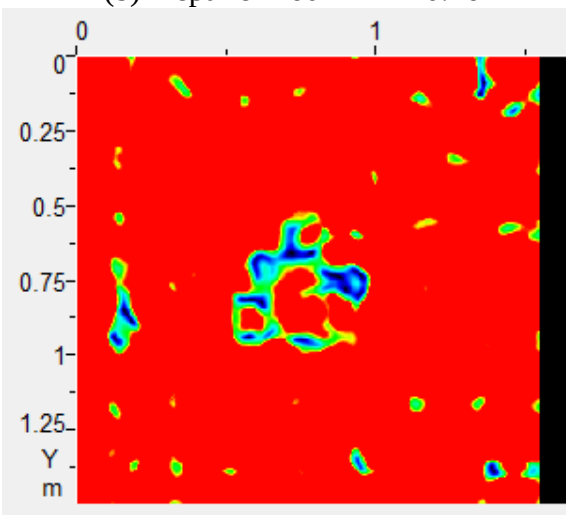

(d) Depth of 370 mm z =0.37 m

Figure A.26: C-Scans of Slab VIII at Various Depths from 160 mm to 370 mm

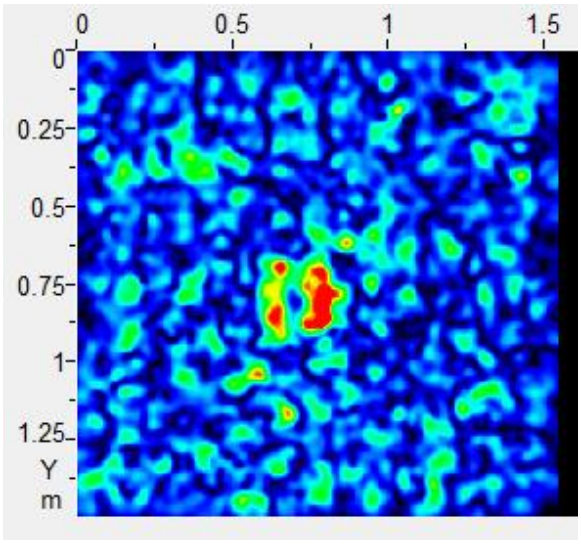

(a) Depth of 80 mm, Vertical Orientation

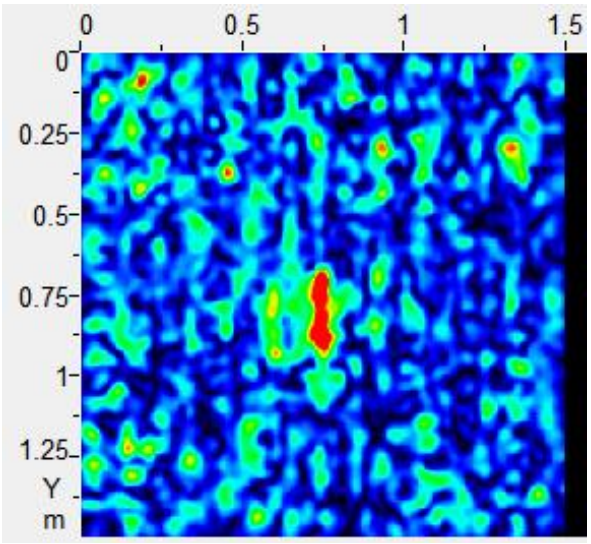

(b) Depth of 80 mm, Horizontal Orientation

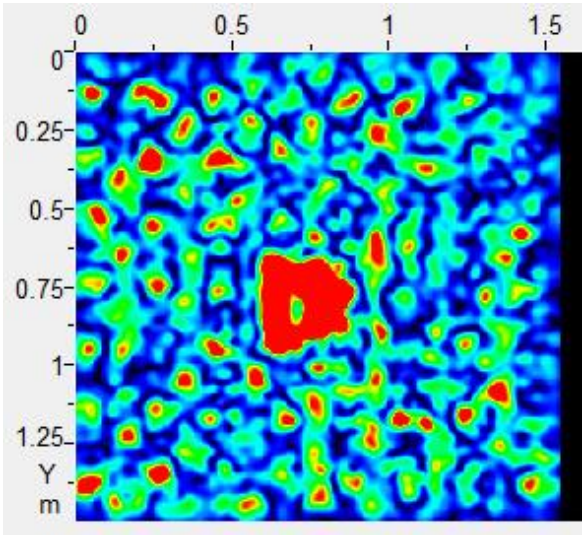

(c) Depth of 100 mm, Vertical Orientation

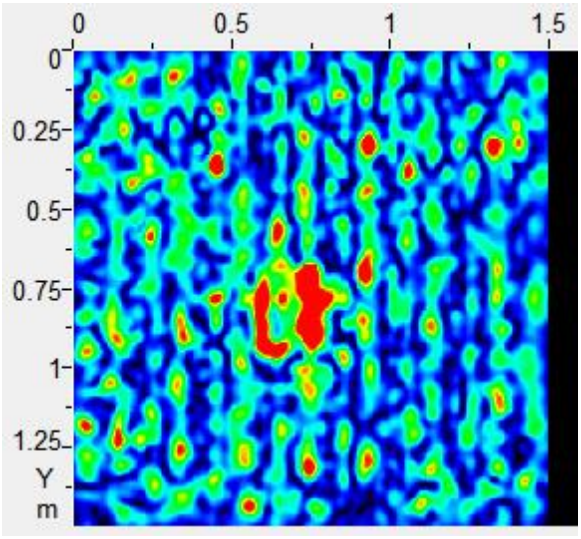

(d) Depth of 100 mm, Horizontal Orientation

Figure A.27: C-Scans of Slab VIII with the Vertical (left) and Horizontal (right) Orientations at 80 mm and 100 mm

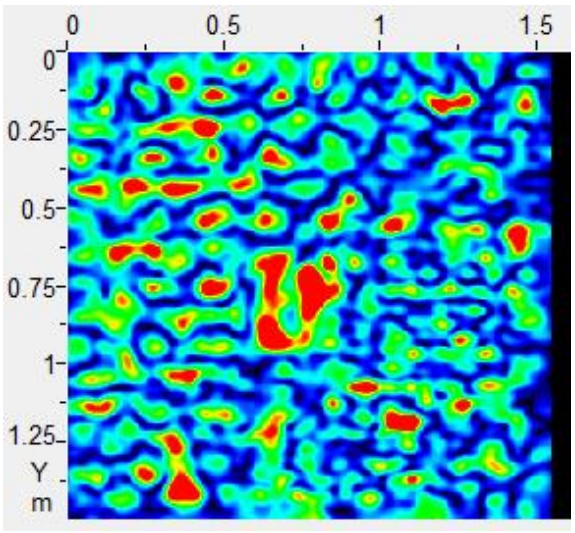

(a) Depth of 150 mm, Vertical Orientation

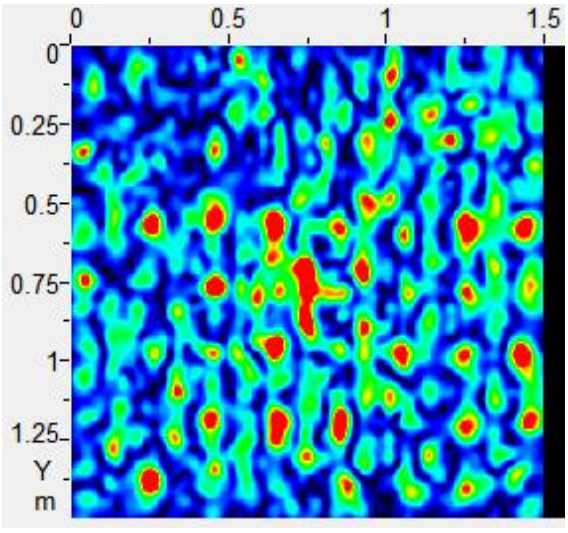

(b) Depth of 150 mm, Horizontal Orientation

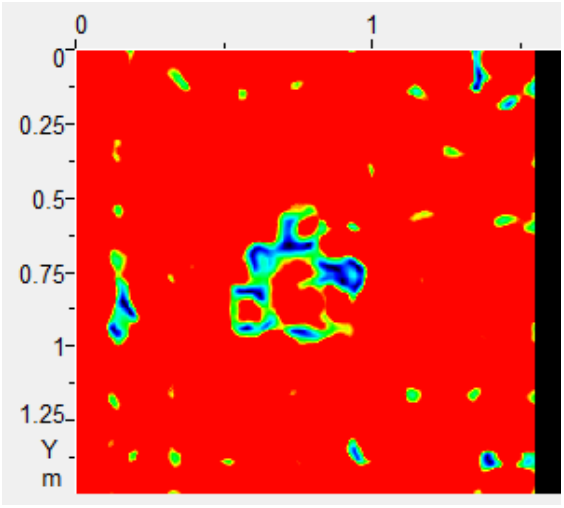

(c) Depth of 370 mm, Vertical Orientation

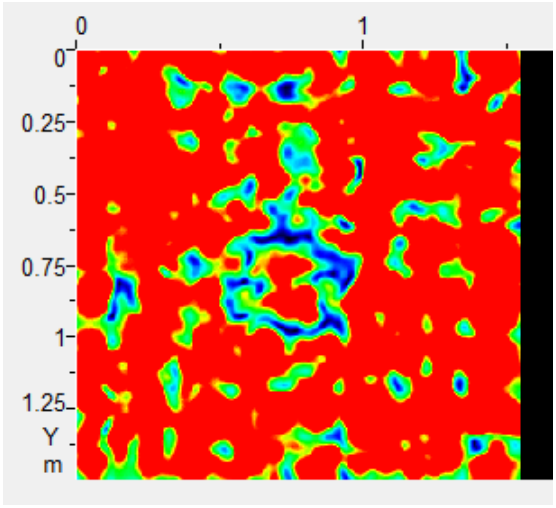

(d) Depth of 370 mm, Horizontal Orientation

Figure A.28: C-Scans of Slab VIII with the Vertical (left) and Horizontal (right) Orientations at 150 mm and 370 mm

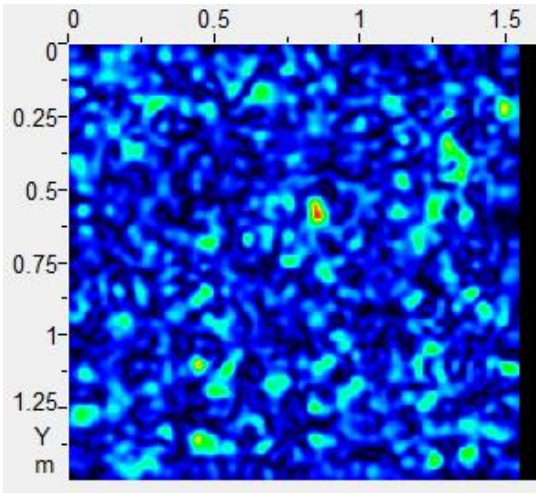

(a) Depth of 40 mm z =0.04 m

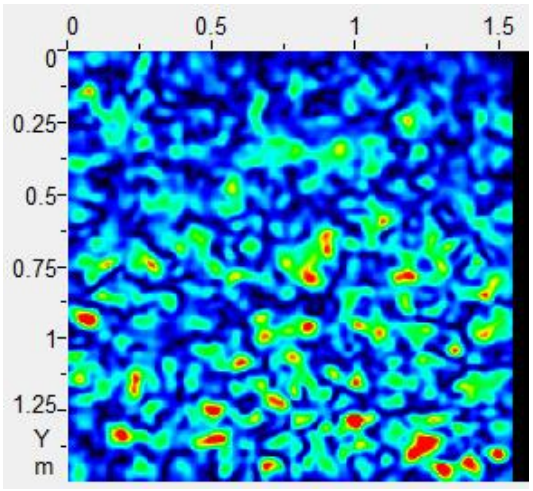

(b) Depth of 100 mm z =0.10 m

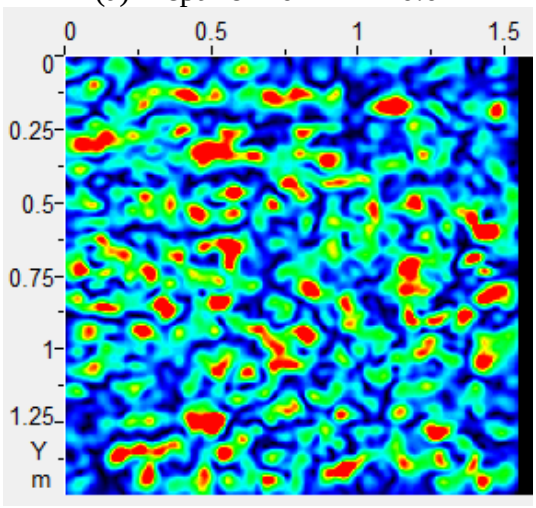

(c) Depth of 130 mm z =0.13 m

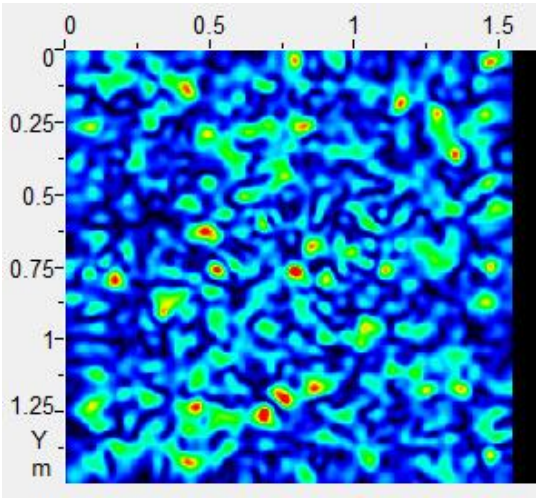

(d) Depth of 170 mm z =0.17 m

Figure A.29: C-Scans of Slab IX at Various Depths from 40 mm to 170 mm

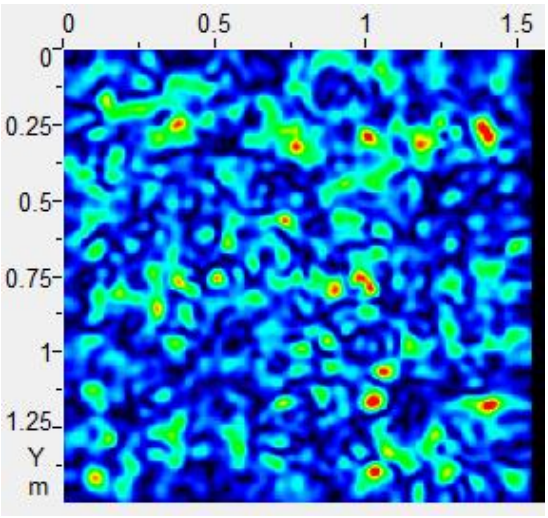

(a) Depth of 210 mm z =0.21 m

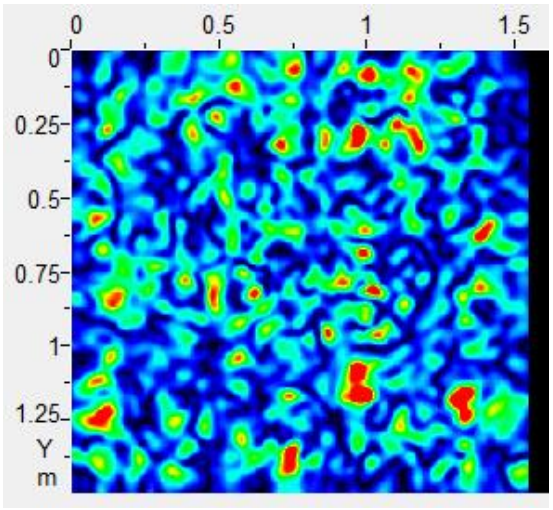

(b) Depth of 250 mm z =0.25 m

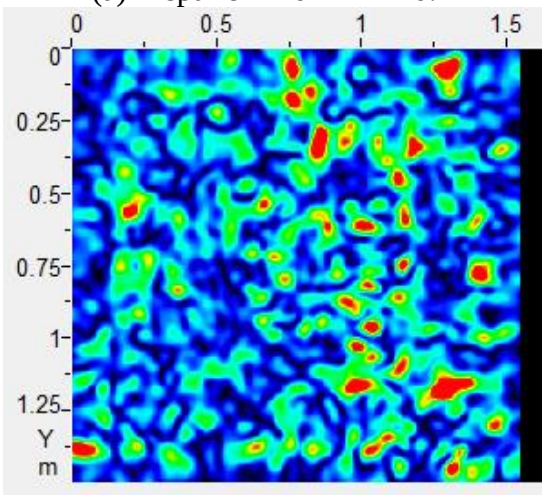

(c) Depth of 270 mm z =0.27 m

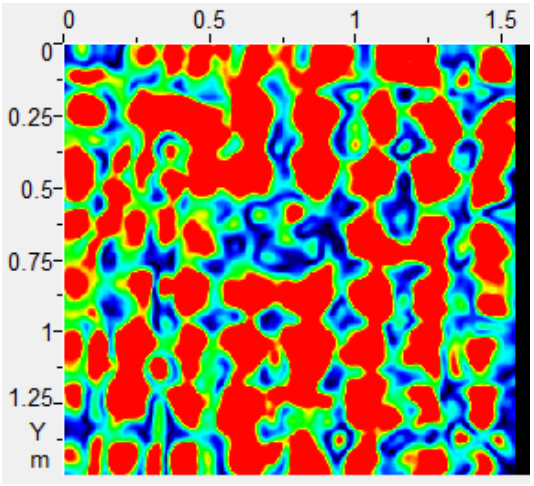

(d) Depth of 380 mm z =0.38 m

Figure A.30: C-Scans of Slab IX at Various Depths from 250 mm to 380 mm

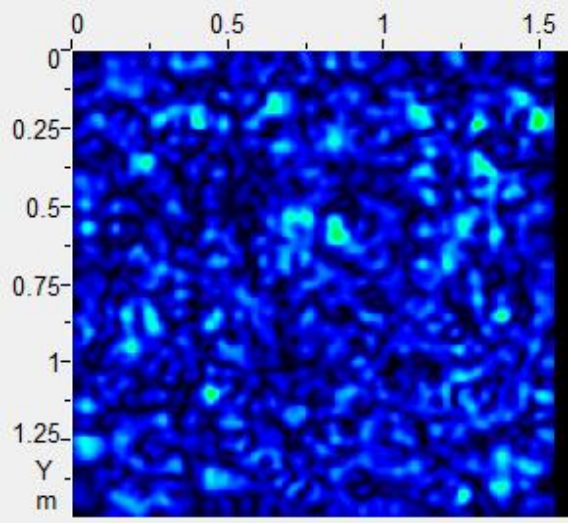

(a) Depth of 30 mm, Vertical Orientation

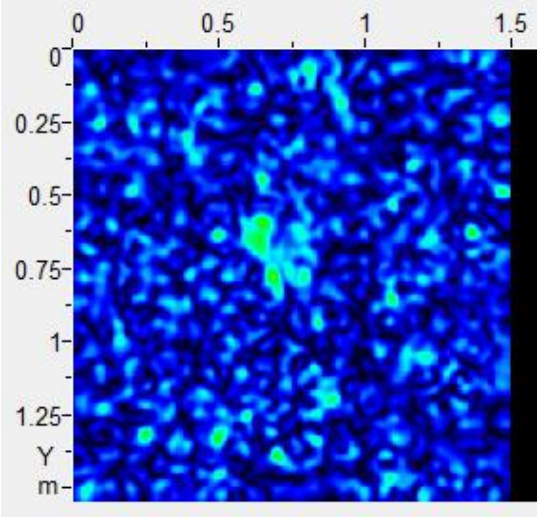

(b) Depth of 30 mm, Horizontal Orientation

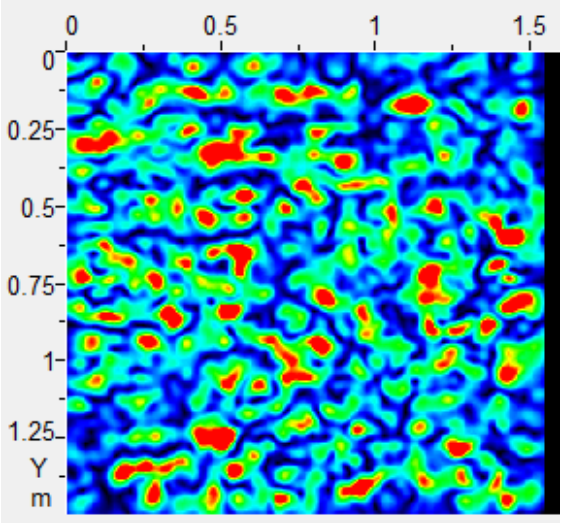

(c) Depth of 130 mm, Vertical Orientation

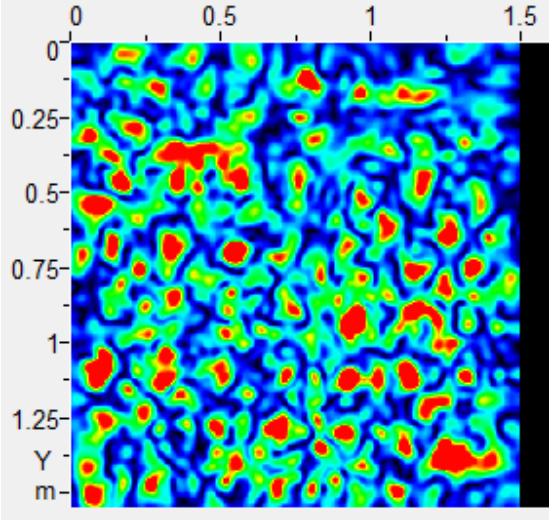

(d) Depth of 130 mm, Horizontal Orientation

Figure A.31: C-Scans of Slab IX with the Vertical (left) and Horizontal (right) Orientations at 30 mm and 130 mm

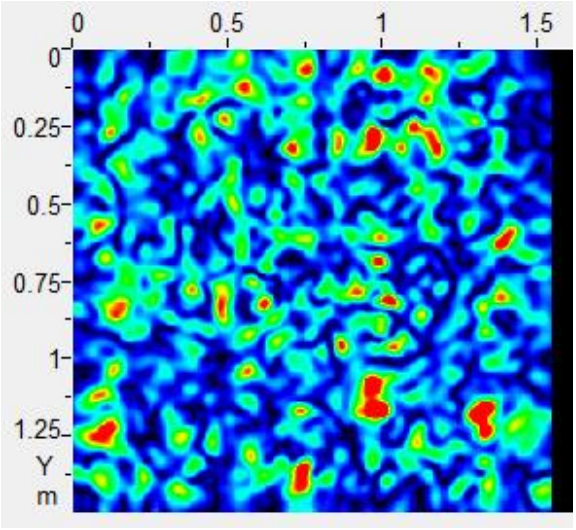

(a) Depth of 250 mm, Vertical Orientation

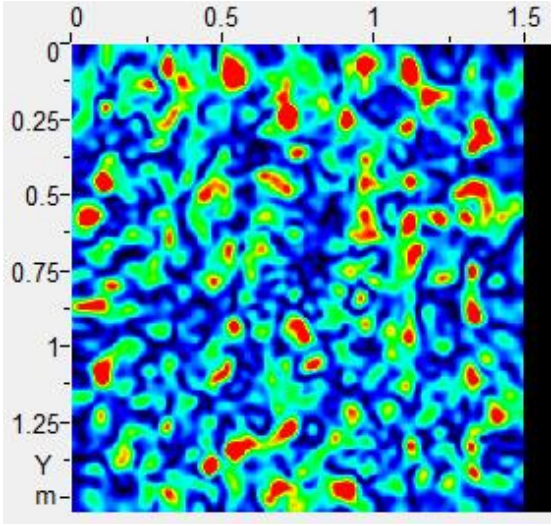

(b) Depth of 250 mm, Horizontal Orientation

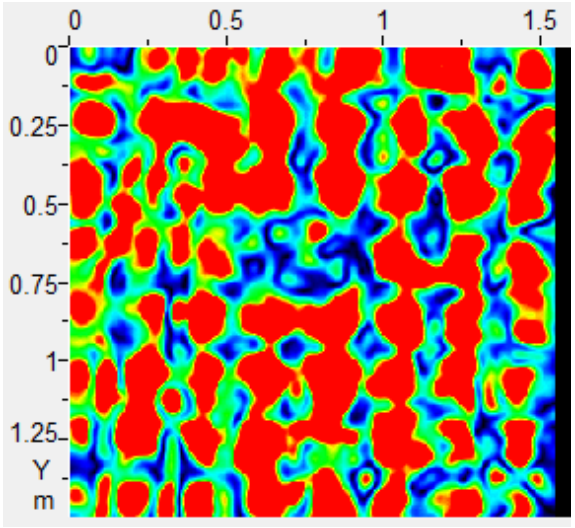

(c) Depth of 380 mm, Vertical Orientation

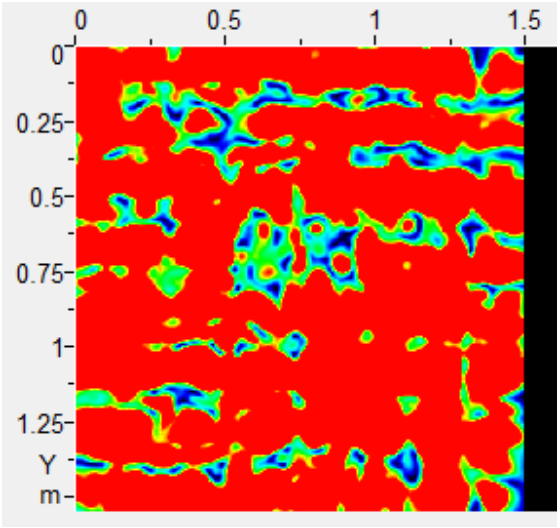

(d) Depth of 380 mm, Horizontal Orientation

Figure A.32: C-Scans of Slab IX with the Vertical (left) and Horizontal (right) Orientations at 250 mm to 380 mm

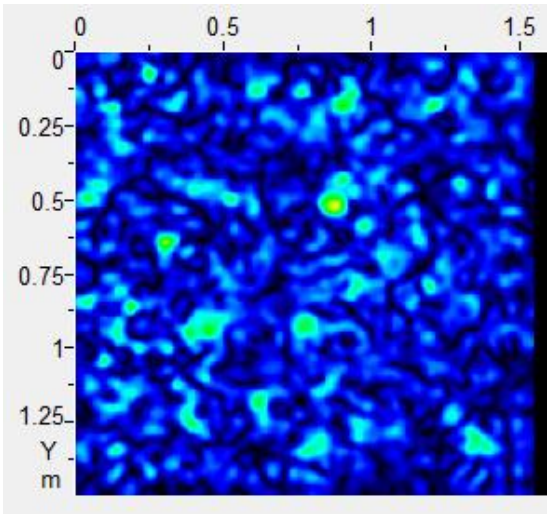

(a) Depth of 60 mm z =0.06 m

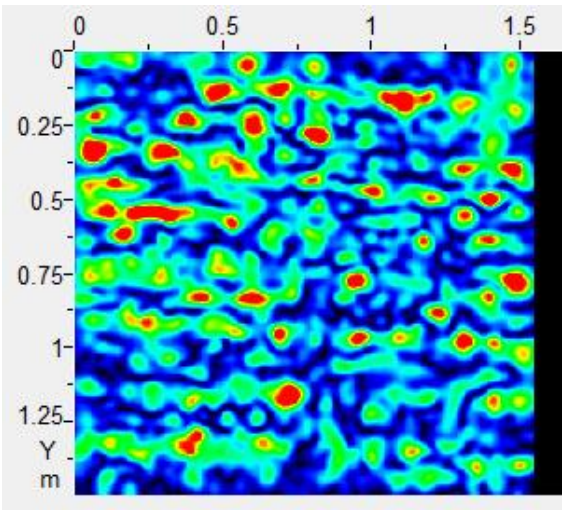

(b) Depths of 110 mm z =0.11 m

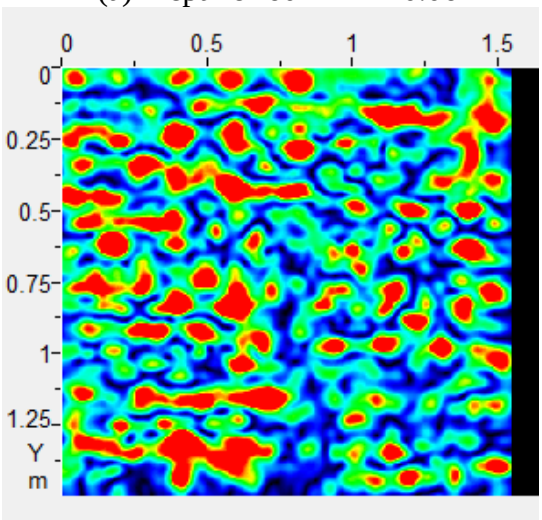

(c) Depth of 130 mm z =0.13 m

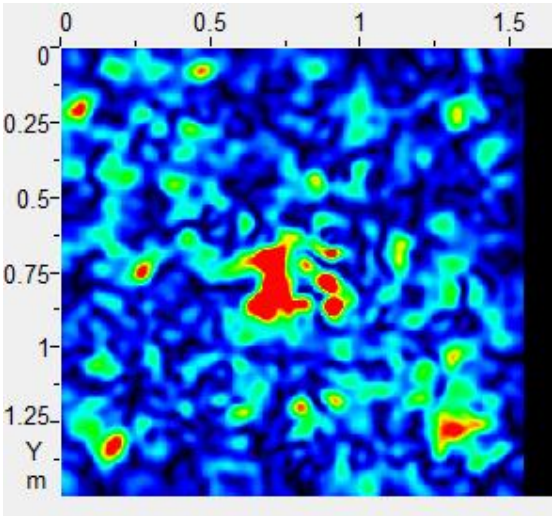

(d) Depths of 210 mm z =0.21 m

Figure A.33: C-Scans of Slab X at Various Depths from 60 mm to 210 mm

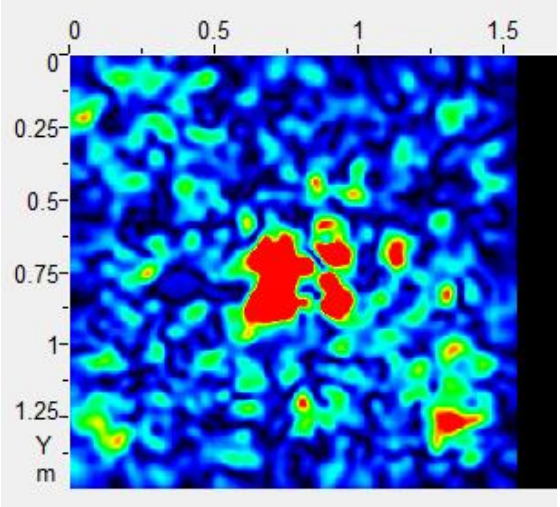

(a) Depth of 220 mm z =0.22 m

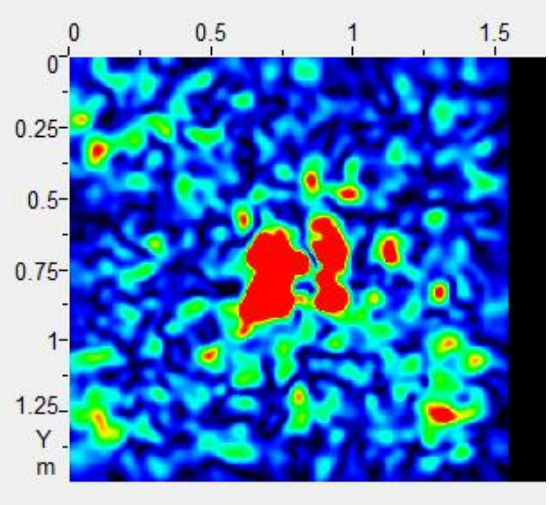

(b) Depth of 230 mm z =0.23 m

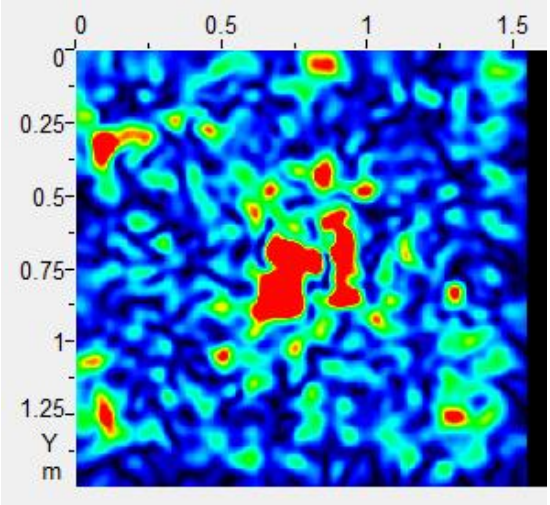

(c) Depth of 250 mm z =0.25 m

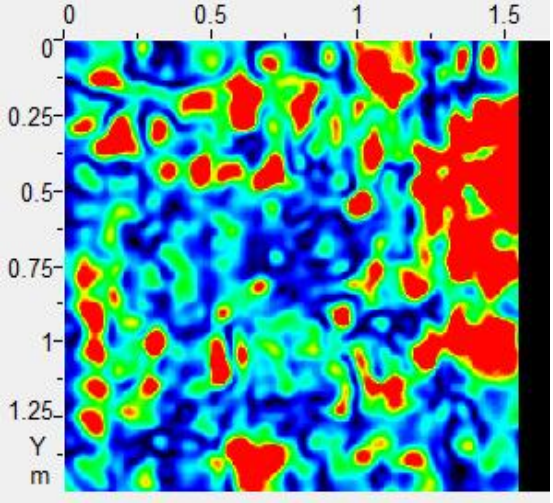

(d) Depth of 380 mm z =0.38 m

Figure A.34: C-Scans of Slab X at Various Depths from 220 mm to 380 mm

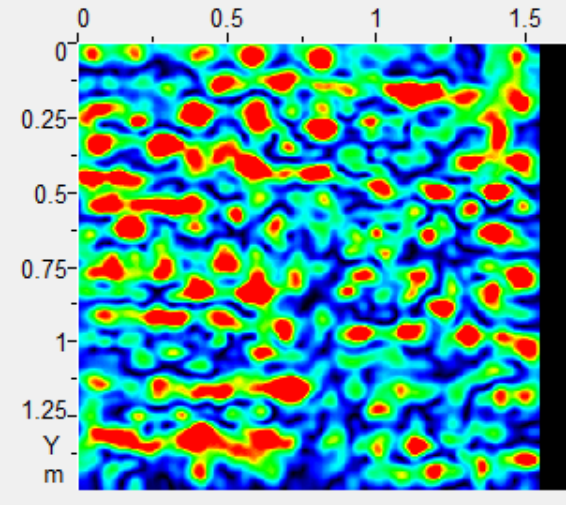

(a) Depth of 120 mm, Vertical Orientation

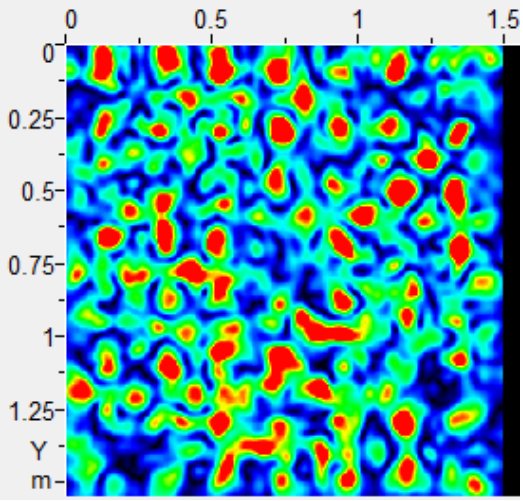

(b) Depth of 120 mm, Horizontal Orientation

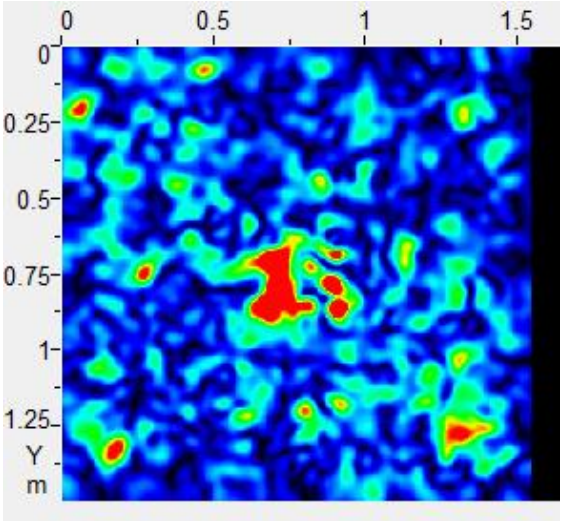

(c) Depth of 210 mm, Vertical Orientation

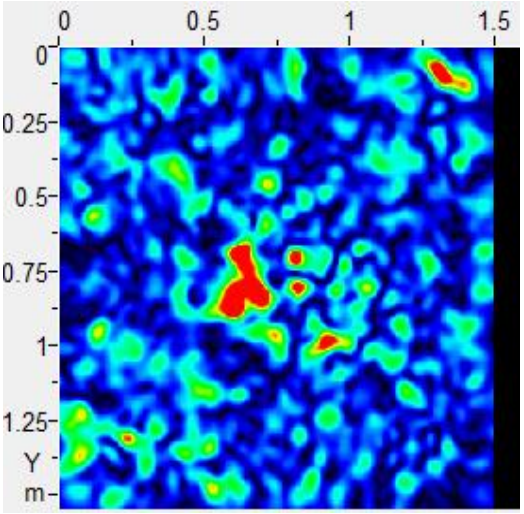

(d) Depth of 210 mm, Horizontal Orientation

Figure A.35: C-Scans of Slab X with the Vertical (left) and Horizontal (right) Orientations at 120 mm and 210 mm

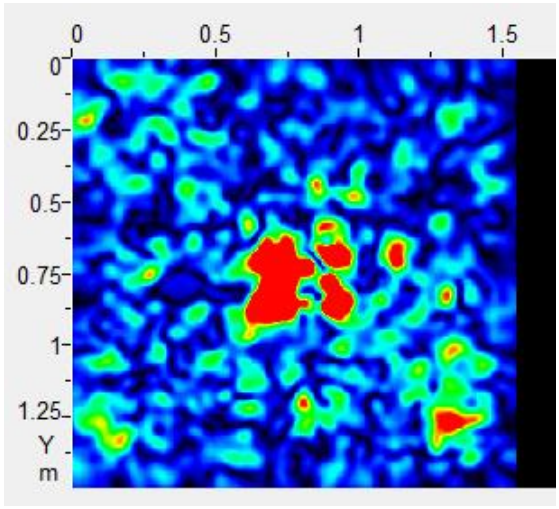

(a) Depth of 220 mm, Vertical Orientation

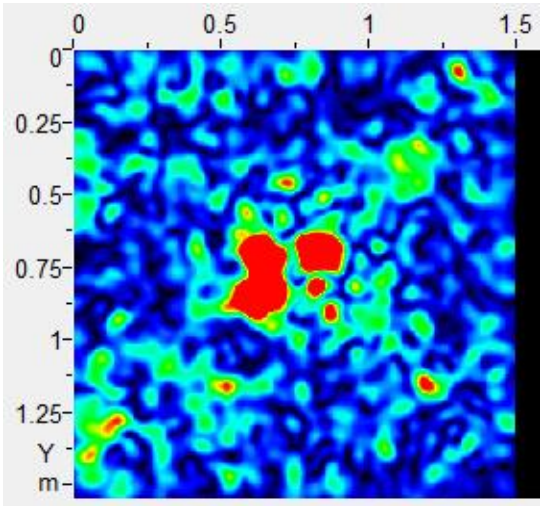

(b) Depth of 220 mm, Horizontal Orientation

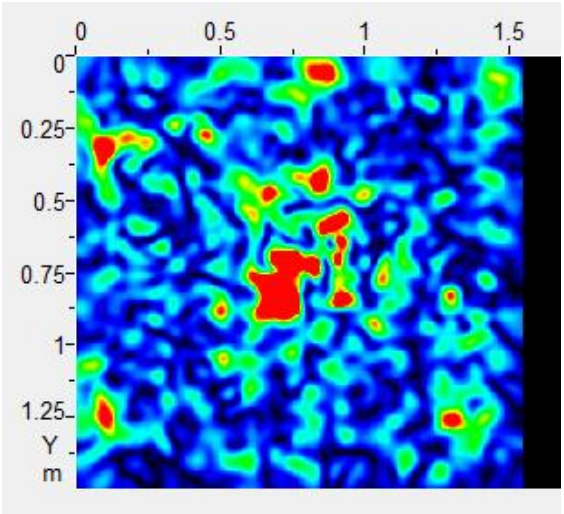

(c) Depth of 260 mm, Vertical Orientation

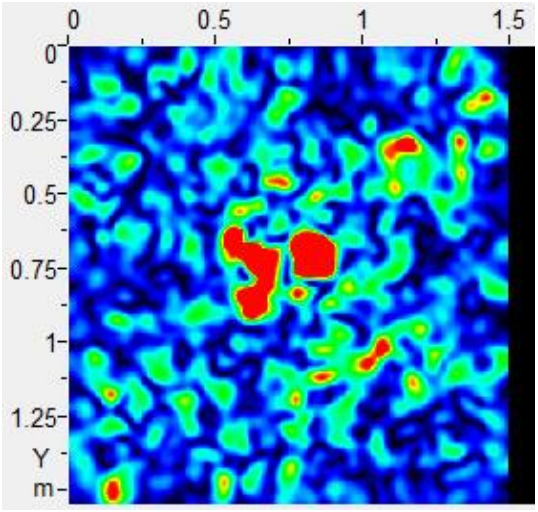

(d) Depth of 260 mm, Horizontal Orientation

Figure A.36: C-Scans of Slab X with the Vertical (left) and Horizontal (right) Orientations at 220 mm and 260 mm

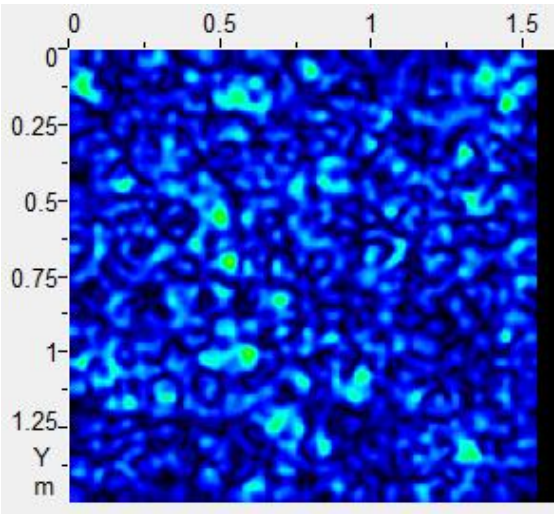

(a) Depth of 30 mm z =0.03 m

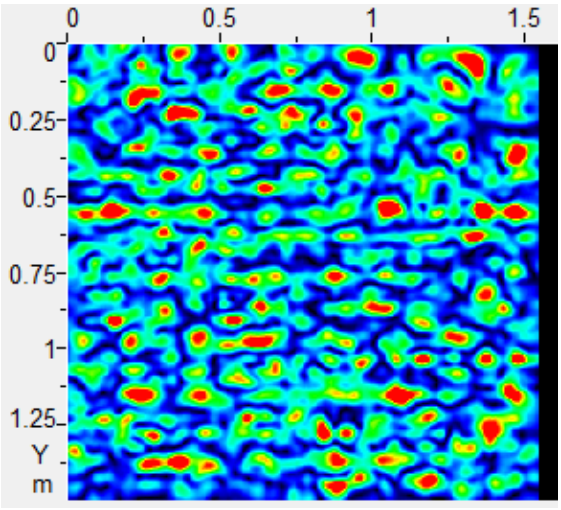

(b) Depth of 90 mm z =0.09 m

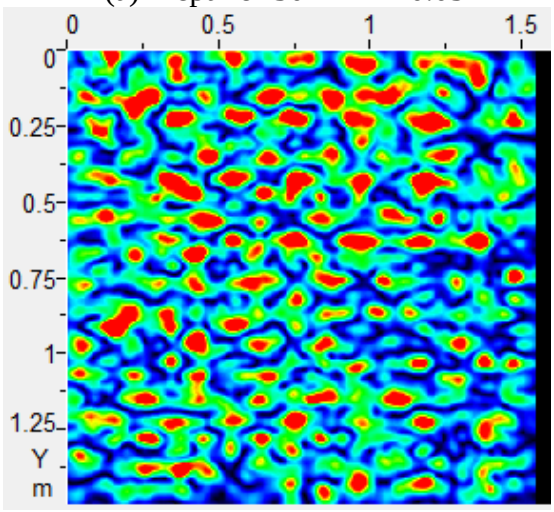

(c) Depth of 120 mm z =0.12 m

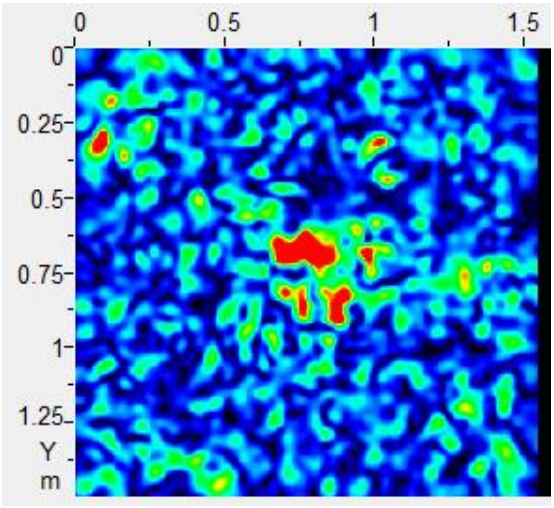

(d) Depth of 200 mm z =0.20 m

Figure A.37: C-Scans of Slab XI at Various Depths from 30 mm to 200 mm

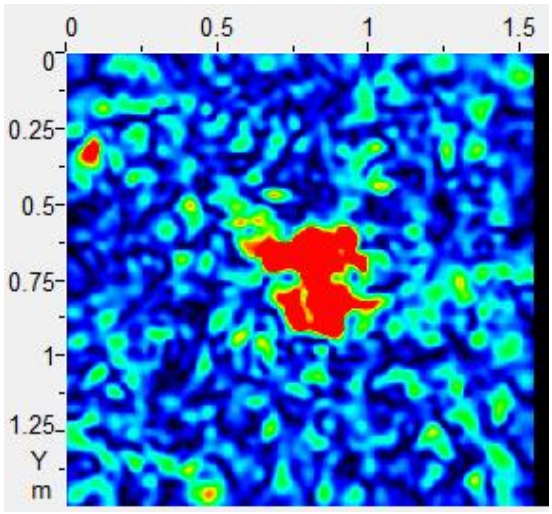

(a) Depth of 210 mm z =0.21 m

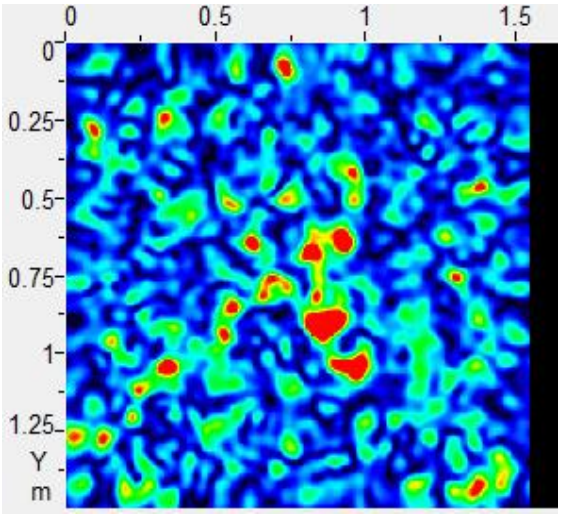

(b) Depth of 250 mm z =0.25 m

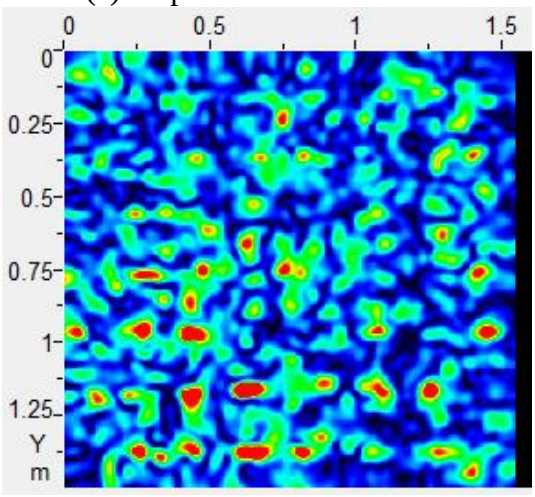

(c) Depth of 300 mm z =0.30 m

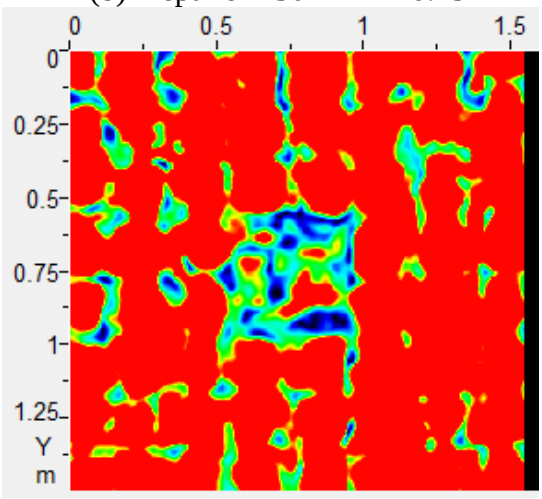

(d) Depth of 380 mm z =0.38 m

Figure A.38: C-Scans of Slab XI at Various Depths from 210 mm to 380 mm

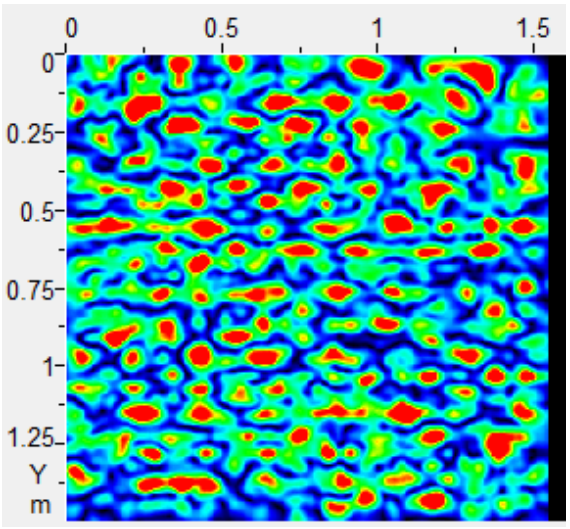

(a) Depth of 110 mm, Vertical Orientation

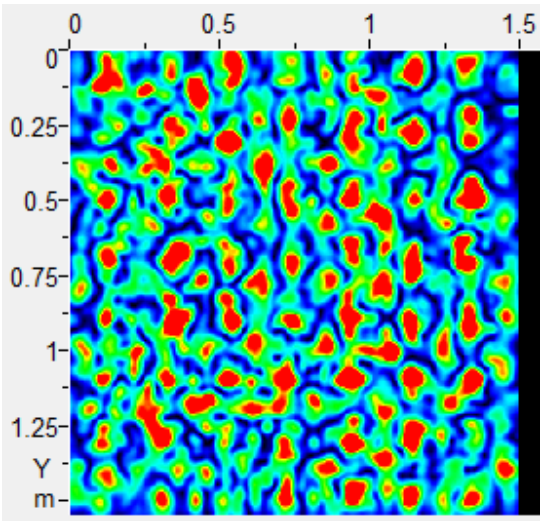

(b) Depth of 110 mm, Horizontal Orientation

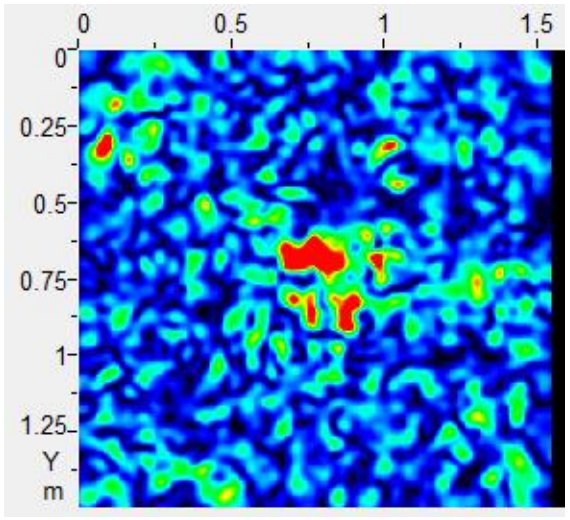

(c) Depth of 200 mm, Vertical Horizontal

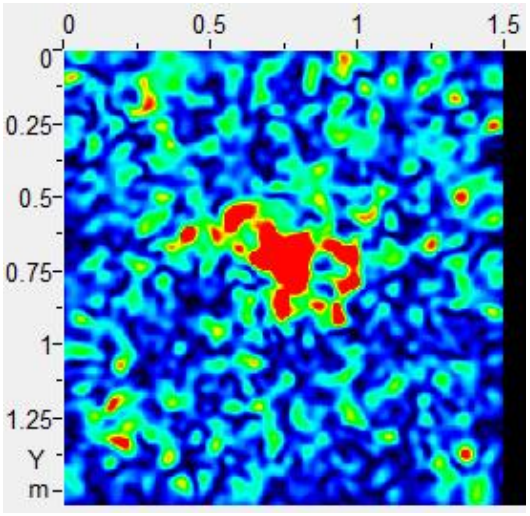

(d) Depth of 200 mm, Horizontal Orientation

Figure A.39: C-Scans of Slab XI with the Vertical (left) and Horizontal (right) Orientations at 110 mm and 200 mm

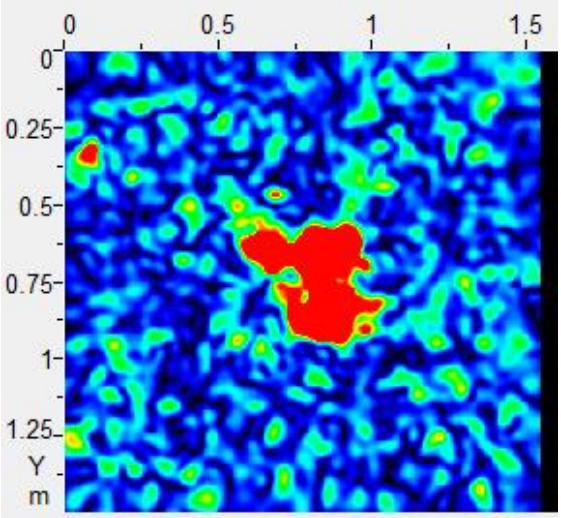

(a) Depth of 220 mm, Vertical Orientation

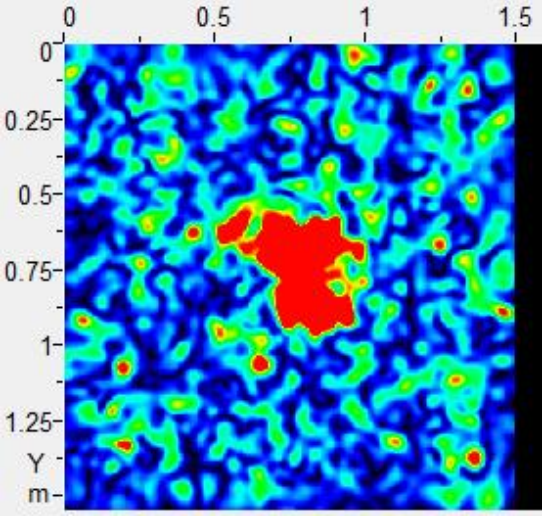

(b) Depth of 220 mm, Horizontal Orientation

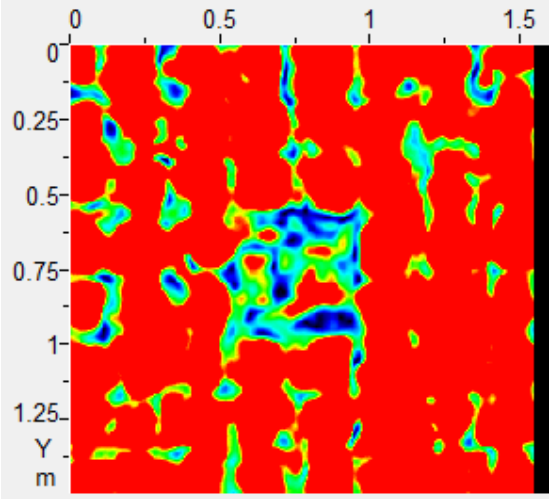

(c) Depth of 380 mm, Vertical Orientation

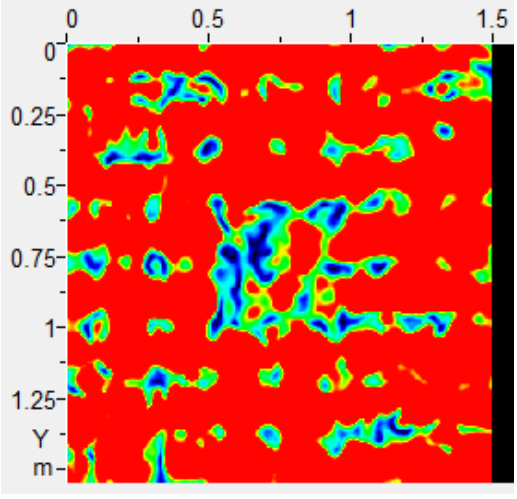

(d) Depth of 380 mm, Horizontal Orientation

Figure A.40: C-Scans of Slab XI with the Vertical (left) and Horizontal (right) Orientations at 220 mm and 380 mm